

Novel Collective Phenomena in High-Energy Proton-Proton and Proton-Nucleus Collisions

Kevin Dusling

*American Physical Society, 1 Research Road
 Ridge, NY 11961, USA
 kdusling@mailaps.org*

Wei Li

*Department of Physics and Astronomy, 6100 Main St., MS-315
 Houston, TX 77005, USA
 davidlw@rice.edu*

Björn Schenke

*Physics Department, Bldg. 510A, Brookhaven National Laboratory,
 Upton, NY 11973, USA
 bschenke@bnl.gov*

Received Day Month Year
 Revised Day Month Year

The observation of long-range rapidity correlations among particles in high-multiplicity p-p and p-Pb collisions has created new opportunities for investigating novel high-density QCD phenomena in small colliding systems. We review experimental results related to the study of collective phenomena in small systems at RHIC and the LHC along with the related developments in theory and phenomenology. Perspectives on possible future directions for research are discussed with the aim of exploring emergent QCD phenomena.

Keywords: quark-gluon plasma; relativistic heavy-ion collisions; quantum chromodynamics; color glass condensate

PACS numbers: 25.75.q, 25.75.Gz, 25.75.Ld, 12.38.t, 12.38.Aw, 12.38.Mh

Contents

1. Introduction	2
2. Collectivity and hydrodynamics in A-A collisions	4
3. Experimental evidence of collectivity in small systems	7
3.1. Two-particle correlations and azimuthal anisotropy	8
3.2. Multi-particle azimuthal correlations	10
3.3. Identified particle spectra and correlations	12
3.4. Flow factorization	17

3.5.	Femtосcopy from Hanbury-Brown-Twiss correlations	18
3.6.	Heavy flavor production	19
4.	Theoretical interpretations	20
4.1.	Final-state interactions: hydrodynamics in small systems	23
4.1.1.	Modeling of the initial state	24
4.1.2.	Viscous hydrodynamics and its limits of application	29
4.1.3.	Results from hydrodynamics in small systems	31
4.1.4.	Parton transport models	36
4.2.	Conclusions on final state interactions in small systems	38
4.3.	Multi-particle production in the Color Glass Condensate	38
4.3.1.	Two-gluon production for $\mathbf{p}_\perp \gtrsim Q_S$: Glasma Graphs	42
4.3.2.	Classical Yang-Mills dynamics	54
4.4.	Scattering from color-field domains	57
4.5.	Conclusions on initial state interactions in small systems	60
5.	Future Directions	60
5.1.	Further scrutiny of hydrodynamic paradigm	61
5.2.	Collectivity in p-p collisions	62
5.3.	Jet quenching in small systems	64
5.4.	Pre-equilibrium dynamics	66
6.	Summary	67

1. Introduction

Collective phenomena are ubiquitous across physics and observed in systems having disparate temporal and spatial scales ranging from atomic nuclei, ultra-cold atomic gases and biological systems, up to the cosmological scales involved in galaxy formation. In a broad sense, the concept of collectivity refers to a common behavior exhibited by a group of entities (e.g., particles moving with a common velocity or along a preferred direction). Collectivity is often associated with an emergent phenomenon of a complex, many-body system, for which the basic interactions (for example, at the two-body level) may be well understood. An important goal of studying collective phenomena is to unravel how the macroscopic behavior of a many-body system emerges from its fundamental degrees of freedom.

One of the most striking displays of collectivity is the strong expansion of the medium produced in ultra-relativistic heavy-ion collisions. A careful analysis of identified particle spectra, elliptic flow, Hanbury-Brown-Twiss (HBT) interferometry and the suppression of particles at high transverse momenta has indicated that a hot and dense QCD medium, the “Quark-Gluon plasma (QGP)” undergoes a nearly ideal hydrodynamic expansion when created.¹⁻⁴

Figure 1 shows one of the many persuasive pieces of evidence for collective behavior in heavy-ion collisions. The plot on the right shows the $\Delta\eta$ - $\Delta\phi$ correlation functions for pairs having $1 < p_T < 3 \text{ GeV}/c$ in semi-central Pb-Pb collisions at the LHC. The right plot shows the same observable for minimum bias p-p colli-

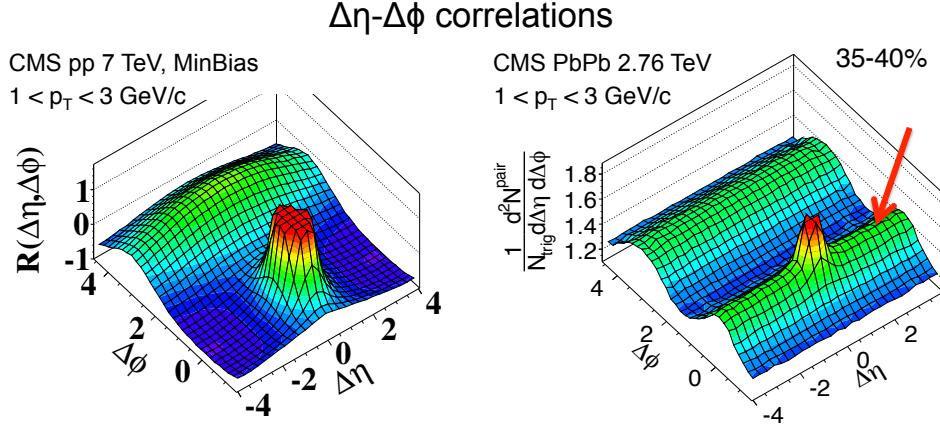


Fig. 1. Two-particle correlation function for charged hadrons with transverse momenta $1 < p_T < 3$ GeV/c in minimum bias p-p collisions at $\sqrt{s} = 7$ TeV⁵ (left) and in 35–40% centrality Pb-Pb collisions at $\sqrt{s_{NN}} = 2.76$ TeV⁶ (right), measured by the CMS experiment.

sions where a dijet-like (or mini-jet) correlation structure can be seen; the narrow peak around $(\Delta\eta, \Delta\phi) \sim (0, 0)$ comes from the showering and hadronization of the leading parton, and the long-range away-side ($\Delta\phi \sim \pi$) structure in $\Delta\eta$ represents correlations from the recoiling parton. As the two partons are produced back-to-back they necessarily have opposite rapidities and will therefore populate the full acceptance in $\Delta\eta$. In Pb-Pb collisions in addition to the jet-like correlations, a pronounced near-side ($\Delta\phi \sim 0$) collimation extending over a long range in $\Delta\eta$ is observed and is now referred to as the “ridge”. This ridge-like correlation in heavy-ion collisions such as Au-Au at RHIC and Pb-Pb at the LHC is believed to be well understood: The overlap area of a heavy-ion collision at a finite impact parameter has an elliptic shape. The larger pressure gradients along the minor-axis of the ellipse lead to a larger flow in this direction and therefore collimated production in both directions of this axis creating a near- and away-side ridge. Careful subtraction of the away-side jet peak shows that such a double-ridge is present. The absence of a ridge structure in minimum bias p-p collisions suggest the absence of collective behavior in these systems even though event-by-event fluctuations may result in highly eccentric initial states.

In 2010 surprising indications for collectivity in p-p collisions at the LHC were observed when triggering on rare events with high multiplicities (large number of final-state particles).⁵ The long-range near-side ridge for p-p events having charged multiplicity $N_{\text{trk}} > 110$ is shown in Fig. 2. This ridge-like structure, not present in minimum bias p-p collisions, is reminiscent of the two-particle correlation in A-A collisions. Determining whether the p-p ridge can be attributed to collective flow effects will require a concerted effort by theorists and experimentalists. With a variety of theoretical proposals and limited experimental data in high-multiplicity

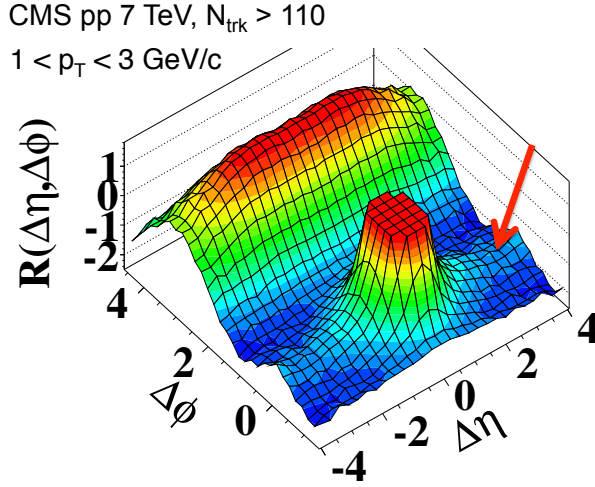


Fig. 2. Two-particle correlation function for particles having $1 < p_T < 3 \text{ GeV}/c$ in high-multiplicity p-p collisions at $\sqrt{s} = 7 \text{ TeV}$, measured by the CMS experiment.⁵

p-p collisions (see Ref.⁷ for an early review) a conclusive explanation of the p-p ridge remains outstanding.

With the discovery of the p-p ridge it was natural to look for a similar signal in p-A collisions. First collisions of high-energy proton and ion beams (p-A) were achieved at the LHC in 2011 at a center-of-mass energy of 5.02 TeV per nucleon pair. The discovery of a ridge in high-multiplicity p-Pb collisions^{8–10} did not come as a complete surprise, but the fact that the strength of the correlation was almost as large as the ridge in heavy-ion collisions was unexpected.

The ridge correlations in p-p and p-A collisions remain to be fully understood, and the existence of similar structures in small colliding systems such as d-Au¹¹ and ³He-Au collisions^{11,12} at lower RHIC energies have stimulated both experimental and theoretical communities to further investigate the properties of the ridge.

This article provides a comprehensive review of the latest experimental results and theoretical developments in our understanding of collective phenomena in dense, high-multiplicity hadronic systems. Perspectives on future directions are also discussed in light of future programs at major accelerator facilities such as RHIC and the LHC.

2. Collectivity and hydrodynamics in A-A collisions

Studies of multi-particle correlations have provided crucial insight into the underlying mechanism of particle production in relativistic heavy-ion collisions. The most prominent feature of multi-particle correlations in AA collisions is due to “elliptic flow”, an azimuthal anisotropy in momentum space induced by strong expansion

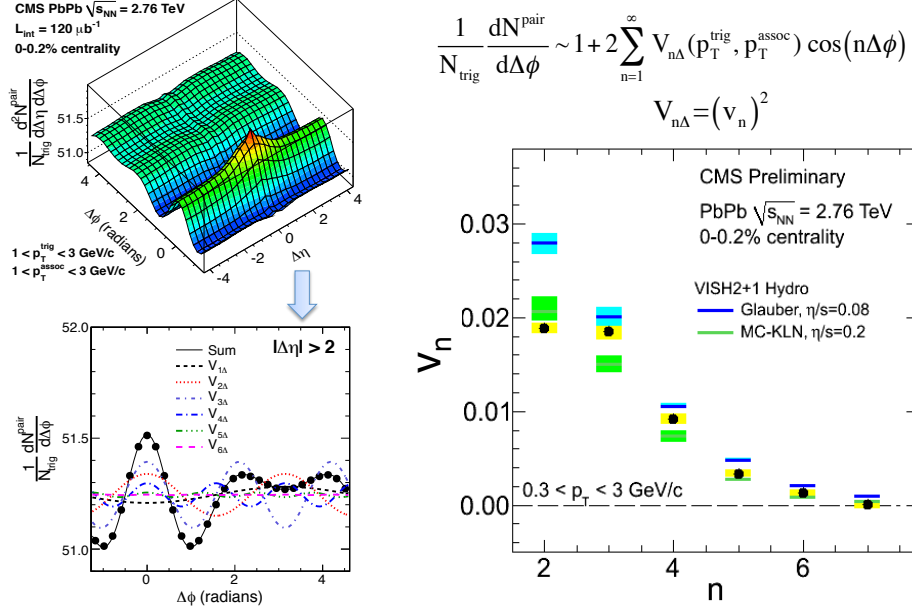


Fig. 3. Left: The 2-D and 1-D long-range $\Delta\phi$ two-particle correlation functions in ultra-central (0–0.2%) PbPb collisions at $\sqrt{s_{NN}} = 2.76$ TeV measured by the CMS collaboration. Right: the extracted v_n Fourier harmonics from long-range two-particle correlations integrated over $0.3 < p_T < 3$ GeV/c, compared with hydrodynamic calculations.²⁵

of the initial almond-shaped overlap area of two nuclei.¹³ Elliptic flow phenomena can be well described by relativistic hydrodynamic simulations with a viscosity approaching the KSS bound $\eta/s = 1/4\pi \approx 0.08$.¹⁴ In two-particle correlation measurements the elliptic flow generates an approximate $\cos(2\Delta\phi)$ component to the two-particle correlation function that extends over a broad $|\Delta\eta|$ range.¹⁵ The long-range in rapidity is a consequence of the approximate boost invariance of the system. Studies of elliptic flow have been carried out over a wide range of energies and systems^{16–24} at both RHIC and the LHC.

Event-by-event fluctuations in the collision geometry of the initial-state introduce higher-order anisotropic flow components. For example, “triangular flow” results in a $\cos(3\Delta\phi)$ modulation of the two-particle correlation.^{26–31} This contribution can dominate the structure of the entire $\Delta\phi$ correlation in very central A-A collisions, as is shown in figure 3 for the top 0–0.2% central Pb-Pb collisions at LHC. A prominent *double hump* appears on the away-side.

By projecting the long-range component ($|\Delta\eta| > 2$) of the 2-D correlation function onto a 1-D $\Delta\phi$ axis the correlations can be characterized by a Fourier series, $\sim 1 + 2 \sum_n v_n^2 \cos(n\Delta\phi)$, where v_n denotes the single-particle anisotropy harmonic of order n .³² A dominant third-order Fourier component is seen because in ultra-central A-A collisions the impact parameter is small enough such that the initial

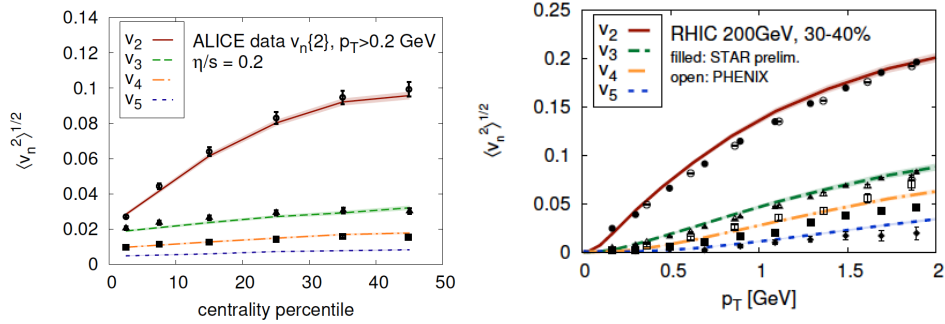


Fig. 4. Model calculations compared to measurements of the harmonic decomposition of azimuthal correlations produced in heavy ion collisions.³³ The left panel shows model calculations and data for v_n vs. collision centrality in Pb+Pb collisions at $\sqrt{s_{NN}} = 2.76$ TeV. The right panel shows similar studies for the p_T dependence of v_n in 200 GeV Au+Au collisions. The comparison of the two energies provides insight on the temperature dependence of η/s .

(average) ellipticity is negligible. On an event-by-event basis, the initial geometry is governed by fluctuations resulting in comparable elliptic and triangular asymmetries.

Of course, any set of data can be decomposed into a Fourier series and the existence of a large elliptic anisotropy cannot be taken as proof of hydrodynamic behavior in and of itself. Quantitative comparison with theoretical calculations, in this case viscous relativistic hydrodynamic simulations is necessary in order to draw any strong conclusions. On the right-hand side of Fig. 3, the extracted v_2 – v_6 data in ultra-central Pb-Pb collisions from CMS are compared to viscous hydrodynamic calculations using two different initial conditions (the details of which will be discussed later). These results indicate that the produced medium has a shear viscosity to entropy density ratio of $\eta/s \sim 0.08 - 0.2$.

Higher-order flow components in A-A collisions can provide more stringent constraints on extracting both transport properties (e.g., η/s) and initial-state models of heavy-ion collisions. Indeed, the elliptic and higher-order flow phenomena have been extensively studied at RHIC and the LHC over a wide range of collision centrality and particle p_T . Fig. 4 shows the comparison of p_T -integrated v_n as a function of centrality in Pb-Pb collisions at the LHC (left) and v_n as a function of p_T for 30–40% central Au-Au collisions at RHIC with hydrodynamic calculations using the IP-Glasma initial-state model.^{33,34} The LHC data is well described by an $\eta/s = 0.2$ and at RHIC by $\eta/s = 0.12$ providing indication of a temperature dependence. It has now been widely accepted that in relativistic heavy-ion collisions, a strongly-coupled medium is formed exhibiting near-ideal fluid behavior.

3. Experimental evidence of collectivity in small systems

This section provides a broad overview of experimental results in small colliding systems, focusing on the recent results from p-Pb collisions at the LHC. While many of the experimental observables explored in this section will have striking similarities with the results from A-A collisions, one must be cautioned that strong conclusions about the interpretation of these measurements in A-A could only be made after detailed models (in this case hydrodynamics) confronted the data. Clearly, the system size in p-p or p-A collisions is significantly smaller, and therefore the applicability of hydrodynamics must be scrutinized. This section collects the wealth of experimental data we have on small systems and compares it to that in A-A with interpretations postponed to section 4.

An important point that should be kept in mind throughout this discussion is that the nature of the very events we are studying in small systems are in a class of their own. They represent a fraction of the total cross-section, as can be gleaned from figure 5 that shows the multiplicity distributions for minimum bias p-p, p-Pb and peripheral 50–100% central Pb-Pb collisions from CMS.^{5,35} Here, multiplicity is defined as the number of charged tracks within $|\eta| < 2.4$ and $p_T > 0.4 \text{ GeV}/c$. Events with 100–200 tracks (these are the high-multiplicity events where a ridge signal is seen in p-p and p-Pb) are a common occurrence in Pb-Pb. In general, experimental signatures should not depend only on the multiplicity; p-p and Pb-Pb events producing 100 tracks have a very different nature.

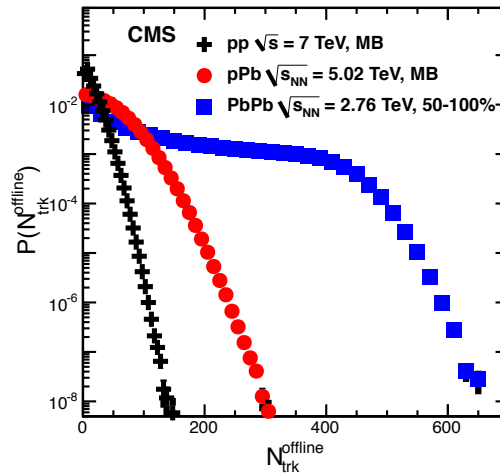


Fig. 5. Multiplicity (N_{trk}) distributions for MinBias p-p, MinBias p-Pb and 50–100% centrality Pb-Pb collisions.^{5,35}

3.1. Two-particle correlations and azimuthal anisotropy

In September 2012, first collisions of proton and lead have been delivered by the LHC at $\sqrt{s_{NN}} = 5.02$ TeV. About two million minimum bias p-Pb events were collected in a few hours of beam time by each experiment. Experiments with p-A were to serve as a control experiment for A-A collisions providing baselines for cold nuclear matter effects.³⁶

However, with the recent discovery of the ridge in p-p, it was not clear what would be observed in high multiplicity p-A collisions. The p-A pilot run discovered a significant near-side ridge, as shown in Fig. 6, within the top few % (CMS,¹⁰ ATLAS⁹) or even 20% (ALICE⁸) multiplicity class. A 2013 high-intensity p-Pb run provided access to higher multiplicity classes and increased statistics.

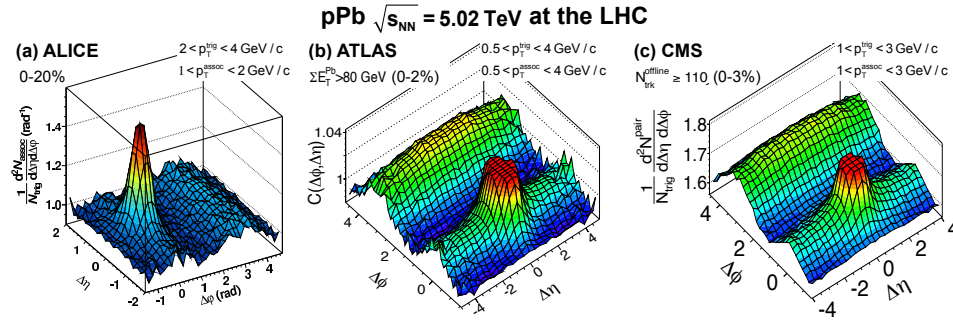


Fig. 6. The 2D two-particle correlation functions in high-multiplicity p-Pb collisions at $\sqrt{s_{NN}} = 5.02$ TeV measured by the ALICE (0–20%, left),⁸ ATLAS (0–2%, middle)⁹ and CMS (0–3%, right)¹⁰ experiments.

The magnitude of the (near side) ridge in p-Pb collisions stands out as a prominent feature being about four times larger than the p-p ridge for $N_{\text{trk}}^{\text{offline}} > 110$ and becomes comparable to the away-side jet peak. In order to disentangle the ridge from the jet the ALICE and ATLAS collaborations subtracted the contribution of jets to the away-side correlation structure in high-multiplicity events, based on the estimates from low-multiplicity events. Implicit in this procedure is the assumption that there is negligible modification of the jet due to the high multiplicities (while this is clearly not valid in A-A collisions there has yet to be an observation of jet quenching in p-p or p-A). Following this subtraction procedure a “double” ridge structure having near- and away-side correlations of similar strength has been observed, as shown in Fig. 7 for the 2D correlation function and its projection to 1D in azimuthal angle.

Motivated by the last decade of study of flow harmonics in A-A collisions the “double” ridge structure in p-Pb collisions has been analyzed using the same Fourier decomposition. The second- and third-order anisotropy Fourier harmonics, v_2 and v_3 , are extracted from the long-range correlations as a function of p_T in high-

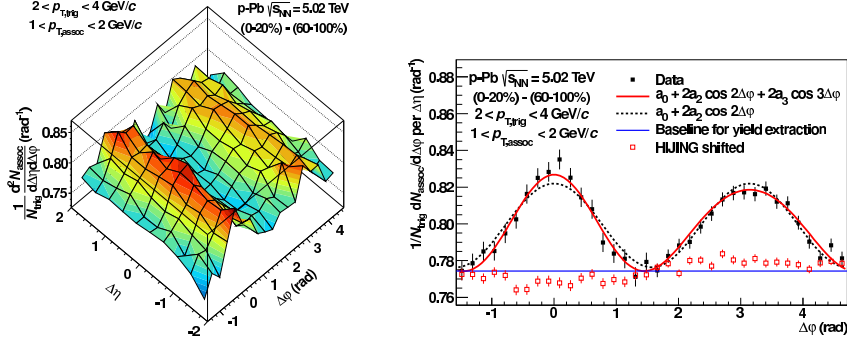


Fig. 7. The difference of two-particle correlation functions between high- and low-multiplicity p-Pb collisions at $\sqrt{s_{NN}} = 5.02$ TeV measured by the ALICE experiment.⁸

multiplicity p-Pb collisions at $\sqrt{s_{NN}} = 5.02$ TeV, shown in Fig. 8 (bottom) from three LHC experiments.^{8, 35, 37} The curves shown from the CMS experiment are the results for v_2 and v_3 without subtracting the away-side jet demonstrating that in high-multiplicity events the contribution from jets to the Fourier harmonics are negligible at low enough p_T .

Results of v_2 and v_3 in Pb-Pb collisions at $\sqrt{s_{NN}} = 2.76$ TeV are also shown in Fig. 8 (top), for a similar multiplicity range as for p-Pb collisions. ALICE, ATLAS and CMS results are in good agreement. Very recently, a sizeable v_2 has also been extracted from p-p collisions at 13 TeV by the ATLAS collaboration.³⁸

As shown in Fig. 8, the v_2 and v_3 values first rise with p_T up to around 3 GeV and then fall off toward much higher p_T , a behavior that is very similar to Pb-Pb collisions. This may be an indication of a common origin of the ridge phenomenon in all collision systems. In Pb-Pb collisions, the trend at low p_T is consistent with hydrodynamic predictions, while the decrease of higher p_T v_n could be due to the lack of thermalization of more energetic probes. Surprisingly, the v_3 harmonics as a function of p_T for p-Pb and Pb-Pb systems are almost identical. This striking similarity extends to the full multiplicity range, as one can see from Fig. 9 (right) for v_3 averaged over $0.3 < p_T < 3$ GeV/c in p-Pb and Pb-Pb. Considering the drastically different initial-state geometry and system size of the two systems, this similarity and its implication remain to be fully understood. Arguments based on the universality of fluctuation-driven initial-state anisotropies^{40–43} followed by the linear response of hydrodynamics may explain the coincidental triangular flows seen in p+Pb and Pb-Pb collisions. The v_2 value at a given multiplicity (Fig. 9, left) is larger in Pb-Pb than in p-Pb; this is expected since we know in Pb-Pb there is a large initial eccentricity that after expansion generates a large v_2 .

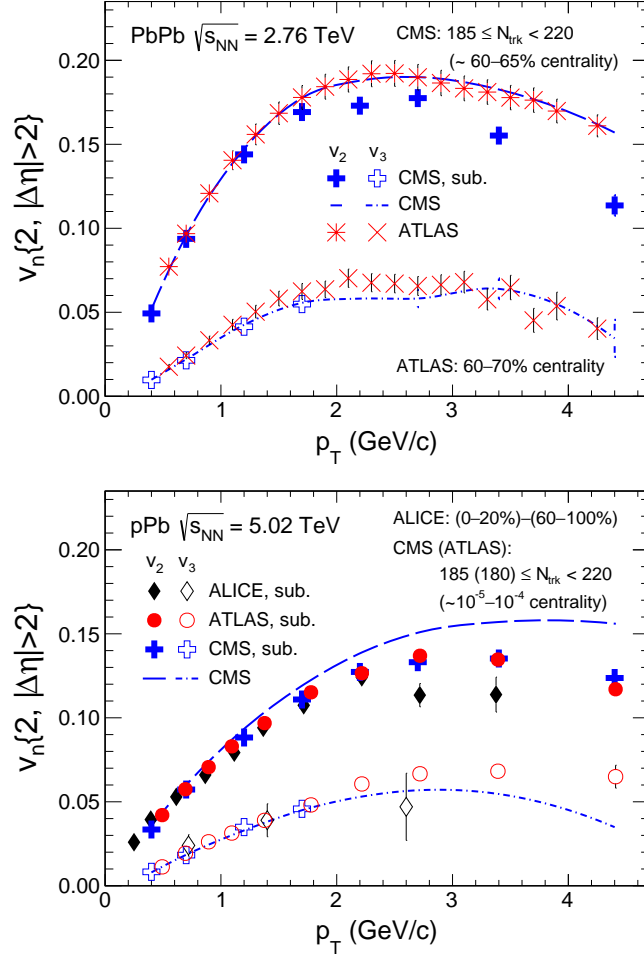


Fig. 8. The second-order (v_2) and third-order (v_3) Fourier harmonics, extracted from long-range two-particle correlations, as a function of p_T in Pb-Pb collisions at $\sqrt{s_{NN}} = 2.76$ TeV (top) and high-multiplicity p-Pb collisions at $\sqrt{s_{NN}} = 5.02$ TeV (bottom). The curves represent original v_n data, while the markers denote the results after correcting for back-to-back jet correlations estimated from low-multiplicity events. Data are obtained from Refs.^{8, 35, 37, 39}

3.2. Multi-particle azimuthal correlations

One of the key questions about the nature of the ridge and its collectivity is whether it is only a two-particle correlation or if a correlation persists amongst all produced particles. The multi-particle cumulant technique was developed to measure the strength of collective azimuthal anisotropy by correlating four or more particles simultaneously.^{44–46} It is designed to extract cumulants of collective azimuthal correlations, while suppressing non-collective short-range correlations, involving only

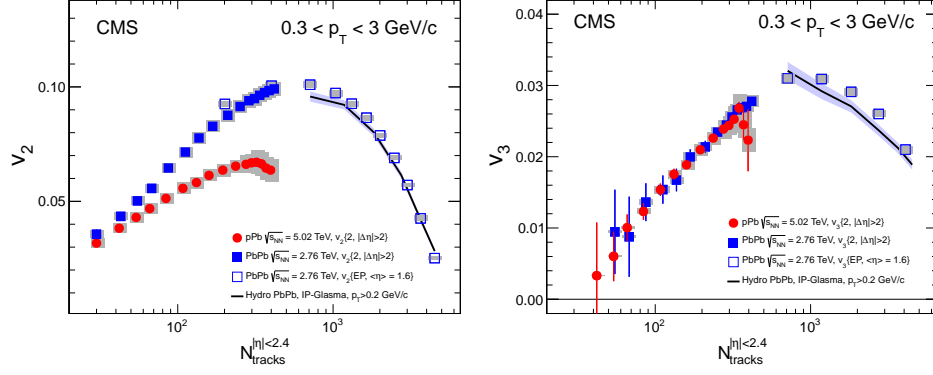


Fig. 9. The p_T -averaged v_2 (left) and v_3 (right) for $0.3 < p_T < 3$ GeV/c as a function of multiplicity in pPb (from two-particle correlation method) and PbPb (from event-plane method) collisions, measured by the CMS collaboration.³⁵ The solid line shows a hydrodynamic calculation using IP-Glasma initial conditions for Pb-Pb collisions.²⁸

a few particles. This approach has been widely used in studying A-A collisions.
22, 23, 47–51

Measurements of the four-particle cumulant have been performed by the ATLAS,⁵² CMS³⁵ and ALICE⁵³ collaborations. It was later extended to six-, eight- and *all*-particle (so-called “Lee-Yang Zeroes” (LYZ)) cumulants.⁵⁴ Fig. 10 shows the measured multi-particle cumulants, c_4 , c_6 , and c_8 , as a function of multiplicity in p-Pb and Pb-Pb collisions. These cumulants, $c_n\{n\}$, are calculated as follows:

$$\begin{aligned}
 c_n\{2\} &= \langle\langle 2 \rangle\rangle, \\
 c_n\{4\} &= \langle\langle 4 \rangle\rangle - 2 \cdot \langle\langle 2 \rangle\rangle^2, \\
 c_n\{6\} &= \langle\langle 6 \rangle\rangle - 9 \cdot \langle\langle 4 \rangle\rangle \langle\langle 2 \rangle\rangle + 12 \cdot \langle\langle 2 \rangle\rangle^3, \\
 c_n\{8\} &= \langle\langle 8 \rangle\rangle - 16 \cdot \langle\langle 6 \rangle\rangle \langle\langle 2 \rangle\rangle - 18 \cdot \langle\langle 4 \rangle\rangle^2 + 144 \cdot \langle\langle 4 \rangle\rangle \langle\langle 2 \rangle\rangle^2 - 144 \langle\langle 2 \rangle\rangle^4,
 \end{aligned} \tag{1}$$

where two- and multi-particle azimuthal correlations are evaluated as:

$$\begin{aligned}
 \langle\langle 2 \rangle\rangle &\equiv \langle\langle e^{in(\phi_1 - \phi_2)} \rangle\rangle, \\
 \langle\langle 4 \rangle\rangle &\equiv \langle\langle e^{in(\phi_1 + \phi_2 - \phi_3 - \phi_4)} \rangle\rangle, \\
 \langle\langle 6 \rangle\rangle &\equiv \langle\langle e^{in(\phi_1 + \phi_2 + \phi_3 - \phi_4 - \phi_5 - \phi_6)} \rangle\rangle, \\
 \langle\langle 8 \rangle\rangle &\equiv \langle\langle e^{in(\phi_1 + \phi_2 + \phi_3 + \phi_4 - \phi_5 - \phi_6 - \phi_7 - \phi_8)} \rangle\rangle.
 \end{aligned} \tag{2}$$

Here $\langle\langle \dots \rangle\rangle$ represents the average over all combinations of particles from all events. The elliptic flow harmonics are related to the multi-particle cumulants by

$$v_n\{4\} = \sqrt[4]{c_n\{4\}}, \quad v_n\{6\} = \sqrt[6]{\frac{1}{4}c_n\{6\}}, \quad v_n\{8\} = \sqrt[8]{-\frac{1}{33}c_n\{8\}}, \tag{3}$$

which are shown in Fig. 11, for p-Pb and Pb-Pb systems side-by-side as a function of multiplicity.

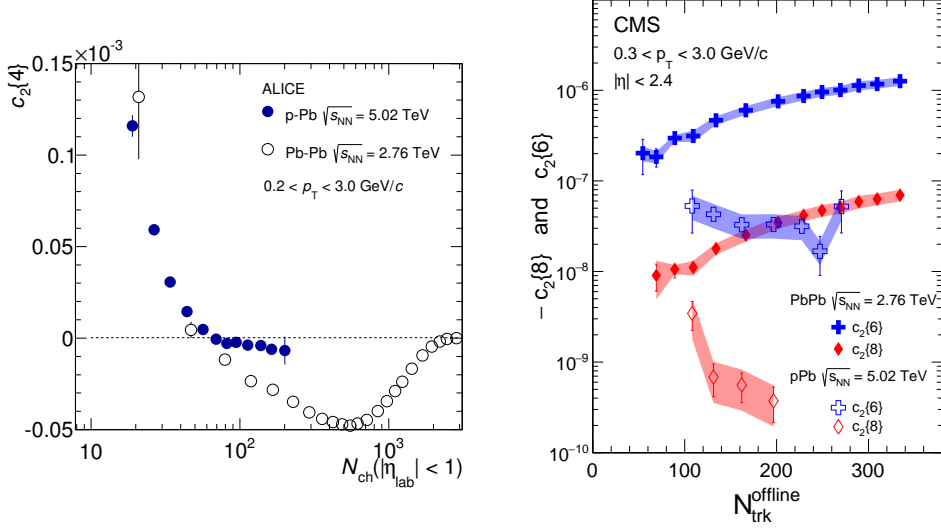


Fig. 10. The four- (c_4) , six- (c_6) and eight- (c_8) particle cumulants as a function of N_{trk} , averaged over $(0.2)0.3 < p_T < 3.0$ GeV/c, in Pb-Pb collisions at $\sqrt{s_{\text{NN}}} = 2.76$ TeV and p-Pb at $\sqrt{s_{\text{NN}}} = 5.02$ TeV. Data are obtained from Refs.^{53,54}

Within experimental uncertainties, v_2 values from various higher-order cumulant methods are all consistent with each other in both p-Pb and Pb-Pb as a function of multiplicity lending support to the highly collective nature of these systems. The v_2 from two-particle correlations does not follow the trends of the v_2 from higher cumulants. Part of the deviation may be due to the away-side jet which persists out to rapidity separations larger than the two unit rapidity gap imposed in the measurement. However, one would expect the effect from mini-jets to be smaller at higher multiplicities. The breaking of $v_2\{2\} \neq v_2\{4\}$ is present in hydrodynamic models when event-by-event dynamical fluctuations of v_2 contribute differently to two-particle and higher-order cumulants.

It should be stressed that although the observed scaling in Fig. 11 is a necessary outcome of a hydrodynamic framework it is not sufficient proof that hydrodynamics is the correct underlying theory. The measurements are a milestone as they lend credence to the highly collective nature of p-Pb collisions and show that the ridge is a highly non-trivial emergent phenomena.

3.3. Identified particle spectra and correlations

Single-particle p_T spectra for various particle species as well as their multiplicity dependence in each collision system provide rich information for constraining the dynamics of particle production. Multiplicity dependence of identified particle (PID) p_T spectra have been measured in p-p, p-Pb and Pb-Pb collisions at the LHC.^{55–58} In Fig. 12 (top), the average p_T ($\langle p_T \rangle$) for π^+/π^- , K^+/K^- , p/\bar{p} , K_S^0 and

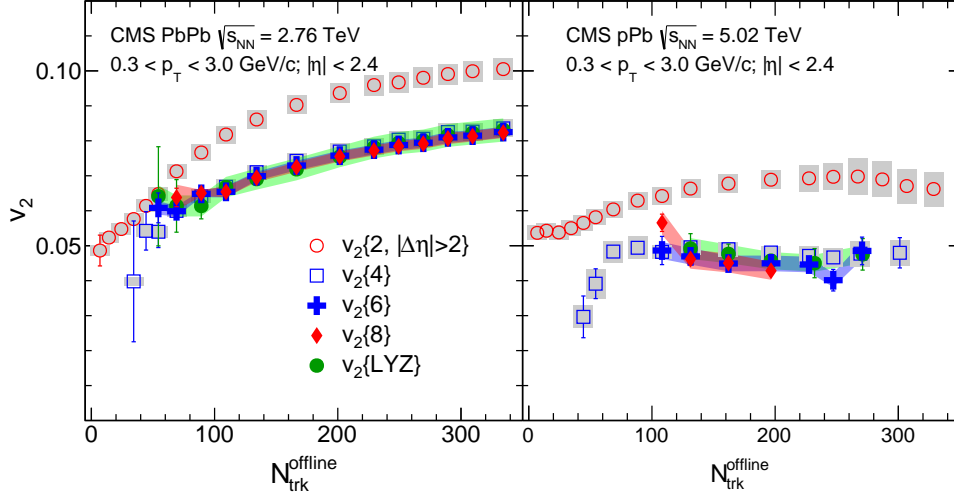


Fig. 11. The second-order Fourier harmonic, v_2 , as a function of N_{trk} obtained from two-, four-, six- and eight-particle cumulants, and the LYZ method, averaged over $0.3 < p_T < 3.0$ GeV/c, in Pb-Pb at $\sqrt{s_{NN}} = 2.76$ TeV (left) and p-Pb at $\sqrt{s_{NN}} = 5.02$ TeV (right).⁵⁴

$\Lambda/\bar{\Lambda}$ particles as measured by the ALICE collaboration is shown as a function of event multiplicity in p-Pb collisions at $\sqrt{s_{NN}} = 5.02$ TeV.⁵⁵

As multiplicity increases, p_T spectra of all particle species become flatter (or “harder”). A similar trend is also found in MC models such as PYTHIA and HIJING, HIJING, which may be due to the biasing towards higher Q^2 processes when triggering on high-multiplicity events. However, the most distinct feature of the data is not just the fact that $\langle p_T \rangle$ increases with multiplicity, but the increase is observed to be faster for particles with a heavier mass. For example, the ratio of proton to pion p_T spectra is enhanced in the higher p_T region, going from low- to high-multiplicity events. Moreover, the CMS collaboration reported that the amount of increase in $\langle p_T \rangle$ for each particle species from low to high multiplicity events is approximately proportional to the particle’s mass.⁵⁷

Similar mass dependence of PID spectra in A-A collisions has been extensively studied. In hydrodynamic models, it is attributed to the effect of a common velocity field along the radial direction of the medium, which generates a boost in particle momentum that is roughly proportional to the mass of the particle. A common framework for describing this characteristic mass dependence of p_T spectra is the “blast-wave” model,⁶¹ with parameters of a common kinetic freeze-out temperature, T_{kin} , and an average radial expansion velocity, $\langle \beta_T \rangle$ (β_T also depends on the radius).

Fitting to the experimental spectra, $\langle \beta_T \rangle$ and T_{kin} can be extracted, and are shown in Fig. 12 (bottom) for p-Pb and Pb-Pb collisions for different multiplicity or centrality ranges. In Pb-Pb, more central collisions tend to have a larger $\langle \beta_T \rangle$ (due to larger pressure gradients) and a smaller T_{kin} (because of a larger system size

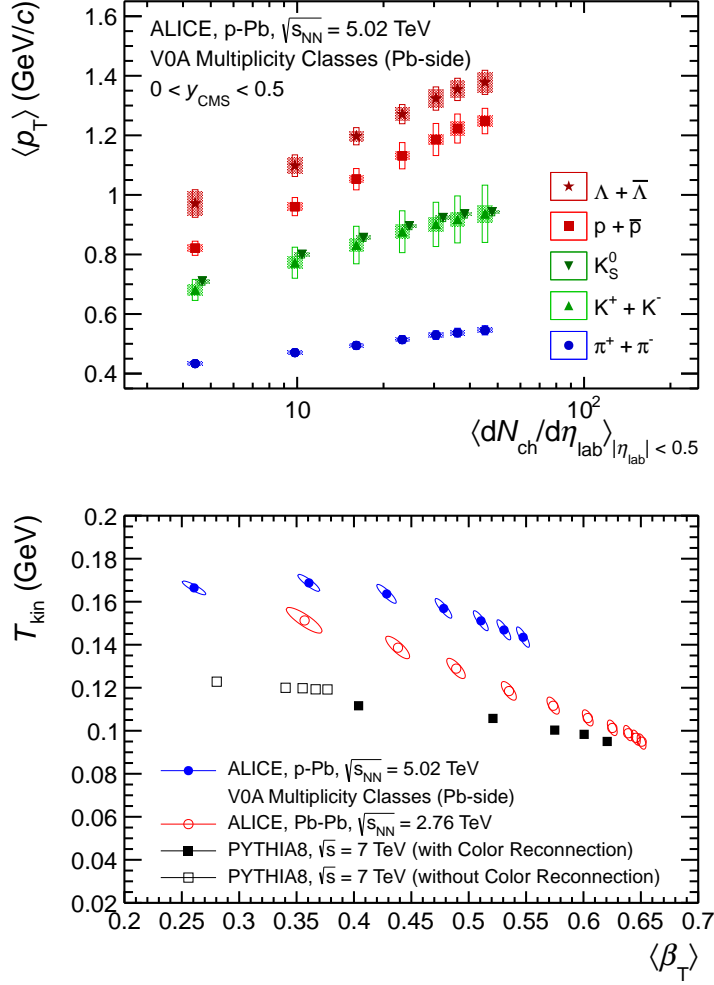


Fig. 12. Top: Average transverse momentum of π^+/π^- , K^+/K^- , p/\bar{p} , K_S^0 and $\Lambda/\bar{\Lambda}$ particles as a function of multiplicity in pPb collisions at $\sqrt{s_{NN}} = 5.02$ TeV. Bottom: parameters of blast-wave fits to identified particle spectra for pPb and PbPb collisions, and PYTHIA8 models.⁵⁵

resulting in a longer lifetime of the hadronic rescattering stage). A similar trend is also observed in p-Pb collisions. Interestingly, if comparing p-Pb and Pb-Pb systems at similar multiplicities (about the same T_{kin}), the radial flow velocity is larger in the smaller p-Pb system. If fixing the total energy or entropy, a smaller QGP fluid possesses a stronger radial pressure gradient,^{62–64} which is consistent with the data. To verify this picture, one important step will be to carry out the same studies in high-multiplicity p-p collisions, which have an even smaller system size.

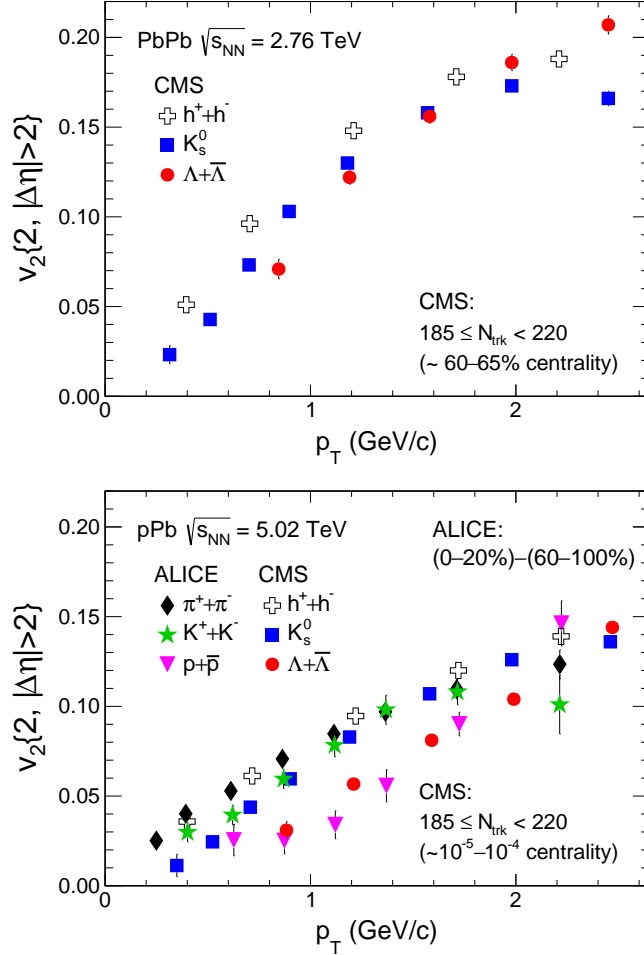


Fig. 13. The second-order Fourier harmonic, v_2 , for charged hadrons, π^+/π^- , K^+/K^- , and p/\bar{p} from ALICE,⁵⁹ K_s^0 and $\Lambda/\bar{\Lambda}$ from CMS,⁶⁰ as a function of p_T for $185 \leq N_{trk} < 220$ in Pb-Pb collisions at $\sqrt{s_{NN}} = 2.76$ TeV and p-Pb collisions at $\sqrt{s_{NN}} = 5.02$ TeV.

While the hydrodynamic fluid picture provides a natural interpretation to the data, as shown in Fig. 12 (bottom), the PYTHIA model with color reconnections^{65,66} can also generate similar behavior as seen in the data. In PYTHIA an outgoing hard parton and the underlying event are connected through color strings. As a result, strings will be pulled out of the underlying event in the transverse direction by the fast-moving parton, and then fragment into final-state particles. The color reconnection method increases this effect by reconnecting partons close in phase space. In this way, the “radially boosted” string provides an effective common velocity for the hadrons produced from it, just like a fluid cell in the hydrody-

dynamic picture. Meanwhile, models based on gluon saturation can also qualitatively describe the general trend of the data.⁶⁷

To further differentiate theoretical models in p-Pb collisions, studies of identified particles have been extended to two-particle correlations. A long-range near-side two-particle correlation involving an identified particle is also observed.^{59,60} Results for the single-particle v_2 harmonic for π^+/π^- , K^+/K^- , p/\bar{p} , K_S^0 and $\Lambda/\bar{\Lambda}$ particles as a function of p_T in Pb-Pb and p-Pb collisions at similar multiplicities are shown in Fig. 13. For both systems, a particle species dependence of v_2 is observed. At a given p_T , particles having a larger mass tend to exhibit a smaller v_2 anisotropy. This mass ordering effect of v_2 was first seen in A-A collisions at RHIC and LHC energies,^{2,4,68-70} which can again be understood as the effect of radial flow pushing heavier particles toward higher- p_T .⁷¹⁻⁷³ Comparing p-Pb and Pb-Pb systems at similar multiplicities in Fig. 13, a large mass splitting can be seen in the smaller p-Pb system, which is again consistent with the hydrodynamic picture.^{74,75} It remains to be seen whether other theoretical interpretations, such as string fragmentation with color reconnections, can describe the features found in both single-particle and two-particle correlation data, as well as their system size dependence.

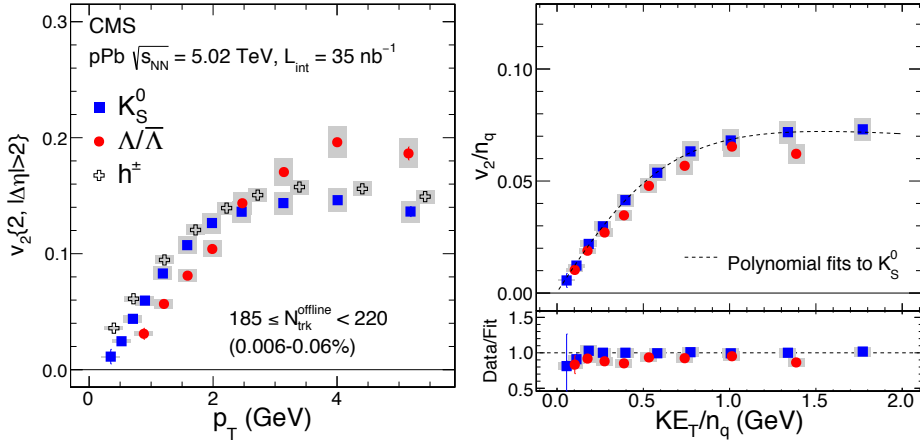


Fig. 14. Top: The second-order Fourier harmonic, v_2 , for K_S^0 , $\Lambda/\bar{\Lambda}$, and unidentified charged particles as a function of p_T for $185 \leq N_{\text{trk}} < 220$ obtained in p-Pb collisions at $\sqrt{s_{\text{NN}}} = 5.02$ TeV. Bottom: the n_q -scaled v_2 values of K_S^0 and $\Lambda/\bar{\Lambda}$ as a function of $(KE_T)/n_q$. Ratios of v_2/n_q to a smooth fit function of v_2/n_q for K_S^0 as a function of $(KE_T)/n_q$ are also shown.⁶⁰

In heavy ion collisions, a scaling phenomenon of v_2 with the number of constituent quarks (n_q) has been discovered.⁷⁶⁻⁷⁸ The values of v_2/n_q are found to be very similar for all mesons ($n_q = 2$) and baryons ($n_q = 3$) when compared at the same transverse kinetic energy per constituent quark (KE_T/n_q , where $KE_T = \sqrt{m^2 + p_T^2} - m$). This empirical scaling may indicate that final-state

hadrons are formed through recombination of quarks,^{79–81} possibly providing evidence of deconfinement of quarks and gluons in these systems. This quark number scaling is found to be also valid within about 10% in high-multiplicity p-Pb collisions as shown in Fig. 14 for K_S^0 and $\Lambda/\bar{\Lambda}$ particles. At similar multiplicities, the scaling holds better in the smaller p-Pb system than Pb-Pb system. Although the idea of quark coalescence is remarkably simple, the detailed dynamics of quark recombination are far from fully understood. The observed constituent quark scaling in small systems may help elucidate this phenomena.

3.4. Flow factorization

When experimentally extracting the single-particle anisotropy v_n from multi-particle correlations the assumption is made that the multi-particle momentum distribution can be factorized into a product of single-particle distributions in each event,

$$\frac{d^{3n}N}{d\mathbf{p}_1 d\mathbf{p}_2 \cdots d\mathbf{p}_n} = \frac{d^3N}{d\mathbf{p}_1} \frac{d^3N}{d\mathbf{p}_2} \cdots \frac{d^3N}{d\mathbf{p}_n}. \quad (4)$$

The factorization assumption in equation 4 is broken by short-range correlations, for example, from jets, resonances, and momentum conservation. However, over a wide rapidity range (e.g., $|\Delta\eta| > 2$) in A-A collisions, the predominant source of long-range correlations comes from an expanding fluid-like system with a common preferred flow direction (i.e., short-axis of the elliptical overlap region, or “event plane”). Other possible sources include back-to-back jet correlations on the away side but their contributions are negligible, especially for central A-A collisions, since they are strongly suppressed by the large multiplicity ($1/N_{\text{trk}}$) and also by the effect of jet quenching. Therefore, the relation in Eq. 4 holds and single-particle v_n can be extracted from the measurement of particle correlations. The factorization assumption has always been explicitly or implicitly applied in all methods of measuring anisotropic flow. Any breakdown of factorization would be an indication of correlations not originated from hydrodynamic flow.

However, it was realized recently that even if all particles were to originate from a hydrodynamically flowing medium, the lumpy energy density distribution in the initial state would also break the factorization relation.^{83,85} This is because particles produced at different p_T and η do not in general share a common flow direction, or event plane. The breakdown of the factorization relation as a function of particle’s p_T and η may provide information on the details of initial-state fluctuations, or more specifically, the lumpiness of the initial-state geometry.

The p_T dependence of factorization breakdown has been quantified in terms of a factorization ratio,

$$r_n(p_T^a, p_T^b) \equiv \frac{V_{n\Delta}(p_T^a, p_T^b)}{\sqrt{V_{n\Delta}(p_T^a, p_T^a)V_{n\Delta}(p_T^b, p_T^b)}}, \quad (5)$$

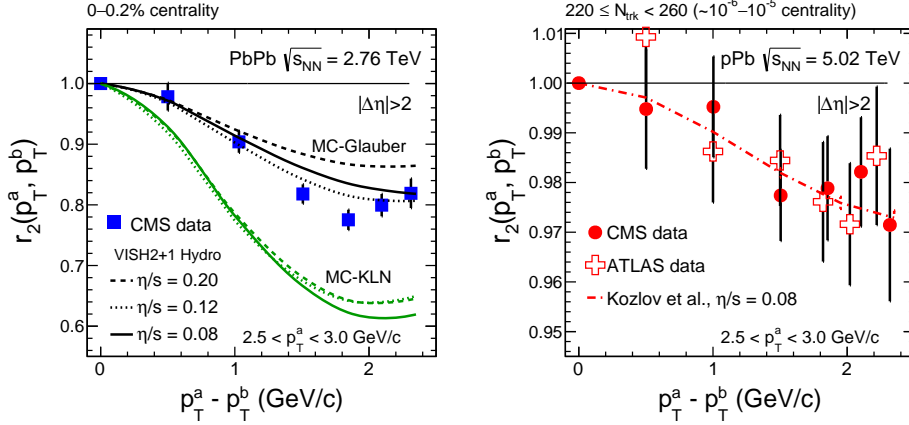


Fig. 15. Elliptic flow factorization ratio, $r_2(p_T^a, p_T^b)$, as a function of $p_T^a - p_T^b$, for $2.5 < p_T^a < 3.0$ GeV/c in ultra-central (0–0.2% centrality) Pb-Pb collisions at $\sqrt{s_{NN}} = 2.76$ TeV⁸² (left) and high-multiplicity p-Pb collisions at $\sqrt{s_{NN}} = 5.02$ TeV^{25, 37, 82} (right), compared to theoretical calculations in hydrodynamic models.^{83, 84}

where $V_{n\Delta}(p_T^a, p_T^b)$ represents the Fourier coefficient of two-particle azimuthal correlations for a given (p_T^a, p_T^b) range. The data are shown in Fig. 15 for ultra-central (0–0.2% centrality) Pb-Pb (left) and high-multiplicity p-Pb (right) collisions. If the factorization relation holds, $r_2(p_T^a, p_T^b)$ will be constant at unity. Up to 20% deviation from unity of r_2 has been observed in ultra-central Pb-Pb collisions, which is consistent with hydrodynamic calculations using a Glauber initial condition, while the MC-KLN initial condition predicted a much larger effect.⁸³ This quantify is found to be insensitive to the η/s value, providing very powerful constraints to models of initial-state fluctuations. Many follow-up theoretical studies showed that the magnitude of factorization breakdown is strongly correlated with the granularity of initial-state fluctuations.^{84, 86–88} A lumpy initial state with larger radial excitations would lead to a more significant breakdown of flow factorization, as seen in ultra-central Pb-Pb collisions. On the other hand, very little effect is found in high-multiplicity p-Pb collisions (Fig. 15, right). This may reflect a relatively larger granularity of initial-state fluctuations in p-Pb with respect to its smaller system size. Or in other words, a p-Pb system is relatively smoother than an ultra-central Pb-Pb system. Note that for both systems, there is almost no average geometry. Any final-state anisotropy is entirely generated by fluctuations.

3.5. Femtoscopy from Hanbury-Brown-Twiss correlations

Hanbury-Brown-Twiss (HBT) correlations provide crucial space time information of the source at the freezeout surface. The extracted femtoscopic radii in various collisions systems from p-p, p-A and A-A at RHIC and the LHC are summarized in Fig. 16 as a function of event multiplicity.⁸⁹ The femtoscopic radii follow a linear

$N_{\text{trk}}^{1/3}$ dependence for all systems, although the slopes are somewhat different. At similar multiplicities, the femtoscopic radii (extracted from a Gaussian fit to the two-particle correlation function) in p-Pb collisions is about 15–20% larger than that in p-p collisions. Both are significantly smaller than the value in Pb-Pb collisions, possibly due to a smaller initial system size. We will return to the discussion of HBT correlations when we present the details of hydrodynamic model calculations in later sections.

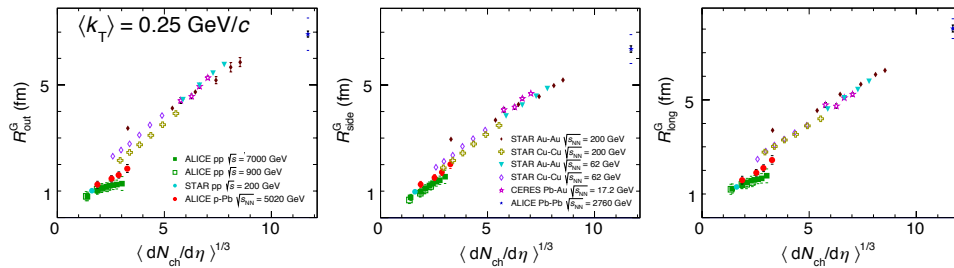


Fig. 16. Comparison of femtoscopic radii (extracted from a Gaussian fit to the two-particle correlation function), as a function of charged-particle multiplicity, measured for various collision systems and energies.⁸⁹

3.6. Heavy flavor production

Production of heavy flavor quarks in p-p and p-Pb collisions has also been studied as a function of multiplicity. Studies of heavy quarkonia states (e.g., J/Ψ , Υ) in heavy ion collisions can probe the possible onset of color screening from a deconfined QGP medium.⁹⁰ An intriguing multiplicity dependence of the $\Upsilon(2S)$ to $\Upsilon(1S)$ yield ratio from p-p, p-Pb to Pb-Pb collisions has been observed by the CMS collaboration.⁹¹ The yield of the $\Upsilon(2S)$ state is suppressed relative to the $\Upsilon(1S)$ state as multiplicity increases in p-p and p-Pb collisions. Although limited in multiplicity reach, the amount of relative suppression has a tendency of smoothly extrapolating to the values measured in Pb-Pb collisions at higher multiplicities. This may be a hint that similar medium effects on the Υ states become significant in p-p and p-Pb collisions as multiplicity increases. However, more studies are still needed to exclude any possible bias introduced by the multiplicity selection.

Open heavy flavor production has been measured in p-p collisions as a function of multiplicity by the ALICE collaboration.⁹² The yields of open charm D^0 , D^+ and D^{*+} mesons as a function of multiplicity in p-p collisions at $\sqrt{s} = 7 \text{ TeV}$ are shown in Fig. 17. Both the yield (y-axis) and multiplicity (x-axis) are normalized by the average values from minimum bias events. The open charm meson yields first linearly increase with multiplicity, which is consistent with the expectation of independent multiple parton interactions. At above 3–4 times the average minimum

bias multiplicity, the increase in yield becomes much faster than linear. Around a similar multiplicity region, the long-range ridge correlations also start becoming significant. These observations suggest the emergence of new dynamic processes in very high-multiplicity p-p collisions.

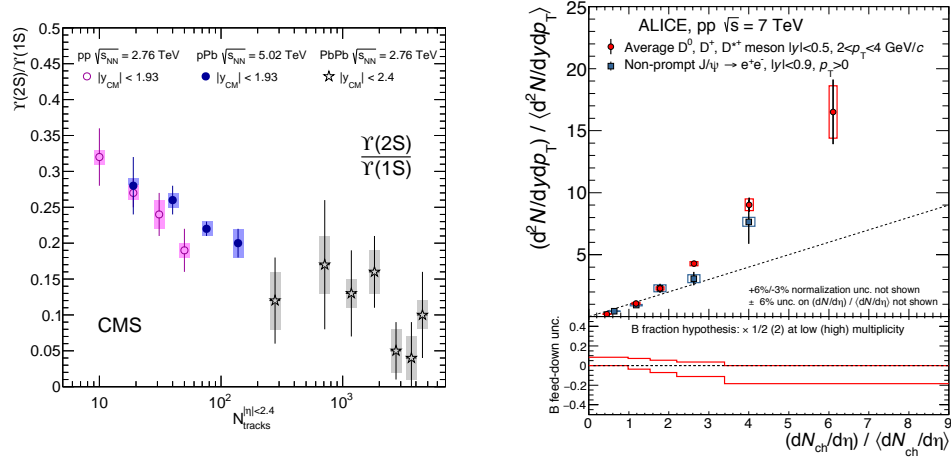


Fig. 17. Left: ratios of $\Upsilon(2S)$ to $\Upsilon(1S)$ yields as a function of charged-particle multiplicity in p-p collisions at $\sqrt{s} = 7$ TeV, p-Pb at $\sqrt{s_{NN}} = 5.02$ TeV and Pb-Pb at $\sqrt{s_{NN}} = 2.76$ TeV.⁹¹ Right: average D meson and non-prompt J/Ψ relative (to minimum bias events) yields as a function of the relative (to minimum bias events) charged-particle multiplicity at midrapidity in p-p collisions at $\sqrt{s} = 7$ TeV.⁹²

4. Theoretical interpretations

Since the 2010 discovery of the ridge in p-p collisions by the CMS collaboration there has been a flurry of theoretical work to uncover its origin. Five years later, as the dust has started to settle, the heavy-ion community has ruled out and refined various models. In this section we will provide an overview of some of the theoretical ideas on the market, focusing on those that confront the data on a quantitative level.

The dialogue in the heavy-ion community has been divided between initial-state and final-state models depending on whether the momentum space anisotropy is established at the moment of particle production or subsequently during strong final state interactions, or (while clearly not equivalent but sometimes used interchangeably) non-hydrodynamic vs hydrodynamic descriptions. However, hydrodynamics is an effective description of the long wavelength, small frequency limit of an underlying theory. Concluding that a system behaves hydrodynamically does not provide any information about the underlying physical processes. Also, for some cases, it is debatable if the model is initial- or final-state. With that being said, we will adopt the usual classification and identify models as non-hydrodynamic (initial-state) or

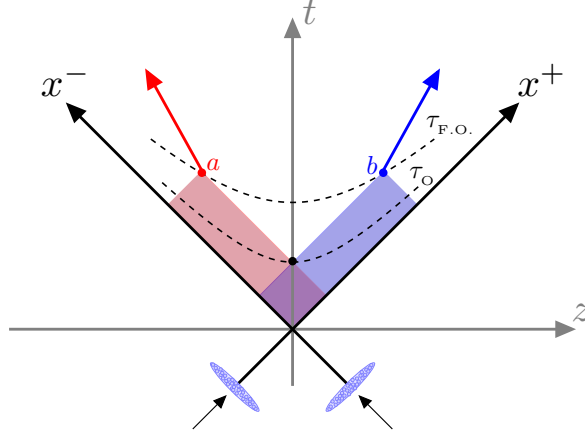


Fig. 18. Space-time diagram showing the causal relation between particles a and b . Particle a and b are causally connected to the red and blue patches respectively. The correlation between them must have formed in their overlap at a proper-time before τ_{O} .

hydrodynamic (final-state) in order to classify different approaches conveniently.

All theoretical models that we consider have a common theme that makes them particularly interesting; correlations between pairs of rapidity-separated particles must have formed at early times.⁹³ In particular, if two correlated particles *freeze out* at a proper time $\tau_{\text{F.O.}}$ then causality dictates that the correlation must have formed at an earlier proper time τ_{O} constrained by

$$\tau_{\text{O}} \leq \tau_{\text{F.O.}} \exp\left(-\frac{1}{2}|y_a - y_b|\right), \quad (6)$$

where $y_{a,b}$ is the momentum-space rapidity of particles a, b . This relation can be derived by considering two particles at space-time rapidities η_a and η_b . Assume particle a emits a signal at time $t_a = \tau_{\text{O}} \cosh \eta_a$ which is subsequently received by particle b at time $t_b = \tau_{\text{F.O.}} \cosh \eta_b$. The distance the signal must travel is $|z_a - z_b| = |\tau_{\text{F.O.}} \sinh \eta_b - \tau_{\text{O}} \sinh \eta_a|$. Causality restricts $|z_b - z_a| \leq c(t_b - t_a)$ and therefore $\tau_{\text{O}} \leq \tau_{\text{F.O.}} \exp(-|\eta_b - \eta_a|)$.

The factor of 1/2 in equation (6) is obtained by introducing a third mutually correlated particle at rapidity η_c . If this third particle were to emit two signals at time τ_{O} particle a and b can be correlated as long as $\tau_{\text{O}} \leq \tau_{\text{F.O.}} \exp(-|\eta_a - \eta_c|)$ and $\tau_{\text{O}} \leq \tau_{\text{F.O.}} \exp(-|\eta_b - \eta_c|)$. We arrive at the most stringent condition for τ_{O} when the third particle, particle c , is located at mid-rapidity, $(\eta_a + \eta_b)/2$, and find

$$\tau_{\text{O}} \leq \tau_{\text{F.O.}} \exp\left(-\frac{1}{2}|\eta_a - \eta_b|\right). \quad (7)$$

The final step in arriving at the desired result of equation (6), is equating the space-time rapidity with the momentum-space rapidity (*i.e.* $\eta \sim y$ in the notation

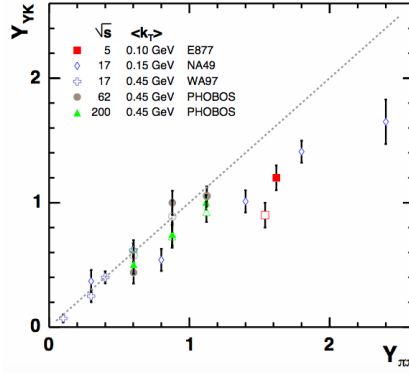


Fig. 19. Yano-Koonin source velocity, Y_{YK} versus pair momentum $Y_{\pi\pi}$ demonstrating approximate boost-invariant longitudinal expansion.⁹⁷

used throughout this section). This is natural at high energies; Lorentz contraction makes the nuclei infinitely thin in the center of mass frame and there is no dimensionful scale in the longitudinal direction. Under a boost-invariant expansion the longitudinal flow of the system has the scale invariant form $v_L = z/t$ and therefore $\eta = y$.

However, it is not a priori the case that this scaling is maintained by the subsequent dynamics. Once an additional scale is introduced the strict scaling relation $v_L = z/t$ may no longer hold. For example, in thermal equilibrium the particle distribution has the form

$$f \sim \exp\left(-\frac{m_{\perp}}{T} \cosh(y - \eta)\right) \quad (8)$$

A thermal smearing of about one unit in rapidity can be expected as long as $m_{\perp}/T \gtrsim 1$. On the other hand, if $p_T \ll T$ the correspondence between η and y is completely lost.

The best empirical evidence for a rigid correlation between the space-time rapidity η and momentum-space rapidity y comes from studying the Yano-Koonin-Podgoretskiĭ (YKP) parameterization^{94,95} of measured Hanbury Brown-Twiss (HBT) correlation functions. The relationship between the Yano-Koonin source velocity, $Y_{YK} = \tanh^{-1} v_{YK}$, and pair momentum $Y_{\pi\pi} = \frac{1}{2} \log\left(\frac{E_a + E_b + p_{za} + p_{zb}}{E_a + E_b - p_{za} - p_{zb}}\right)$ allows for testing the longitudinal expansion.⁹⁶ For a non-expanding source Y_{YK} would be independent of $Y_{\pi\pi}$. For a source undergoing a boost invariant expansion $Y_{YK} = Y_{\pi\pi}$, and this appears to be satisfied by the available data at RHIC as shown in figure 19.

There seems to be a compelling case that the bulk of particle production is approximately boost invariant and the above causality arguments are well founded. The proceeding discussion has far-reaching implications on our understanding of long-range correlations.

The PHOBOS collaboration has observed that the near-side ridge signal in heavy-ion collisions persists up to six units in rapidity separation.^{98,99} Using a very conservative estimate of $\tau_{F.O.} \sim 10$ fm/c these correlations must have been established well before $\tau \sim 0.5$ fm/c. Long-range rapidity correlations thus probe early space-time dynamics and are therefore particularly well suited for studying novel QCD processes. For example, it has been argued that long range correlations may be a useful tool for probing high energy evolution of multi-parton correlations in the nuclear wavefunction.¹⁰⁰

4.1. *Final-state interactions: hydrodynamics in small systems*

From the earliest days of RHIC, hydrodynamics has been very successful in describing the bulk properties of heavy-ion collisions.^{72,101–103} Ideal hydrodynamics, which neglects viscous corrections, was able to reproduce the trends seen in experimental data, in particular the centrality and transverse momentum dependence of particle spectra and elliptic flow. Subsequent developments in the description of the initial state, in particular the inclusion of event-by-event fluctuations, and in the extension of the formalism to include off-equilibrium corrections like those introduced by a non-zero shear viscosity, have advanced the theoretical modeling significantly.^{14,104} Quantitative agreement of viscous relativistic fluid dynamics with a wide range of experimental data is excellent (see Fig. 20), and recent improvements such as the inclusion of bulk viscosity and microscopic transport for the later stages of the collision improve the agreement even more.¹⁰⁵

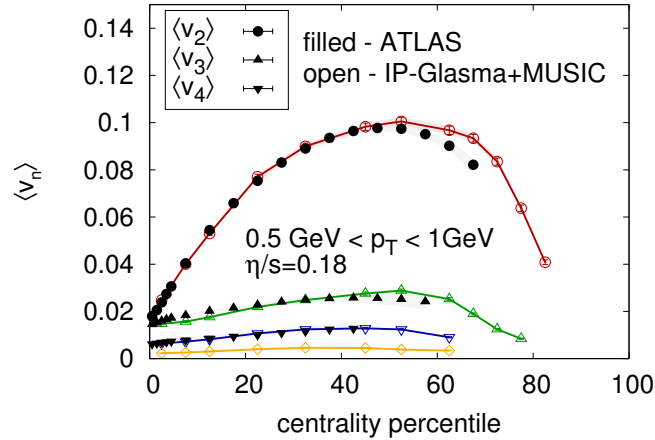


Fig. 20. Model calculations using a constant shear viscosity to entropy density ratio $\eta/s = 0.18$ for v_n vs. collision centrality in Pb-Pb collisions at $\sqrt{s_{NN}} = 2.76$ TeV compared to experimental measurements.^{106,107}

The similarity of experimental data for multi-particle correlations in small sys-

tems with those in heavy ion collisions (see Sec. 3) suggests that the physical processes responsible for the observed correlations may be the same in both systems. More explicitly, hydrodynamics could also be the appropriate model to describe high multiplicity p-p and p-A collisions.

While the applicability of hydrodynamics in very small systems should definitely be questioned (and we will discuss this issue in detail below), the earliest discussion of (ideal) relativistic hydrodynamics to describe nuclear collisions involved p-p collisions.^{108,109} Following the early argument by Landau, hydrodynamics should be applicable if at the moment of collision, a large number of “particles” is created, the “collision mean free path” in the created system is small compared with its dimensions, and a statistical equilibrium is established. We use quotation marks because the definition of particle number and mean free path may be ambiguous in a strongly interacting system.

More recently hydrodynamic calculations aiming at the prediction and description of experimental data for small collision systems at RHIC and LHC have become available.^{74, 75, 106, 110–114} In particular, p-A and d-Au collisions at high energy were explored early on, and predictions showed qualitative agreement with subsequently published experimental data (albeit at different collision energies).

In the following we will discuss the ingredients of these calculations, emphasizing the differences between the calculations of various groups. We will see in particular that results for anisotropic flow are highly sensitive to assumptions about the initial state and its fluctuating structure.

4.1.1. *Modeling of the initial state*

The most important ingredient in the hydrodynamic description of small collision systems is the modeling of the initial geometry. Fluctuations in the initial energy density that deviate from sphericity propagate hydrodynamically and generate non-zero flow harmonics. In practice the initial state geometry is generated by doing event-by-event calculations where fluctuations of density distributions inside the incoming nuclei or hadrons are taken into account. In many calculations these fluctuations are dominated (or exclusively given) by the random positions of nucleons in a nucleus. However, in collisions of a single proton with a large nucleus the substructure of the proton may become important.

We present the details of the initial state model calculations that have been employed for the description of p-A collisions below. These are the Monte Carlo (MC) Glauber model,¹¹⁵ the IP-Glasma model,^{34, 116} and EPOS.¹¹⁴

Monte Carlo Glauber model We follow the discussion in the literature to introduce the implementation of the Monte Carlo (MC) Glauber model for p-A collisions.¹¹⁷

In the MC Glauber model, which has been fairly successful in describing experimental data from heavy ion collisions,¹¹⁵ the proton and the energy deposited

per wounded (participating) nucleon are assumed to be spherical. Hence, in p-A collisions the fluctuating shape of the interaction region is solely due to the random positions of struck nucleons in the heavy nucleus.

The specific implementation we discuss here¹¹⁷ uses GLISSANDO,¹¹⁸ where the entropy deposited per wounded nucleon (or binary collision) fluctuates according to a gamma distribution in order that the final multiplicity distribution reproduces the empirically observed negative binomial. The width of each Gaussian shaped (in transverse space) contribution to the entropy density is chosen to be 0.4 fm.

To determine whether a nucleon was wounded, a Gaussian wounding profile is used. This means that a nucleon undergoes a collision with probability

$$P(b) = A \exp(-\pi A b^2 / \sigma_{\text{NN}}), \quad (9)$$

where b is the distance to the nucleon it is potentially colliding with, σ_{NN} is the nucleon nucleon cross section, and A is a constant chosen to be 0.92.

This method leads to a fairly large interaction region, much larger than the size of the incoming proton. This is illustrated in Fig. 21 a). If one chooses the alternative method of depositing energy around the interaction point of two nucleons, the average size is reduced by approximately 40%.^{117a}

In 3+1 dimensional simulations,^{84,117} the initial entropy density needs to be defined in the space-time rapidity direction as well. Typically one assumes the factorization of the transverse and longitudinal distributions. Assuming that the transverse distribution is independent of rapidity within some range around mid-rapidity is important to reproduce the experimentally observed ridge structure: Having the same initial transverse geometry at different space-time rapidities, leads to correlations between the flow pattern of particles emerging with different momentum rapidities. The typical profile in space-time rapidity is given by a combination of a linearly dropping central region and two half Gaussians at large (positive and negative) rapidities:

$$\rho(\eta_s) = \exp\left(-\frac{(|\eta_s| - \eta_0)^2}{2\sigma_\eta^2}\theta(|\eta_s| - \eta_0)\right) \left(1 \pm \frac{\eta_s}{y_{\text{beam}}}\right) \theta(y_{\text{beam}} \pm \eta_s). \quad (10)$$

The linear drop away from the nucleon introduces a torque effect and some small fluctuation in the longitudinal direction. The parameters typically chosen^{84,117} in calculations for p-A collisions at $\sqrt{s} = 5.02$ TeV are $\eta_0 = 2.5$, $\sigma_\eta = 1.4$, and $y_{\text{beam}} = 8.58$. Another parameter is the initial time that the hydrodynamic calculation starts, typically chosen between $\tau_0 = 0.2$ fm/ c and $\tau_0 = 0.6$ fm/ c .

Since in the hydrodynamic framework the final flow anisotropy is driven by the initial state eccentricity, we define it here and will refer to it later in the text when discussing how different initial state models generate different geometries. The n 'th order eccentricity is given by^{26,29}

^aAlso using the black disk approximation, where a collision only occurs if $b < R = \sqrt{\sigma_{\text{NN}}/\pi}$, leads to smaller interaction regions.

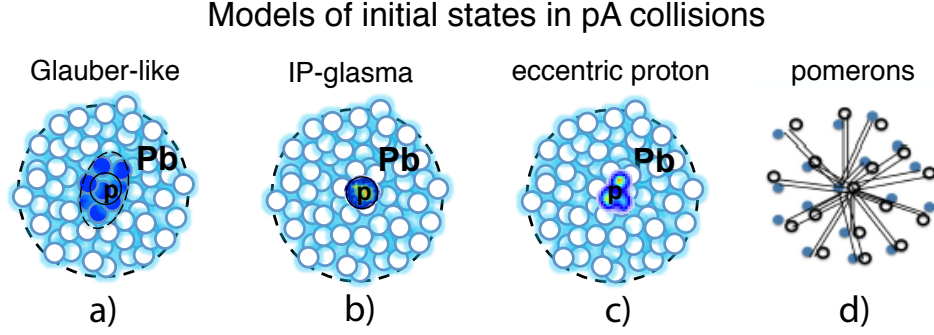


Fig. 21. Typical geometric configurations generated by different initial state models for p-A collisions: a) MC-Glauber with wounded nucleons as sources b) IP-Glasma with round proton c) IP-Glasma with an eccentric proton d) Pomerons.

$$\varepsilon_n = \frac{\sqrt{\langle r^n \cos(n\phi) \rangle^2 + \langle r^n \sin(n\phi) \rangle^2}}{\langle r^n \rangle}, \quad (11)$$

where $\langle \cdot \rangle$ is the energy density (or entropy density) weighted average, and r and ϕ are the polar coordinates in the plane transverse to the collision axis.

IP-Glasma model The Impact Parameter (IP) dependent Glasma model^{34, 116} is based on the color glass condensate framework¹¹⁹ and uses the IP-Sat model¹²⁰ to constrain the impact parameter and gluon momentum fraction dependence of the dipole cross section. This, together with fluctuating nucleon positions for heavy ions determines the initial distribution of color charges, which then enter the currents in the Yang-Mills equations that determine the initial gluon fields. The assumption in this model being that at high energies the QCD coupling constant is small^b and the occupation numbers of gluons are non-perturbatively large ($\sim 1/\alpha_s$). In this limit the dynamics can be approximated classically by the Yang-Mills equations describing both the initial configuration of gluon fields and their dynamical evolution.^{121–126} For heavy ion collisions at high energies these assumptions are likely to be valid. For smaller systems, such as p-A collisions, the approximations might be appropriate for high multiplicity events. Details on the implementation in A-A collisions^{116, 127} and p-A collision can be found in the literature.^{106, 127} Here we list the main ingredients of the IP-Glasma model:

- (1) IP-Sat parametrization of the saturation scale $Q_s(x, \mathbf{x}_T)$ and fixed parameters from DIS data.^{120, 128, 129}

^bThe coupling is determined at the dynamically generated saturation scale Q_s , which grows with increasing energy.

- (2) Monte Carlo sampling of nucleon positions in the incoming nucleons and the impact parameter \mathbf{b} .
- (3) Determination of the thickness function as a function of \mathbf{x}_T , $T(\mathbf{x}_T)$, in each nucleus using information from (2). Using (1), this results in the distribution of $Q_s(\mathbf{x}_T)$ at the collision energy of interest.
- (4) Using a proportionality constant of order 1 that allows the conversion from Q_s to the color charge density $g^2\mu$ leads to the color charge density distribution in each nucleus. This proportionality constant can fluctuate to account for the effect of gluon number fluctuations. See discussion below.
- (5) Monte Carlo sampling of color charges ρ^a (with color index a) for each nucleus from the color charge density distribution, assuming

$$\langle \rho^a(\mathbf{x}_T)\rho^b(\mathbf{y}_T) \rangle = g^2\mu^2(x, \mathbf{x}_T)\delta^{ab}\delta^{(2)}(\mathbf{x}_T - \mathbf{y}_T). \quad (12)$$

- (6) Solution of the Yang Mills equation

$$[D_\mu, F^{\mu\nu}] = J^\nu, \quad (13)$$

for each nucleus with the color currents given by

$$J^\nu = \delta^{\nu\pm}\rho^a(x^\mp, \mathbf{x}_T)t^a, \quad (14)$$

where $+$ and $-$ are for right moving and left moving nuclei, respectively. t^a are the generators of SU(3).

- (7) Numerical solution for the gluon fields after the collision at time $\tau = 0^+$.^{121, 130}

$$A^i = A_{(A)}^i + A_{(B)}^i, \quad (15)$$

$$A^\eta = \frac{ig}{2} [A_{(A)}^i, A_{(B)}^i], \quad (16)$$

$$\partial_\tau A^i = 0, \quad (17)$$

$$\partial_\tau A^\eta = 0, \quad (18)$$

where (A) and (B) denote fields of the two colliding nuclei.

- (8) Solution of the source-free Yang-Mills equation to obtain the time evolution of the produced gluon fields.
- (9) Landau matching of the gluon-field energy momentum tensor to obtain the relevant quantities for fluid dynamic calculations: energy density $\varepsilon(\mathbf{x}_T)$ and flow velocities $u^\mu(\mathbf{x}_T)$.

Note that initial conditions obtained with this model are boost invariant, which is a good approximation for high energy collisions and rapidities not too far away from mid-rapidity.

We will now discuss specific features of the model relevant for small collision systems. Due to the fluctuating color charges, gluon multiplicity distributions in the IP-Glasma model already include negative binomial fluctuations.^{34, 127} It was however discovered that for p-p and p-A collisions additional fluctuations (as compared to the original model³⁴) of the color charge density were needed to describe

the experimental multiplicity distributions (see also Fig. 35). These fluctuations can be understood as fluctuations of the gluon number for a given value of the saturation scale Q_s . The comparison of gluon with hadron distributions is of course only qualitative and additional fluctuations from the hadronization mechanism are also expected to modify the result. Nevertheless, it is important to include the gluon number fluctuations to allow for rare fluctuations that generate the high multiplicity events of interest.

Turning to the initial geometry, the IP-Glasma model generates interaction regions in the transverse plane that are dominated by the smaller of the two colliding objects. This is because energy is only deposited where both nuclei's gluon fields are non-zero (otherwise the fields are pure gauge fields and indistinguishable from the vacuum). For a proton colliding with a large nucleus (not too close to its edge), the interaction region is thus strongly affected by the shape of the proton. This behavior leads to much smaller interaction regions than in the Monte Carlo Glauber model as illustrated in Fig. 21 b). Furthermore, if the proton is assumed to be round (up to fluctuations of the color charges ρ^a), initial eccentricities as defined in (11) are very small.

EPOS The EPOS model^{74, 131, 132} has successfully been applied to describe experimental data from both p-p and p-Pb collisions. EPOS includes both a fluctuating initial state and hydrodynamic evolution, as well as jets and the interaction between jets and the medium. The initial state calculation is based on multiple scatterings, where initial state radiation is included. Thus, the model deals with parton ladders or “Pomerons”. The Pomerons, whose number determines the multiplicity, are placed in between two colliding partons, which are distributed around the center of nucleons according to an exponential distribution. In addition, the pomerons carry a transverse momentum (generated by the initial scattering) and thus move transversely even before the coupling to hydrodynamics occurs. EPOS does not assume boost invariance but produces a smoothly changing longitudinal energy density distribution. It should be noted that EPOS also needs to include saturation effects in order to not violate unitarity. It is done by introducing an energy dependent saturation scale for each Pomeron.⁷⁴

Holographic pomerons Following the AdS/CFT conjecture¹³³ a reggeized and unitarized scattering amplitude was derived for $\mathcal{N} = 4$ SYM in the limit of large N , strong coupling $g_{YM}^2 N \gg 1$ and high energy.¹³⁴ In¹³⁵ it was recognized that a single closed string exchange contribution to the eikonized dipole-dipole scattering amplitude yields a Regge behavior of the elastic amplitude, with features consistent with experimental data.

This Regge behavior is driven by worldsheet instantons, which describe the Schwinger mechanism for string pair creation by an electric field, where the longitudinal electric field at the origin of this non-perturbative mechanism is induced by the relative rapidity of the scattering dipoles.

This stringy Schwinger mechanism can generate quantum fluctuations of virtual strings, which take the form of thermal fluctuations with an effective temperature related to the inverse string circumference and therefore impact parameter; at the center of the string $T_{\text{eff}}^{-1} \sim 2\pi|\mathbf{b}_\perp|$. If the impact parameter is small enough there may be a region in the middle of the string where the effective temperature is above the deconfinement temperature suggesting that the string description should be replaced by a plasma phase.¹³⁵

It has been argued that near this critical impact parameter the increased quantum fluctuations reduce the string tension and self-interactions among the strings cause an implosion and formation of a *string ball*.¹³⁶ A more quantitative study of string self-interactions and string ball formation was explored in.^{63,137} At effective temperatures larger than T_c the string ball may form a strongly coupled high density plasma that expands hydrodynamically. One of the key features of the holographic pomerons that may distinguish them from other pictures of plasma formation is the sudden onset of hydrodynamic behavior at a critical impact parameter. However, no explicit hydrodynamic calculations have been performed using this framework.

4.1.2. *Viscous hydrodynamics and its limits of application*

Hydrodynamics is an effective theory for the long wavelength modes of a system able to describe the interactions of the low momentum part of the particle spectrum if, from a kinetic theory point of view, the mean free path of the particles is significantly smaller than the system size. This lead many to criticize the use of viscous fluid dynamics in small colliding systems and indeed one should always check whether hydrodynamics is being applied within its domain of validity. In this section we will first introduce the basic ingredients of viscous relativistic hydrodynamics and quantify the domain of validity more explicitly.

The viscous relativistic fluid dynamic equations for small systems are identical to those employed to describe heavy ion collisions. Various recent reviews cover the details of both the equations and their derivation, as well as the implementation in numerical codes.^{14,104,138}

Here we summarize the most important aspects. Relativistic viscous hydrodynamics is formulated as a gradient expansion to take into account deviations from local thermal equilibrium or ideal hydrodynamics. Due to the acausal behavior of the relativistic equations expanded to first order in gradients, numerical implementations require the inclusion of terms at least of second order in the gradients. Commonly used are Israel-Stewart type equations^{139,140} that were derived using the 14 moment method and the second moment of the Boltzmann equation to determine the hydrodynamic equations for the dissipative currents. Improvements that provide a more systematic expansion were derived more recently.¹⁴¹

Many simulations concentrate on shear viscosity, but some also include bulk viscosity, and possibly the coupling between shear and bulk terms. In fact, the effect of bulk viscosity has been found to be large¹⁰⁵ for certain observables, including spec-

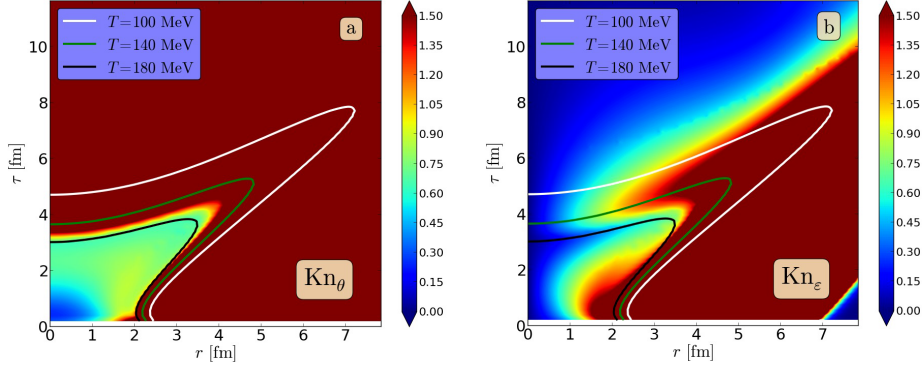


Fig. 22. Space-time evolution of the Knudsen numbers in p-Pb collision at the LHC, with $\eta/s = 0.08$ in the QGP phase and a temperature dependent η/s in the hadron gas phase, and $dN_{\text{ch}}/d\eta = 270$. (a) Kn_θ and (b) Kn_ϵ .¹⁴²

tra and anisotropic flow. However, a large uncertainty arises from off-equilibrium corrections to the particle spectra when converting hydrodynamic quantities to particles at freeze-out, in particular when including bulk viscous corrections.

Large corrections to the equilibrium distribution functions (typically appearing at transverse momenta $p_T \gtrsim 2 \text{ GeV}$) are one indication that the fluid dynamic approximation we are using breaks down. Another, more systematic quantification of the validity of viscous fluid dynamics is provided by the study of Knudsen and Reynolds numbers. The Knudsen number is defined as the ratio of a microscopic to a macroscopic scale in the system. Various choices for these scales are possible, and a variety of them has been studied in both heavy ion collisions and smaller systems.¹⁴² For example, the macroscopic scale can be defined as the inverse of the expansion rate $L_{\text{macro}}^\theta = \theta^{-1} = (\partial_\mu u^\mu)^{-1}$, with u^μ the flow velocity, while the microscopic scale can be described by the shear relaxation time, $l_{\text{micro}} = \tau_\pi$, which in a dilute gas is proportional to the mean free path, $\tau_\pi \sim \lambda_{\text{mfp}}$. So, $Kn_\theta = \tau_\pi \theta$, or alternatively we can define Kn_ϵ , with $L_{\text{macro}}^{-1} = \sqrt{\nabla_\mu \epsilon_0 \nabla^\mu \epsilon_0} / \epsilon_0$, where ϵ_0 is the energy density.

For hydrodynamics to be valid, the Knudsen number should stay significantly below one at all points in space time. Whether this condition is fulfilled was tested for various choices for L_{macro} ¹⁴² and we show examples for p-A collisions in Fig. 22.

One can see that around $T = 100 \text{ MeV}$ the fluid dynamical description is no longer applicable, with all Kn_θ values being above 1.5. The results shown are for a constant $\eta/s = 0.08$ in the QGP phase – if a temperature dependent η/s was used in the QGP phase, the situation would worsen and fluid dynamics would be out of its domain of applicability even in the early stages of the evolution. While large Knudsen numbers indicate the breakdown of hydrodynamics it does not preclude large final state effects. However, it does mean that another framework outside of

hydrodynamics might be more appropriate to model the system when the Knudsen number is large.

4.1.3. Results from hydrodynamics in small systems

We now discuss the results obtained for the Fourier harmonics in small collision systems within various model calculations, beginning with the existing predictions for proton-proton collisions at the LHC and continuing with proton/deuteron on heavy ion collisions. We will then go into more detail with the discussion of more recent, very sophisticated calculations and their results for mean transverse momentum, Fourier harmonics of charged hadrons and identified particles, as well as HBT radii.

Proton-proton collisions Wide ranges of predictions for elliptic flow in proton-proton collisions were published early on - in particular in expectation of LHC results at 7 and 14 GeV. We list several calculations and predicted values for the elliptic flow in p-p collisions in the following.

Ideal hydrodynamic calculations¹⁴³ indicated that $v_2 \sim 0.035$ in p-p collisions, and that any value above 0.02 in minimum bias collisions would indicate an extremely small viscosity (below the KSS bound of $1/4\pi$) of the medium.

In a string percolation model that includes a directional dependence of the sources, a sizable v_2 was predicted for p-p collisions.¹⁴⁴ Various scenarios including different shapes of the proton have been studied¹⁴⁵ and estimates of v_2 for p-p collisions depended strongly on the assumed shape, ranging from zero to almost 1.5% for the more realistic models. Similarly strong dependencies on the proton profile were found in hydrodynamic simulations,¹⁴⁶ where very large values for the minimum bias v_2 , ranging from 6% to 25% are quoted.

High multiplicity events were predicted to have an integrated v_2 of around 10%, but again with a wide spread depending on the initial state configuration, when using hydrodynamics after initializing with flux tubes obtained in a constituent quark model.¹⁴⁷ A similar model using partonic interactions determines eccentricities compatible with v_2 values ranging from 10% to 20%, depending on model parameters, when assuming a given relation between eccentricities and elliptic flow values determined from hydrodynamic calculations.¹⁴⁸

Mimicking quantum fluctuations by introducing an eccentricity to the interaction region, and then performing hydrodynamic simulations, a v_2 value of 3% was found if the induced eccentricity has average value of about 17% in another study.¹⁴⁹

Using DIPSY, a Monte Carlo event generator based on the QCD dipole model, to generate the initial conditions and a fixed relation between v_2 and eccentricity, a value of 6% for v_2 in p-p collisions at LHC was estimated, being fairly independent of the multiplicity.¹⁵⁰

In the EPOS framework that performs hydrodynamic expansion based on flux-

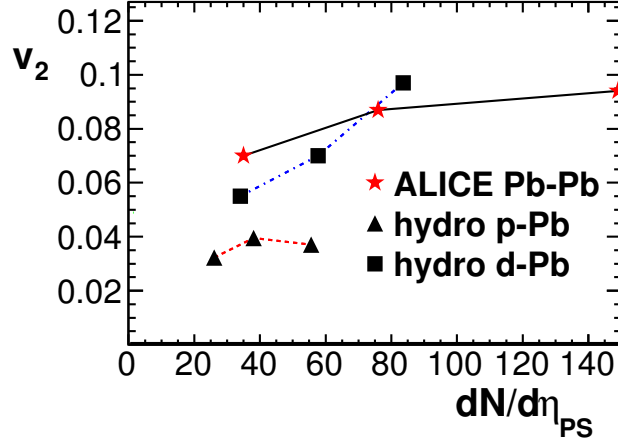


Fig. 23. Predictions for the elliptic flow coefficient v_2 from a 3+1D viscous relativistic hydrodynamic simulation for p-Pb (at $\sqrt{s} = 4.4$ TeV) and d+Pb (at $\sqrt{s} = 3.11$ TeV) collisions, compared to ALICE results for Pb+Pb collisions.^{112, 151}

tube initial conditions as described above, both the experimentally determined mean transverse momentum and measures of the source size were reproduced.¹¹⁰ Furthermore, the ridge structure was reproduced within this model.¹¹¹ This indicates that the elliptic flow component is correctly described by EPOS in p-p collisions.

The conclusion to be drawn from this extremely wide range of predictions is the strong model dependence, in particular on the initial state for hydrodynamic calculations, that one faces when computing v_2 in proton-proton collisions.

Proton-heavy ion collisions Early predictions for flow in d-Pb and p-Pb collisions from hydrodynamic simulations were also presented.¹¹² In this work MC-Glauber initial conditions, as described in Section 4.1.1, were used together with 3+1 dimensional viscous hydrodynamic simulations to obtain results for particle spectra and flow harmonics as functions of transverse momentum and pseudo rapidity.

The elliptic flow is found to be 3%-4% in p-Pb collisions, with little centrality dependence (Fig. 23), significantly smaller than for Pb-Pb collisions with the same multiplicity. For the d-Pb system, the elliptic flow is significantly larger, increasing for central collisions, and reaching almost 10%.

The ridge structure in two-particle correlations was observed in similar hydrodynamic calculations for p-Pb collisions at $\sqrt{s} = 5.02$ TeV.¹¹³ For the largest rapidity gaps considered, v_2 integrated over $0.1 \text{ GeV} < p_T < 2 \text{ GeV}$ was found to be 4%, while the corresponding v_3 was about half as big.

As discussed before, in these calculations the initial interaction region turns out to be rather large when using scaling of the initial energy or entropy density with the participating nucleons. The size and lifetime of the collective source formed in central p-Pb collisions is found to be 3 – 4 fm.

More quantitative results on the size of the emission source using HBT techniques were subsequently presented.¹⁵² Here, an alternative model for the initial distribution was also considered. This “compact” variant locates the sources in the center of mass of nucleon-nucleon collisions. The average rms radii for the two sets of initial conditions considered were 1.5 and 0.9 fm, respectively.

Results obtained for HBT radii as a function of multiplicity were presented in comparison to heavy ion and p-p data.¹⁵² It was found that the p-Pb results for R_{side} , R_{out} , and R_{long} were much closer to the heavy ion results at a given multiplicity than to the p-p results. R_{out} is reduced by 25% when using the compact initialization, while the other radii are little affected. We note that the difference in the initial size of the system has a large effect on the final measured HBT radii. In particular, it was shown¹⁰⁶ that the IP-Glasma model (see Section 4.1.1) produces significantly smaller initial energy density distributions in the transverse plane than either of the MC Glauber models discussed above. In particular, initial sizes in p-Pb collisions were demonstrated to be much closer to those in p-p collisions than Pb-Pb collisions.¹⁰⁶ One would expect that this leads to similar differences for HBT radii obtained in hydro calculations using the different initial state models.

Very detailed analyses of flow in p-Pb collisions using the MC Glauber model including negative binomial fluctuations, which are necessary to reproduce the multiplicity distribution, and in particular its tail at high multiplicity, have been carried out following the first exploratory works.¹¹⁷ Here, the authors employ hydrodynamic simulations followed by statistical freeze-out. The negative binomial fluctuations in the initial state, which cause the deposited entropy per participant nucleon to fluctuate, turn out to be necessary in order to describe the experimental data by increasing the initial eccentricities and thus the resulting $v_2\{2\}$ and $v_2\{4\}$. The successful description of ATLAS data⁵² in this case is presented in Fig. 24.

Comparing to predictions discussed above and shown in Fig. 23, we conclude that (differences from the employed method to determine v_2 aside), large differences result from using different initial state models.

More detailed analyses have demonstrated that various features of the data are naturally reproduced by hydrodynamic calculations, even on a quantitative level. For example, the mass splitting of the mean transverse momentum^{75,84} and the v_2 of identified particles^{74,75} in p-Pb collisions was presented using different initial state descriptions.

We note that hadronic cascade models, such as UrQMD, also reproduce the characteristic mass splitting. UrQMD could however not describe the centrality dependence of the elliptic flow or get a real valued $v_2\{4\}$.¹⁵³ The latter is naturally achieved in hydrodynamic calculations, where all higher order cumulants (from 4, 6, 8 particles, etc.) are equal since all particles are correlated with one another.

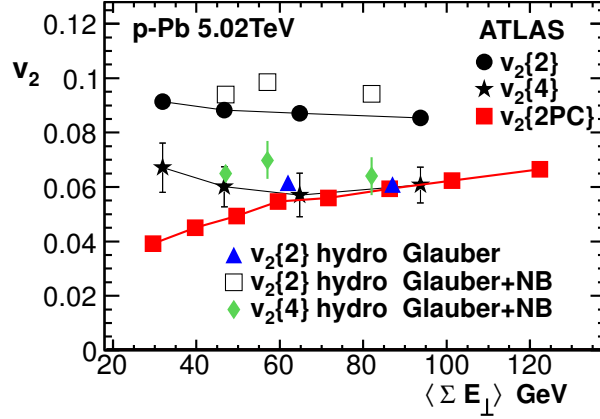


Fig. 24. The elliptic flow coefficient of charged particles for $|\eta| < 2.5$, $0.3 \text{ GeV} < p_T < 5.0 \text{ GeV}$ from the cumulant method $v_2\{2\}$ and $v_2\{4\}$, and from the di-hadron correlation function measured by the ATLAS Collaboration,⁵² compared to hydrodynamic calculations.¹¹⁷ Glauber+NB includes negative binomial fluctuations in the initial entropy density distribution.

The IP-Glasma model produces an initial transverse energy distribution having the shape of the assumed proton shape, and early calculations using a spherical proton therefore yielded a very small v_2 in p-A collisions.¹⁰⁶ However, the process of energy deposition is less ambiguous as in the MC Glauber model, where very different results can be achieved by using different prescriptions for the initial energy/entropy density distributions.

Within the IP-Glasma + hydrodynamics description it is thus clear that the results for azimuthal anisotropies in p-Pb collisions are sensitive to the shape of the proton and its fluctuations event by event.¹⁰⁶

In conclusion, all aspects of the experimental data are at least qualitatively and for the most part also quantitatively described by hydrodynamic calculations. Unfortunately, in addition to the unknown transport parameters, results are highly sensitive to the assumptions made in modeling the initial state. Furthermore, one must scrutinize the applicability of hydrodynamics in these very small systems due to large Knudsen numbers throughout the evolution.

Some support for the applicability of hydrodynamics comes from calculations at large coupling, where it was shown that viscous hydrodynamics describes early on the evolution obtained using AdS/CFT correspondence in a system of colliding shock waves.¹⁵⁴

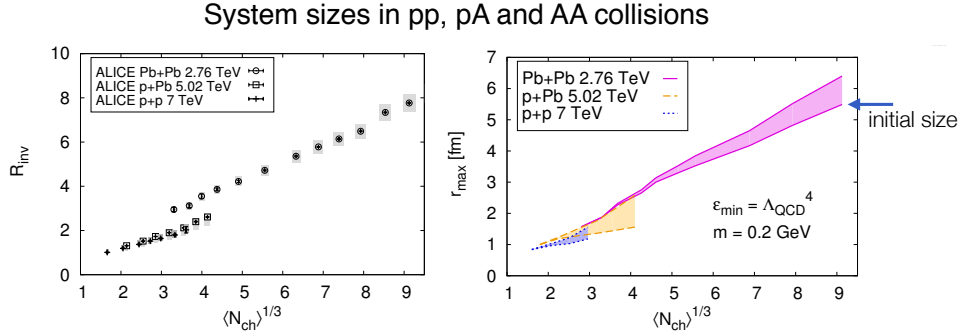


Fig. 25. The experimental radius R_{inv} in p-p, p-Pb, and Pb-Pb collisions from the ALICE collaboration¹⁵⁵ (left) compared to the radius r_{max} in the IP-Glasma (+MUSIC) model.¹⁰⁶ The lower end of the band indicates the initial size, the upper end the maximal size reached during hydrodynamic expansion. Initial sizes are similar in p-p and p-A collisions, while A+A collision systems at the same multiplicity are generally larger. This is a trend reflected also in the experimental HBT radii shown on the left.

HBT radii from hydrodynamics As for the results on the azimuthal anisotropy, results for the system size, mainly characterized by HBT radii (discussed in Section 3.5), vary largely depending on the initial state model. While the IP-Glasma model produces initial sizes that are similar in p-p and p-A collisions, but large in A-A for the same multiplicity, the MC-Glauber model produces larger p-A systems, closer to those in A-A collisions,¹⁵² as illustrated in Fig. 21. While HBT calculations within the IP-Glasma model have yet to be performed, the general trends of the initial size of the system and the measured HBT radii agree very well. In Fig. 25 we compare the experimental data on the left to results for r_{max} on the right. We define r_{max} as the (angle averaged) radius where the system reaches a minimal threshold energy density $\epsilon_{min} = \Lambda_{QCD}^4$. This radius by definition depends on the choice of ϵ_{min} . This choice however only affects the overall normalization of r_{max} ; it does not affect the dependence of r_{max} on the number of charged particles N_{ch} . There is also some dependence on the infrared cutoff m , which has been chosen to be on the order of Λ_{QCD} . This dependence can mostly be absorbed into an overall normalization constant.¹⁰⁶

In summary, the system sizes obtained from experimental HBT measurements are generally compatible with the fluid dynamic picture, while the details, once again, depend strongly on the initial state and its size.

Deuteron/³He-heavy ion collisions Small systems with drastically different geometries from p-A collisions could help distinguish whether the origin of the azimuthal anisotropies measured in p-A collisions could indeed stem from the hydrodynamic response to the initial geometry.

Therefore, the PHENIX experiment has measured v_2 in d-Au and v_2 and v_3 in ³He-Au collisions. Hydrodynamic calculations^{158, 159} predicted a somewhat en-

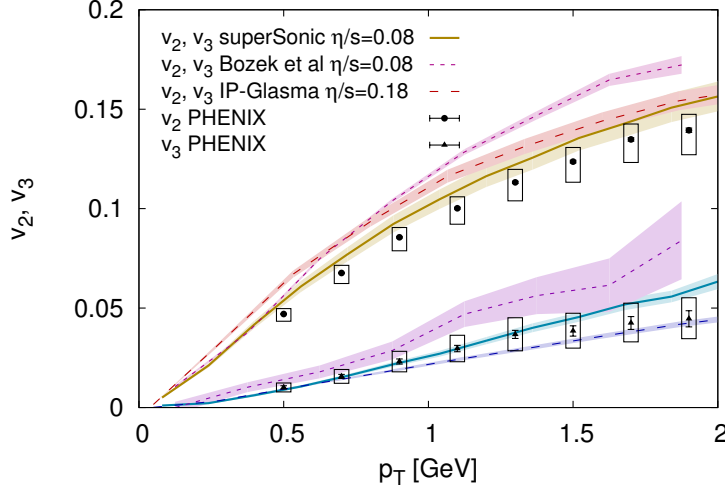


Fig. 26. Experimental results for v_2 and v_3 in ${}^3\text{He}+\text{Au}$ from PHENIX¹² compared to three different hydrodynamic calculations: A prediction using MC Glauber initial conditions,¹⁵⁶ results from superSonic including pre-flow,¹⁵⁷ and IP-Glasma+MUSIC calculation,¹⁵⁸ with increased viscosity of $\eta/s = 0.18$ compared to the original prediction.

hanced v_3 for the ${}^3\text{He}\text{-Au}$ system because of the enhancement of significantly triangular events. Indeed, hydrodynamics can describe the v_n 's also in these two systems.^{156, 157, 160} While some predictions¹⁵⁹ had to be amended with a “pre-flow” component, others¹⁵⁸ need an adjustment of the shear viscosity. Both calculations then lead to good agreement with the experimental data.^{12, 161} In Fig. 26 we show a compilation of results for v_2 and v_3 in ${}^3\text{He}\text{-Au}$ collisions. While some of the calculations, which are predictions, can be improved by varying the shear viscosity, general agreement with the experimental data is very good, for the very different initial conditions. superSonic and IP-Glasma+MUSIC seem to have a somewhat too large ratio of v_2/v_3 . It would be desirable to also experimentally measure v_3 in d-A and p-A collisions to see whether it is indeed enhanced in ${}^3\text{He}\text{-A}$ collisions as expected from the initial geometry and confirmed in hydrodynamic calculations.¹⁵⁷

4.1.4. Parton transport models

Parton transport models describe final state interactions microscopically, including various kinds of processes (elastic, inelastic) and different implementations of cross sections (isotropic, pQCD, ...). If these cross sections are large enough, the microscopic description should approach the hydrodynamic limit, and we expect similar results for flow observables as in (viscous) hydrodynamic simulations.

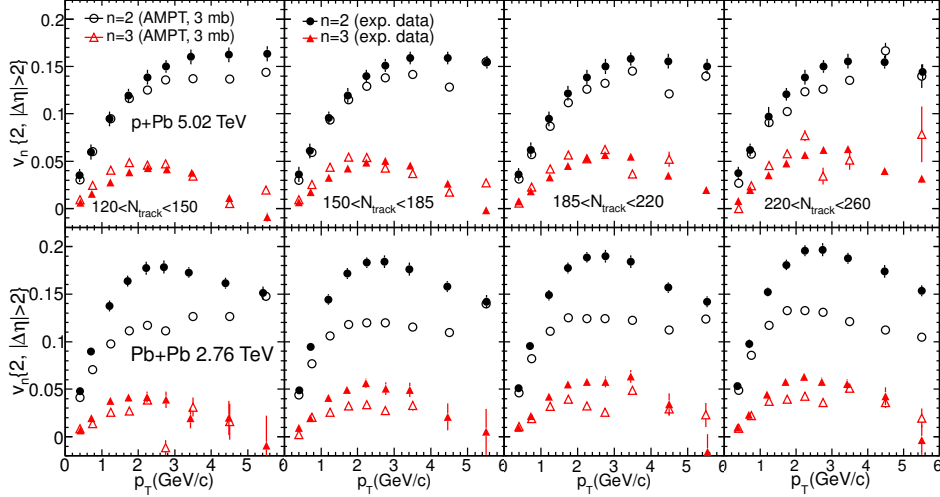


Fig. 27. The transverse momentum dependence of the elliptic, v_2 , and triangular, v_3 , anisotropy coefficients in p-Pb (upper panel) and Pb-Pb collisions (lower panel) from the AMPT model (open symbols) compared to experimental data from CMS (filled symbols). Figure adapted from.¹⁶⁶

AMPT The AMPT model¹⁶² is based on HIJING¹⁶³ to generate the initial state and the parton cascade ZPC¹⁶⁴ that simulates the final state interactions. One important ingredient that allows AMPT to produce enough final state collectivity is the so called string melting mechanism, which converts all initial minijets and soft strings into quarks and anti-quarks. These undergo elastic scatterings with a partonic cross-section which is controlled by the strong coupling constant and the Debye screening mass. After hadrons are formed using a coalescence model, they also interact further.

p-Pb (and p-p) collisions have been studied within the AMPT model in.^{165,166} It was found that with a modest elastic cross section of $\sigma = 1.5 - 3$ mb long range two-particle correlations were well described and the computed v_2 and v_3 agreed well with the experimental data from p-Pb collisions (while v_2 in Pb-Pb collisions was underestimated by the model) - see Fig. 27.

A particularly interesting observation of this study¹⁶⁶ was that on average each parton undergoes only two collisions (and the hadronic cascade had a negligible effect on the results). It is surprising that such a small amount of interactions could lead to the build-up of collective flow.

A possible explanation of the physical process in the AMPT model was given in a recent work,¹⁶⁷ where the details of what partons carry the anisotropy and how it depends on the number of their scatterings were analyzed. It was found that an escape mechanism seems to be responsible for the produced anisotropy in AMPT. The main ingredient of this is the initial spatial anisotropy of the medium and the resulting greater probability for partons to escape along the direction in which the

medium is shorter.

This effect is drastically different from the build-up of hydrodynamic flow, and if it is the main effect, it is somewhat surprising that the transverse momentum dependence of the v_n coefficients is so well reproduced by AMPT.

4.2. *Conclusions on final state interactions in small systems*

In conclusion we can state that it is possible to describe all characteristic features measured in p-p and p/d/ ^3He -A collisions with models based on the collective response to an initial state geometry. In particular hydrodynamic models can reproduce the azimuthal anisotropies of charged hadrons v_n , the mass splitting of the mean transverse momentum and v_2 for identified particles, and the HBT radii. However, for all observables there is a significant uncertainty related to the little knowledge we have about the initial state in small systems. Depending on the assumptions made about how the initial shape of the system is generated, final results can vary dramatically. Apart from this caveat, the Knudsen number can take on rather large values in viscous hydrodynamic simulations of small systems. Thus, the quantitative results could be plagued with errors due to running hydrodynamics at least partly outside its domain of applicability.

4.3. *Multi-particle production in the Color Glass Condensate*

Introduction to the Color Glass Condensate A first attempt at understanding the nature of multi-particle correlations should come from studying the production processes dictated by QCD. Traditionally this is done in the framework of collinear factorization where the strong interaction processes are factorized into a product of cross sections convoluted with parton distribution functions. This approach is valid in the Bjorken (or short distance) limit,

$$\Lambda_{\text{QCD}} \ll Q \sim x\sqrt{s} \sim \sqrt{s} \quad (19)$$

where Q is the kinematic energy scale of the scattering process, and x the Bjorken x , *i.e.*, the longitudinal momentum fraction of the parton in the infinite momentum frame. Requiring the independence of an energy scale μ separating of the long distance physics encoded in the parton distribution functions from the short distance QCD matrix elements leads to the DGLAP (Dokshitzer-Gribov-Lipatov-Altarelli-Parisi)^{168–170} renormalization group equation. By construction the DGLAP equation resums collinear logarithms of the form $\alpha_s \ln(Q^2/\Lambda_{\text{QCD}}^2)$.

However, most of the particle production and the bulk of QCD phenomena occurs at low Q and therefore we consider QCD in the Regge-Gribov (or high energy) limit,

$$\Lambda_{\text{QCD}} \ll k_{\perp} \sim x\sqrt{s} \ll \sqrt{s} \quad (20)$$

where another class of large logarithms, $\alpha_s \ln(1/x)$, must be resummed, in this case by the Balitski-Fadin-Kuraev-Lipatov (BFKL) equation.^{171,172} The rapid rise in

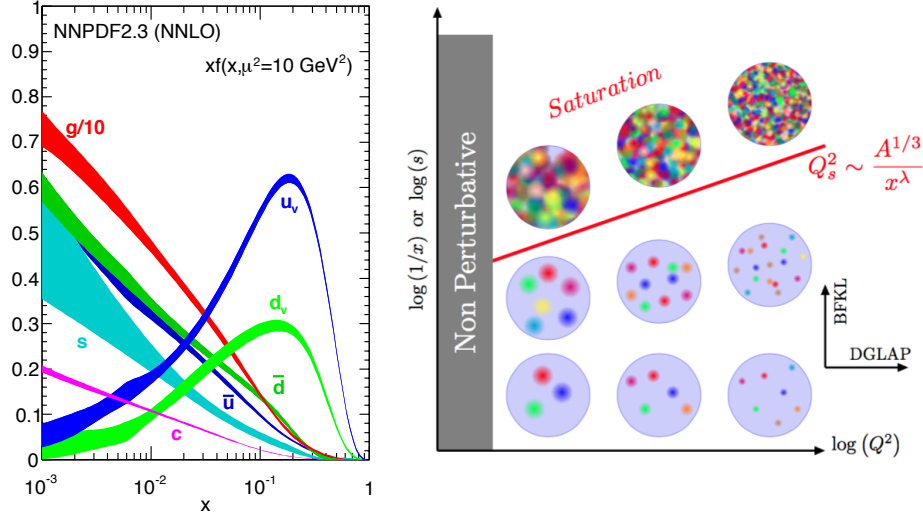


Fig. 28. Left: Longitudinal momentum fraction, x , times the unpolarized parton distributions obtained in NNLO NNPDF2.3 global analysis¹⁷⁴ at scale $\mu^2 = 10 \text{ GeV}^2$. Figure adopted from.¹⁷⁵ Right: Evolution of the saturation scale Q_S and the schematic structure of a nucleus with Q^2 along the horizontal axis and Bjorken x along the vertical axis. The increase of the gluon number at a fixed transverse size scale along the vertical axis eventually leads to the phenomenon of saturation.

the gluon distribution $xG(x, Q^2)$ at small x for a fixed Q^2 (see figure 28), growing approximately as a power of $x^{-0.3}$ can be understood within the BFKL framework. The rapid growth is moderated by the fact that gluons having transverse momenta less than a semi-hard saturation scale $Q_S(x)$ have a maximum occupation of $1/\alpha_s$. A parametric estimate for the onset of saturation can be made by considering the maximum number of partons that can be packed in a proton of size S_\perp .¹⁷³ The condition that the transverse area occupied by a parton ($\sim S_\perp/xG$) is on the order of the gluon fusion cross-section $\sigma \sim \alpha_s/Q^2$ defines a saturation scale $Q_S^2 \simeq \alpha_s xG(x, Q_S^2)/S_\perp$. The argument can be extended to nuclei; A nucleus with atomic number A has transverse size $S_\perp \sim A^{2/3}$ and its parton distribution scales approximately as $xG_{\text{nucleus}} \sim A \cdot xG$ resulting in

$$Q_S^2(x) \simeq \frac{\alpha_s A}{S_\perp} xG(x, Q_S^2) \sim \frac{A^{1/3}}{x^\lambda} \quad (21)$$

thereby enhancing saturation effects by a factor as large as $A^{1/3} \approx 6$ in nuclear targets such as lead ($A = 208$). The evolution of the saturation scale as a function of Q^2 and x is schematically shown in the *phase diagram* of high energy QCD in figure 28.

The Color Glass Condensate is an effective field theory description of the saturated gluons in the Regge-Gribov limit. More details can be found in the recent review article.¹⁷⁶ The degrees of freedom consist of strong color sources $\rho^a \sim 1/g$

of the nuclei and the resulting classical gauge fields. The strong color sources vary event-by-event and are governed by a gauge invariant probability distribution, W with expectation values of operators schematically written as

$$\langle \mathcal{O} \rangle \equiv \int [D\rho_P] [D\rho_T] W[\rho_P] W[\rho_T] \mathcal{O}[\rho_P, \rho_T]. \quad (22)$$

The requirement that physical observables be independent of the scale separating the sources from fields results in the JIMWLK renormalization group equation. There is no known analytic solution to the JIMWLK evolution equation and while numerical solutions are available,^{177,178} their use in phenomenology remains limited.¹⁷⁹ There exists a kinematic window in x where the nuclear wave-function can be derived in closed form. In the McLerran-Venugopalan model^{180–182} x must be large enough, $\alpha_s \log(1/x) \ll 1$, such that quantum corrections entering at leading logarithmic order can be neglected *and* x must be small enough, $x \ll A^{-1/3}$, such that the small- x partons couple coherently to the large- x sources. In this limit, the weight functional has the following Gaussian form

$$W[x, \rho] = \exp \left(- \int d^2 \mathbf{x}_\perp \left[\frac{\rho^\alpha(\mathbf{x}_\perp) \rho^\alpha(\mathbf{x}_\perp)}{2\mu_A^2} \right] \right), \quad (23)$$

where $\mu_A^2 = g^2 A / (2S_\perp)$ is the average color charge squared per unit area per unit color degree of freedom. While the MV model is a useful phenomenological tool at moderate values of $x \sim 10^{-2}$, at smaller x , as probed by the kinematics at the LHC, quantum corrections at leading logarithmic order in $1/x$ must be incorporated. The difficulties with the JIMWLK equation arise from its hierarchical structure (*e.g.* the evolution of the two-point function depends on the four-point function). This can be circumvented by working in the large N_c approximation (in addition to the already imposed large nucleus approximation). In this limit the expectation value of a four-point function can be recast as the product of correlators of two point functions and, at leading order in α_s , the JIMWLK equation is simplified to the LO Balitsky-Kovchegov^{183,184} (BK) equation

$$\frac{\partial T(\mathbf{r}, Y)}{\partial Y} = \int_{\mathbf{r}_1} \mathcal{K}(\mathbf{r}, \mathbf{r}_1) [T(\mathbf{r}_1, Y) + T(\mathbf{r}_2, Y) - T(\mathbf{r}, Y) - T(\mathbf{r}_1, Y) T(\mathbf{r}_2, Y)] \quad (24)$$

In the above expression $\mathbf{r}_2 \equiv \mathbf{r} - \mathbf{r}_1$ and $T(\mathbf{r}, Y)$ is the quark–anti-quark dipole scattering amplitude from a nucleus. In the context of the BK equation, the kernel \mathcal{K} amounts to resumming all terms of the form $(\alpha_s \ln(x_0/x))^n$ arising at any order in perturbation theory. It is well known that running coupling corrections qualitatively modify the small x evolution and analytic results determining the scale of the coupling that enters the evolution kernel are known.^{185,186} The form of these running coupling corrections amount to two pieces; a piece resembling a running coupling correction to the LO BK Kernel,¹⁸⁷ and a “subtraction term” that introduces new structures. In what follows we use the “Balitsky prescription” (equation (25)) for

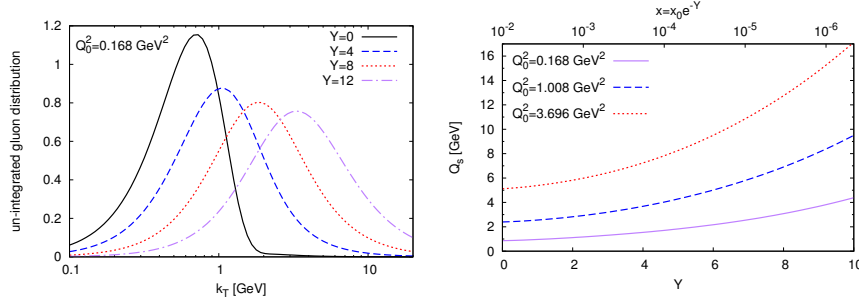


Fig. 29. Left: Un-integrated gluon distribution in the adjoint representation, plotted as $\alpha_s \phi / (S_\perp N_c)$, with initial condition ($Y = 0$) corresponding to a min. bias proton along with subsequent evolution by rcBK to ($Y = 4, 8, 12$). Right: The saturation scale defined as the location of the maximum of $k_\perp \phi(Y, k_\perp)$ as a function of $Y = \ln(x_0/x)$ for initial conditions $Q_0^2 = 0.168, 1.008, 3.696 \text{ GeV}^2$.

the evolution kernel,

$$\mathcal{K}_{\text{Bal.}}(\mathbf{r}, \mathbf{r}_1, \mathbf{r}_2) = \frac{\alpha_s(\mathbf{r}) N_c}{\pi} \left[\frac{\mathbf{r}^2}{\mathbf{r}_1^2 \mathbf{r}_2^2} + \frac{1}{\mathbf{r}_1^2} \left(\frac{\alpha_s(\mathbf{r}_1^2)}{\alpha_s(\mathbf{r}_2^2)} - 1 \right) + \frac{1}{\mathbf{r}_2^2} \left(\frac{\alpha_s(\mathbf{r}_2^2)}{\alpha_s(\mathbf{r}_1^2)} - 1 \right) \right], \quad (25)$$

as it was shown that the “subtraction term” is numerically less important¹⁸⁸ and will be ignored in this work. Numerical results¹⁸⁹ for the full NLO BK equation¹⁹⁰ have recently become available demonstrating a sensitive dependence on initial condition with results not necessarily positive definite calling for a better understanding of the NLO BK equation before it can be used for phenomenology. A recent analysis that resums double logarithms seems to improve the situation at NLO.¹⁹¹

Solution of the running coupling BK equations (rcBK) requires a suitable initial condition at large- x . This review will focus on the results using an MV model-like initial condition with anomalous dimension γ ,

$$T(\mathbf{r}, Y = 0) = 1 - \exp \left[- \left(\frac{r^2 Q_{s0}^2}{4} \right)^\gamma \ln \left(\frac{1}{r \Lambda_{QCD}} + e \right) \right]. \quad (26)$$

The value of γ and initial saturation scale (in the fundamental representation), Q_{s0}^2 have been constrained by global fits to available small- x ($x \leq 0.01$) lepton-proton scattering data.¹⁹² This work will use the parameter set h’ from¹⁹³ having parameters $\Lambda_{QCD} = 0.241 \text{ MeV}$, $\gamma = 1.119$, $Q_{s0}^2 = 0.168 \text{ GeV}^2$.

At large N_c the dipole scattering amplitude can be identified with the un-integrated gluon distribution in the adjoint representation¹⁹⁴

$$\Phi(Y, \mathbf{k}_\perp) = \frac{N_c \mathbf{k}_\perp^2}{4\alpha_s} \int d^2 \mathbf{r} e^{i \mathbf{k}_\perp \cdot \mathbf{r}} [1 - T(\mathbf{r}, Y)]^2. \quad (27)$$

For completeness we also point out that at large \mathbf{k}_\perp the Wilson lines can be expanded in powers of the sources yielding a relation between the average squared

color charge density and unintegrated gluon distribution

$$\Phi(Y, \mathbf{k}_\perp) = g^2 \pi (N_c^2 - 1) \frac{\mu^2(Y, \mathbf{k}_\perp)}{\mathbf{k}_\perp^2}. \quad (28)$$

The numerical solution of the rcBK equation is shown in the left plot of figure 29. The solid black curve is the initial condition defined in equation (26) and its evolution to $Y = 4, 8, 12$ is shown as the dashed, dotted, dash-dotted curves respectively. As we will argue at length below, the solitonic structure is crucial to our understanding of the ridge phenomenon. The non-monotonic behavior of the gluon distribution kinematically constrains gluons to be produced in similar directions. The transverse momentum dependence of the ridge will be controlled to a large extent by the maximum gluon occupation at the relevant values of x probed in the processes.

The right plot of figure 29 shows the location of the maximum of the quantity $k_\perp \Phi(k_\perp)$ as a function of Y or equivalently $x = x_0 e^{-Y}$. The quantity $k_\perp \Phi(k_\perp)$ represents the number of gluons at a given k_\perp and its maximum value can be identified with a saturation momentum though it should not be confused with the saturation scale that enters into the initial condition in equation (26). The latter is the *initial* saturation scale at $x = x_0 = 10^{-2}$ in the fundamental representation.

The solid purple curve in the right plot of figure 29 corresponds to the wavefunction shown in the plot on the left (*i.e.* having initial condition $Q_{s0}^2 = 0.168 \text{ GeV}^2$ which we will refer to as “minimum bias”). The rcBK equation has no impact parameter dependence and the fits to lepton-proton scattering data (from which the value of $Q_{s0}^2 = 0.168 \text{ GeV}^2$ is obtained) assumes that the impact parameter dependence factorizes from the dipole amplitude. Since the median impact parameter dominates inclusive scattering we will use this initial condition for proton configurations prototypical of minimum bias.

In order to mimic rare fock space configurations generated in high-multiplicity events the initial saturation scale will be adjusted to account for the increased multiplicity. The right plot of figure 29 also shows the evolution of the saturation momentum for configurations involved in high multiplicity events. The initial condition having $Q_{s0}^2 = 1.008 \text{ GeV}^2$ corresponding to $6\times$ the value of a min. bias proton will be argued to be the relevant scale need to describe high-multiplicity events in p-p collisions at the LHC. The initial condition with $Q_{s0}^2 = 3.696 \text{ GeV}^2$ ($22\times$ the min. bias proton) is used to describe a *hot-spot* configuration in the nucleus probed in central p-Pb events at the LHC. This large value is expected as it takes into account the additional $A^{1/3}$ enhancement from nuclear coherence.

4.3.1. Two-gluon production for $\mathbf{p}_\perp \gtrsim Q_S$: *Glasma Graphs*

In the presence of strong classical sources the naive power counting of Feynman diagrams can change drastically. We consider two mechanisms for the production of a pair of mid-rapidity hadrons. The first proceeds via the production of two

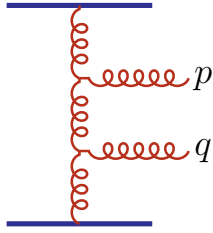
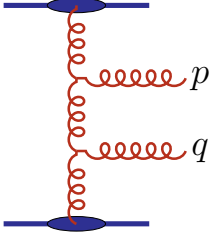
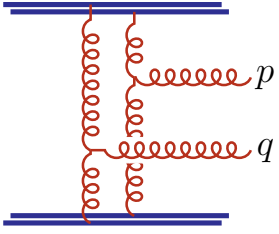
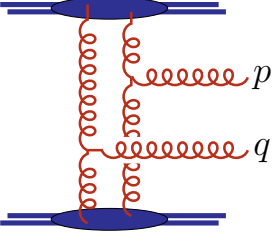
	Low color charge density (min. bias)	High color charge density (high multiplicity)
Jet Graph	 α_s^4	 α_s^0
Glasma Graph	 α_s^6	 α_s^{-2}

Table 1. Power counting for multiparticle production in QCD in the dilute (left column) and dense (right column) limit of color sources. The top row shows the diagram responsible for mini-jet production (hadrons produced primarily back-to-back in azimuthal angle). The bottom row shows the “glasma” diagram responsible for the near-side collimation that is long-range in rapidity. Each three-gluon vertex or coupling to a bare parton is proportional to g . Each gluon coupling to a *blob* contributes $1/g$.

gluons from a single t -channel gluon exchange as shown in the upper left amplitude in table 1. We refer to this diagram as the Jet Graph, since the gluon pairs that are produced in this channel are predominately back-to-back in azimuthal angle. We should stress that we are interested in mini-jets (*i.e.* soft dihadron correlations) and not jets in the usual sense studied in collinear factorization.

The second class of diagrams shown in the lower left of Fig. 1, has two gluons produced from two t -channel gluon exchanges. As drawn here the diagram appears disconnected and one might conclude does not contribute to an intrinsic two-particle correlation. This is not the case because the averaging over the color sources introduces non-trivial connections within the seemingly disconnected diagram.

In the dilute limit each vertex (both the three-gluon and the coupling to the valence parton) come with a single power of the strong coupling constant g . After squaring the jet amplitude the cross section scales as α_s^4 . The glasma diagram on the other hand has six such vertices and the cross-section is proportional to α_s^6 and is therefore suppressed by α_s^2 in the dilute limit of both projectile and target.

In the high energy limit the power counting changes dramatically. By high

energy limit we mean that $k_{\perp} \ll \sqrt{s}$ such that there is sufficient small- x evolution that the gluon densities are non-perturbatively large. The high-energy limit is also reached for large nuclei or rare collisions of hot-spot configurations of the projectile and/or target. The two tagged gluons now couple to the high occupancy $\sim 1/\alpha_s$ of larger- x sources. The effective coupling of a gluon to the valence region is now $1/g$ instead of g . This is depicted in the right diagrams of table 1 where each connection to a *blob* couples with $1/g$. In the dense-dense limit the Jet Graph goes as α_s^0 while the glasma graph scales as α_s^{-2} . For high multiplicity collisions one therefore expects the glasma graph as the main contributor to two-particle production.

These two classes of diagrams can also be treated in collinear factorization. The Glasma graph would refer to double parton scattering and is suppressed by $\Lambda_{\text{QCD}}^2/Q^2$ relative to a single parton scattering diagram^{195,196} (such as our Jet Graph). The high-energy limit of QCD therefore allows us to study novel QCD processes which would otherwise be largely inaccessible by experiment.

The motivation for the first study of two-particle correlations in the color glass condensate framework⁹³ was geared towards explaining the ridge in heavy-ion collisions. The basic idea is that the longitudinal chromo-electric and -magnetic fields created in the collision of two large nuclei radiate correlated particles approximately isotropically in the azimuthal separation of the pairs. The boost invariance of the classical field results in boost invariant particle production naturally explaining the long-range rapidity correlations. Collimation in azimuthal separation, $\Delta\phi$ is achieved by final-state effects such as strong radial flow due to hydrodynamic expansion.

The strength of the correlated two-particle distribution can be expressed as⁹³

$$\left\langle \frac{d^2N}{dy_p d^2\mathbf{p}_{\perp} dy_q d^2\mathbf{q}_{\perp}} \right\rangle_{\text{conn.}} = \kappa \frac{1}{Q_S^2 S_{\perp}} \left\langle \frac{dN}{dy_p d^2\mathbf{p}_{\perp}} \right\rangle \left\langle \frac{dN}{dy_q d^2\mathbf{q}_{\perp}} \right\rangle. \quad (29)$$

We should stress that the above is an intrinsic correlation expressed in terms of the single particle distribution^c and is essentially a consequence of dimensional analysis – the correlations are entirely classical in nature and there is only one scale, Q_S characterizing the strength of the fields. The factor $1/(S_{\perp} Q_S^2)$ has the physical interpretation of the transverse area of a flux-tube from where the particles are emitted divided by the transverse area of the system. The coefficient κ can be calculated but it is a constant of $\mathcal{O}(1)$ and the strength of the resulting correlation fares well with the experiment in a blast-wave model.¹⁹⁷ The subsequent discovery of the double-ridge (a symmetric collimation on *both* the near and away-side) which was found after careful subtraction of the recoiling jet leaves a gap in this picture.

It was later realized that the glasma graphs contain an intrinsic dependence on

^cIn general, the double inclusive distribution can be written as

$$\left\langle \frac{d^2N}{dy_p d^2\mathbf{p}_{\perp} dy_q d^2\mathbf{q}_{\perp}} \right\rangle = \left\langle \frac{dN}{dy_p d^2\mathbf{p}_{\perp}} \right\rangle \left\langle \frac{dN}{dy_q d^2\mathbf{q}_{\perp}} \right\rangle + \left\langle \frac{d^2N}{dy_p d^2\mathbf{p}_{\perp} dy_q d^2\mathbf{q}_{\perp}} \right\rangle_{\text{conn.}} \quad (30)$$

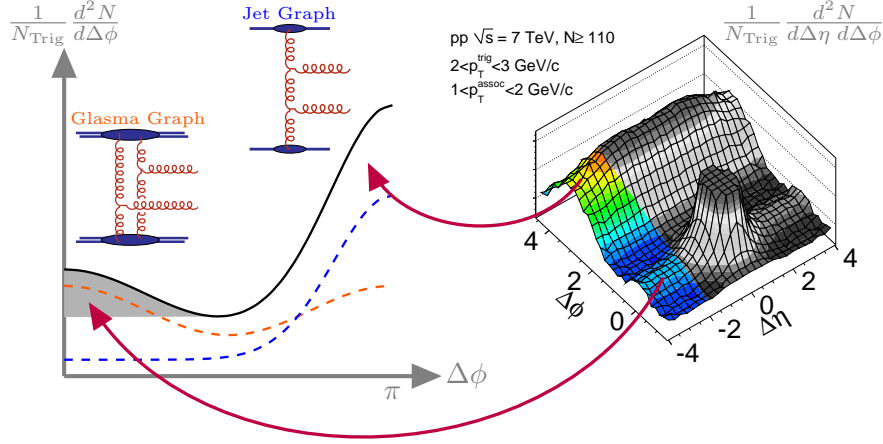


Fig. 30. Anatomy of a proton-proton collision. The away-side peak, associated with mini-jet production can be understood from the jet-graph (two gluons produced from a single ladder) as shown in the right diagram along with its schematic contribution to the per-trigger-yield plotted in blue. The Glasma graph contribution (left diagram) is shown schematically by the orange curve. The shaded gray region (extracted experimentally by the ZYAM procedure) is referred to as the associated yield

the azimuthal separation irrespective of the presence of an additional collimation mechanism¹⁹⁸ which is not apparent in equation (29). After the observation of a ridge in high-multiplicity proton collisions a blast-wave analysis showed that the near-side ridge in p-p could *not* be described by combination of isotropic production from glasma flux tubes with subsequent transverse flow.¹⁹⁹ Instead, the systematics of the p-p ridge were consistent with the intrinsic azimuthal dependence from glasma graphs leaving little room for any additional transverse expansion.

We therefore have the following picture of the dihadron correlations in proton-proton collisions (summarized graphically in Fig.30). The Jet Graph generates particles predominately back-to-back (*i.e.* at relative azimuthal angle of π) and when expressed as a per-trigger-yield^d is approximately independent of multiplicity, an observation consistent with the experimental data.

Due to a novel interference phenomenon generated from the intrinsic correlations in the nucleus (the precise form of which will be discussed in the subsequent sections) the glasma graph has enhanced production on angular separations of $\Delta\phi = 0$ and $\Delta\phi = \pi$. The collimation at $\Delta\phi = 0$ is responsible for the near-side ridge while

^dThe per-trigger-yield is the double-inclusive distribution $\langle d^2N \rangle$ divided by one power of the single inclusive distribution $\langle dN \rangle$. Since the jet and single-gluon graphs proceed via a single t -channel exchange they have the same number of connections to the larger- x sources and therefore much of the centrality dependence cancels in the ratio.

that at $\Delta\phi = \pi$ explains the double-ridge (after appropriate jet subtraction).

The glasma graph has a much stronger centrality dependence than the jet graph. In the dilute-dilute limit the per-trigger yield ^e of the glasma graph scales with coupling as α_s^3 while in the dense-dense limit it goes as α_s^{-1} . This large enhancement is expected for high multiplicity events at moderate $\mathbf{p}_\perp \sim Q_S$.

With this basic picture in mind we now go on to discuss two-gluon production in the color glass-condensate framework. The next two sections focus on the perturbative $\mathbf{p}_\perp \gg Q_S$ limit of di-jet production and glasma graphs respectively and explore the mechanism behind the intrinsic azimuthal correlations. We will then give an overview of the relevant phenomenology of this framework and discuss some open issues.

Mini-jet production In this section we explore in more detail our understanding of di-jet or mini-jet production. The away-side (or recoiling jet) is pervasive in all dihadron analyses and serves as an important baseline.

Computing the di-jet amplitude in the Color-Glass-Condensate framework is a formidable task. The diagram shown in the upper right of table 1 involves calculating the gluon propagator in the full nonlinear classical background field. In the dilute-dense limit this was looked at in^{200–203} and the resulting expression could not be written in a k_T -factorized form as the end result involved correlators of four Wilson lines. This quadrupole operator obeys its own evolution equation and it cannot be factorized into a simple product of dipoles. We point out, however, that its nonlinear Gaussian approximation²⁰⁴ in terms of the dipole operator agrees numerically very well with the full result in JIMWLK evolution.¹⁷⁸

In contrast, di-jet production has been extensively studied in collinear factorization and at leading order the partons are produced strictly back-to-back^f. This is due to the fact that the internal momentum distribution of the partons in the hadrons is neglected and conservation of momentum requires the produced partons to have equal transverse momentum squared and opposite directions, *i.e.*, $\sigma \sim \delta(\mathbf{p}_\perp^2 - \mathbf{q}_\perp^2)\delta(|\phi_p - \phi_q| - \pi)$. Any internal motion, for example due to Fermi motion or soft emissions, will lead to a decorrelation of the jets.

The soft radiation emitted between the produced gluons and their respective hadrons in addition to the emission of rapidity ordered gluons between the two

^eThe single inclusive spectra scale as α_s^3 , α_s and α_s^{-1} in the dilute-dilute, dilute-dense, and dense-dense limits respectively.

^fThe collinear factorized form for di-jet production can be obtained from the k_\perp -factorized form by substitution of the unintegrated gluon distribution with the appropriate parton distributions, $\Phi(\mathbf{k}_\perp) = xg(x) 4\pi^4\delta^{(2)}(\mathbf{k}_\perp)$. From equation 33 we obtain

$$\frac{d^2 N}{dy_p d^2 \mathbf{p}_\perp dy_q d^2 \mathbf{q}_\perp} = x_p g(x_p) x_q g(x_q) \frac{4\alpha_s^2 N_c^2}{(N_c^2 - 1)} \frac{\delta^{(2)}(\mathbf{p}_\perp + \mathbf{q}_\perp)}{\mathbf{p}_\perp^2 \mathbf{q}_\perp^2} \quad (31)$$

agreeing with equation (60) of²⁰⁵ when the large- y matrix element given in equation (54) is used.

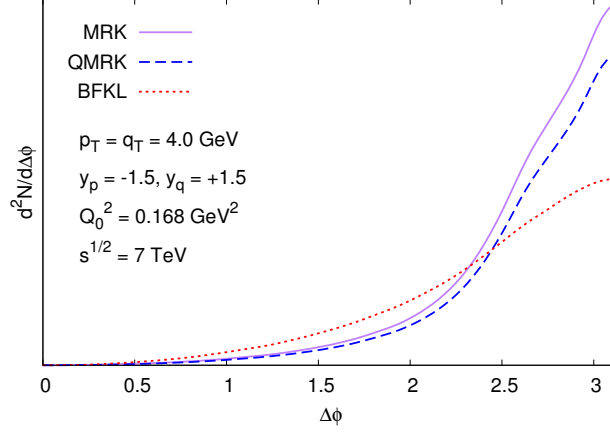


Fig. 31. Two-gluon production versus relative azimuthal separation for min. bias p+p collisions (details are labelled in the figure). The three curves represent three approximations; Dashed blue: Eikonal approximation (parametrically small angle scattering of incident particles) to the 2 – 4 matrix element without radiation between the tagged gluons ($\alpha_s \Delta y \rightarrow 0$), Solid purple: Leading term in $\Delta y \rightarrow \infty$ of the QMRK result, Dotted orange; Includes the full BFKL Green's function taking into account the emission of rapidly ordered gluons between the tagged final-state partons.

tagged partons is encoded within the following k_T factorized di-jet cross-section

$$\frac{d^2 N}{d^2 \mathbf{p}_\perp d^2 \mathbf{q}_\perp dy_p dy_q} = \frac{\alpha_s^2 N_c^2}{4\pi^8 (N_c^2 - 1)} \frac{S_\perp}{\mathbf{p}_\perp^2 \mathbf{q}_\perp^2} \quad (32)$$

$$\times \int_{\mathbf{k}_{0\perp}, \mathbf{k}_{3\perp}} \Phi_P(\mathbf{k}_{0\perp}) \Phi_T(\mathbf{k}_{3\perp}) \mathcal{G}(\mathbf{k}_{0\perp} - \mathbf{p}_\perp, \mathbf{k}_{3\perp} + \mathbf{q}_\perp, \Delta y_{pq}).$$

In the context of BFKL resummation (where the above is rigorously defined) the quantities Φ are the BFKL evolved impact factors and are known to next-to-leading order.²⁰⁶ In this work we will apply a *hybrid* formalism that identifies the impact factor with the unintegrated gluon distributions introduced earlier. We employ in this work the LO BFKL Green's function, the explicit form of which can be found in²⁰⁵ for example. Though its NLL form is known²⁰⁶ the corrections introduced to the observables considered here are small enough to be neglected.

The BFKL radiation can be *switched off* by taking the $\alpha_s \Delta y$ limit of the above Green's function and the resulting di-jet cross section becomes

$$\frac{d^2 N}{dy_p d^2 \mathbf{p}_\perp dy_q d^2 \mathbf{q}_\perp} = \frac{\alpha_s^2 N_c^2}{8\pi^8 (N_c^2 - 1)} \frac{S_\perp}{\mathbf{p}_\perp^2 \mathbf{q}_\perp^2} \int d^2 \mathbf{k}_\perp \Phi(\mathbf{k}_\perp) \Phi(\mathbf{k}_\perp + \mathbf{p}_\perp + \mathbf{q}_\perp) \quad (33)$$

The above expression is valid in the multi-Regge kinematics (MRK) corresponding to the leading $\Delta y \rightarrow \infty$ limit of the $2 \rightarrow 4$ amplitude. Using the $2 \rightarrow 4$ matrix element in the eikonal approximation results in the quasi-multi-Regge kinematics (QMRK) whose precise form can be found in.²⁰⁷

Figure 31 demonstrates the results of the above discussion and shows the relative importance of including rapidity ordered gluon emissions even for moderate $\alpha_s \Delta y$ as encoded in the BFKL formalism. Neglecting these emission would spoil the agreement with the experimentally measured away-side mini-jet. The details of the full calculations will be discussed further on, but The agreement between the BFKL evolution and the experimental data can be seen the agreement of the away-side yield in figure 33 for p-p collisions. Another example is the agreement between the blue curve in the right plot of figure 34 that shows the mini-jet with BFKL evolution in peripheral p-Pb and the corresponding ATLAS measurement of the same. The mini-jet itself contains interesting QCD dynamics and may be a useful probe of Pomeron exchange and BFKL evolution²⁰⁸ complementing studies that look for the growth in di-jet cross section as proposed in.²⁰⁹

Glasma Graphs We now review the mechanism behind the intrinsic collimation that was predicted^{198,210} to exist in systems lacking hydrodynamic flow or final state rescattering. We will provide an overview of the *glasma graphs* that are responsible for this intrinsic azimuthal correlation and argue that the resulting signal is a quantum interference effect sensitive to correlations present in the nuclear wavefunction before the collision occurs.

In order to set the stage and develop some notation we will begin with an overview of the perturbative $\mathbf{p}_\perp \gg Q_S$ calculation of single gluon production and its resulting k_\perp -factorized expression. The starting point is the probability to produce a gluon having rapidity y and transverse momentum \mathbf{k}_\perp ,

$$\frac{dN}{dy d^2\mathbf{k}_\perp} = \frac{1}{2(2\pi)^3} \sum_{a,\lambda} \langle |M_\lambda^a(\mathbf{k})|^2 \rangle. \quad (34)$$

The classical contribution to the amplitude for the production of a single gluon with four-momentum k is $M_\lambda(\mathbf{k}) = \epsilon_\mu^\lambda(\mathbf{k}) k^2 A^\mu(\mathbf{k})$ with ϵ_μ^λ representing the gluon polarization vector having polarization states λ . The above should be evaluated in the on-shell $k^2 \rightarrow 0$ limit. The expectation value $\langle \dots \rangle$ represents an averaging over the color configurations of the two nuclei.

At large transverse momentum the gauge fields can be expressed explicitly in terms of color charge densities^{121,130} of the projectile and target nuclei, ρ_P and ρ_T ,

$$p^2 A^{\mu a}(p) = -i f^{abc} g^3 \int \frac{d^2\mathbf{k}_\perp}{(2\pi)^2} L^\mu(\mathbf{p}_\perp, \mathbf{k}_\perp) \frac{\rho_P^b(\mathbf{k}_\perp) \rho_T^c(\mathbf{p}_\perp - \mathbf{k}_\perp)}{\mathbf{k}_\perp^2 (\mathbf{p}_\perp - \mathbf{k}_\perp)^2}. \quad (35)$$

$L^\mu(\mathbf{p}_\perp, \mathbf{k}_\perp)$ is the effective Lipatov gluon emission vertex.¹⁷² The resulting expectation value in equation (34) is a product of two-point correlators over the color charge densities of the target and projectile. In the non-local MV model the momentum space correlator is

$$\langle \rho^a(\mathbf{k}_{1\perp}) \rho^{*b}(\mathbf{k}_{2\perp}) \rangle = (2\pi)^2 \delta^{ab} \mu^2(\mathbf{k}_{1\perp}) \delta^{(2)}(\mathbf{k}_{1\perp} - \mathbf{k}_{2\perp}). \quad (36)$$

We should stress that in order to accommodate the small- x evolution one needs to generalize the local MV model of equation (23) to include a nonlocal version such

that $\mu^2 \rightarrow \mu^2(\mathbf{x}_\perp - \mathbf{y}_\perp)$ and consequently in momentum-space a function of the transverse momentum (*i.e.* $\mu^2 \rightarrow \mu^2(|\mathbf{k}_\perp|)$). Further discussion of this subtlety can be found in.¹⁹⁴ Combing equations (28), (34), (35), (36) the following k_T -factorized form for the single inclusive gluon production is obtained

$$\frac{dN}{dy_p d^2\mathbf{p}_\perp} = \frac{\alpha_s N_c}{\pi^4 (N_c^2 - 1)} \frac{S_\perp}{\mathbf{p}_\perp^2} \int \frac{d^2\mathbf{k}_\perp}{(2\pi)^2} \Phi_P(\mathbf{k}_\perp) \Phi_T(\mathbf{p}_\perp - \mathbf{k}_\perp). \quad (37)$$

We should point out that the above factorized form is obtained in a different limit than the usual- k_T factorization derived from the scattering of a dilute projectile off a quasi-classical target as examined in²¹¹ for example. Equation 37 has been able to successfully describe a wealth of single-inclusive data from both p-p and d-Au collisions.^{212–215}

We now consider the production of a pair of gluons with transverse momenta \mathbf{p}_\perp and \mathbf{q}_\perp and longitudinal rapidity y_p and y_q within the same framework. The double-inclusive gluon distribution is

$$\frac{d^2N}{dy_p d^2\mathbf{p}_\perp dy_q d^2\mathbf{q}_\perp} = \frac{1}{4(2\pi)^6} \sum_{a,b,\lambda,\sigma} \langle |M_{\lambda\sigma}^{ab}(\mathbf{p}, \mathbf{q})|^2 \rangle. \quad (38)$$

The *classical* contribution to the two-gluon matrix element is $M_{\lambda\sigma}^{ab}(\mathbf{p}, \mathbf{q}) = \epsilon_\mu^\lambda(\mathbf{p}) \epsilon_\nu^\sigma(\mathbf{q}) p^2 A^{\mu,a}(\mathbf{p}) q^2 A^{\nu,b}(\mathbf{q})$ and these gauge fields can be expanded in terms of the color charge densities when $\mathbf{p}_\perp, \mathbf{q}_\perp \gg Q_S$ as done in equation (35). Putting all the pieces together we obtain the following schematic form of the inclusive two-gluon distribution

$$\begin{aligned} \frac{d^2N}{dy_p d^2\mathbf{p}_\perp dy_q d^2\mathbf{q}_\perp} &\sim \int_{\substack{\mathbf{k}_{1\perp}, \mathbf{k}_{2\perp}, \\ \mathbf{k}_{3\perp}, \mathbf{k}_{4\perp}}} \mathcal{T}(\mathbf{p}_\perp, \mathbf{q}_\perp, \mathbf{k}_{i\perp}) \langle \rho_P(\mathbf{k}_{1\perp}) \rho_P^*(\mathbf{k}_{3\perp}) \rho_P(\mathbf{k}_{2\perp}) \rho_P^*(\mathbf{k}_{4\perp}) \rangle \\ &\quad \times \langle \rho_T(\mathbf{p}_\perp - \mathbf{k}_{1\perp}) \rho_T^*(\mathbf{p}_\perp - \mathbf{k}_{3\perp}) \rho_T(\mathbf{q}_\perp - \mathbf{k}_{2\perp}) \rho_T^*(\mathbf{q}_\perp - \mathbf{k}_{4\perp}) \rangle \end{aligned}$$

where color indices have been suppressed and a shorthand notation, \mathcal{T} , has been used for the product of multiple Lipatov vertices, the detailed form of which will not be needed for the qualitative discussion to follow.

The basis of the *glasma graph* framework is the factorization of the four-point functions into products of two point functions using the Gaussian form of the color charge distribution such as the local MV model in equation (23) or the non-local MV model in equation (36) (used for the remainder of this section) that accommodates small- x evolution. The resulting factorization results in a total of nine diagrams, each carrying a unique dependence on the azimuthal separation of the two produced gluons which we will discuss in turn.

An important piece of the above formalism, which remains to be discussed, is the rapidity dependence of the above correlation. At leading order in α_s (*i.e.* working within the *local* MV model) the particle production is boost-invariant and therefore independent of the rapidity separation of the pairs and their respective separation from the leading hadrons. Quantum corrections modify this picture and lead to the breaking of boost invariance. The difficulty in the proper treatment of

the above problem stems from the fact that not only must quantum evolution be included between the measured gluons and the leading nuclei but also *between* the two measured gluons. A dense-dense factorization formalism resumming leading logarithms in $1/x$ corrections for inclusive observables developed in^{216–218} was used to compute the rapidity dependence of gluon-pair production in.¹⁰⁰ However, this factorization may break down when $\alpha_s \Delta y \gg 1$.²¹⁹ Regardless, the framework used here serves as a useful starting point for addressing the role of long-range rapidity correlations in the dense-dense limit.

As noted above the glasma graphs are obtained by forming all possible contractions over the color sources. One of the nine resulting graphs corresponds to the single-inclusive spectra squared. While it is leading in N_c it has no dependence in azimuthal separation *within the approximations used here*. However, event-by-event fluctuations or an impact parameter profile of the nuclei would indeed generate azimuthal correlations within this framework (as seen for example in²²⁰). We now focus on the remaining eight diagrams and the azimuthal correlations they generate without introducing a global geometry.

Let us give as an example the expression from one such diagram responsible for the near-side ridge

$$\frac{d^2 N_{\text{Fig. 32}}}{d^2 \mathbf{p}_\perp d^2 \mathbf{q}_\perp dy_p dy_q} = \frac{\alpha_s^2 N_c^2}{4\pi^{10} \zeta (N_c^2 - 1)^3} \frac{S_\perp}{\mathbf{p}_\perp^2 \mathbf{q}_\perp^2} \int_{\mathbf{k}_\perp} \Phi_p^2(\mathbf{k}_\perp) \Phi_T(\mathbf{p}_\perp - \mathbf{k}_\perp) \Phi_T(\mathbf{q}_\perp - \mathbf{k}_\perp),$$

where the unintegrated gluon distributions are evaluated at (small) x values on the order $x \sim p_T / \sqrt{s} e^{\pm y_p}$ – the precise prescription is given in.^{221,222} The feynman diagram is shown in figure 32. There is a single loop momentum in this diagram \mathbf{k}_\perp that is integrated over. The transverse momentum flowing out of the nuclear projectile and target (represented here by the blobs) is of the order of their respective saturation momentum. In this case we therefore must have $|\mathbf{p}_\perp - \mathbf{k}_\perp| \sim Q_S$ and $|\mathbf{q}_\perp - \mathbf{k}_\perp| \sim Q_S$. Furthermore the magnitude of the loop momentum must also be near the saturation scale $|\mathbf{k}_\perp| \sim Q_S$. This leads to the conditions that $q_\perp^2 - 2q_\perp Q_S \cos \phi_{kq} = 0$ and $p_\perp^2 + p_T Q_S \cos \phi_{kp} = 0$. This pair of equations constrains the produced gluons such that 1) $\phi_p = \phi_q$, collimation on the near side. 2) $p_\perp \sim q_\perp$, maximum correlation for similar transverse momentum and 3) $p_\perp \sim Q_S$ maximum correlation near a semi-hard scale. All three of these features are born out by the full numerical calculation and consistent with the trends seen in the data.

The full glasma graph calculation includes contributions from all eight graphs – the detailed expression can be found in.²²² All eight diagrams provide a near- and/or away-side collimation and are necessary for a quantitative description of the data. Two diagrams of note are those having delta function correlations, $d^2 N / d\Delta\phi \sim \delta^{(2)}(\mathbf{p}_\perp \pm \mathbf{q}_\perp)$, which was interpreted as HBT-like correlations in.²²³ In the dilute-dense limit (by dilute we mean $\phi_p(\mathbf{k}_\perp) \sim \delta^{(2)}(\mathbf{k}_\perp)$) these two graphs are the only glasma graphs that remain and are therefore crucial for our understanding of highly asymmetric collisions. The delta functions will be broadened by hadronization. For

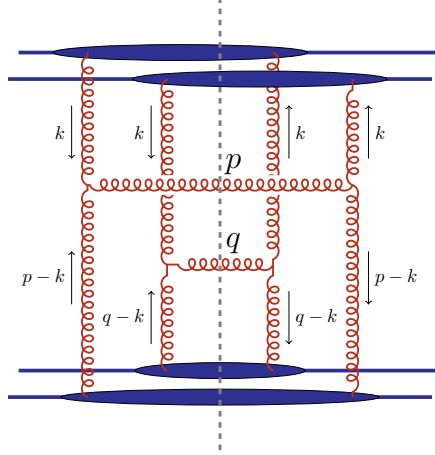


Fig. 32. Momentum flow demonstrating the generation of the near-side collimation. The intrinsic parton momentum of either hadron is on the order Q_S and therefore $|\mathbf{p}_\perp - \mathbf{k}_\perp| \sim |\mathbf{q}_\perp - \mathbf{k}_\perp| \sim Q_S$ where \mathbf{k}_\perp is a loop momentum constrained such that $|\mathbf{k}_\perp| \sim Q_S$.

practical considerations the delta function is replaced by a Gaussian, the precise form of which can be found in,²²⁴ originally fit to the p-p dihadron correlations before the availability of any data on p-Pb. The good agreement with the subsequent p-Pb data shows the robustness of this modeling of non-perturbative hadronization dynamics. We should stress that the associated yield (the integral over ϕ_{pq} on the near side) is insensitive to the functional form of the smearing function.

In order to convert the two-gluon correlations presented above into the hadronic observables, an appropriate hadronization procedure must be used. In what follows we show results using the NLO KKP parameterization²²⁵ of fragmentation functions for gluon to charged hadrons. It has recently been found that the NLO KKP results are troublesome at LHC energies²²⁶ and suggested that the gluon-to-hadron fragmentation functions were a probable source of this problem. Extraction of new fragmentation functions by fits to the more recently available single inclusive hadronic data would be highly valuable.

Figure 33 shows a comparison of the di-hadron correlation compared to the results for high multiplicity p-p collisions. The full numerical calculations of all eight glasma graphs along with the away-side mini-jet contribution with BFKL evolution corroborate the qualitative picture shown in figure 30. The centrality dependence is controlled by an appropriate choice of initial saturation scale Q_{s0}^2 that fixes the initial condition in the rcBK evolution equation. Fits to deep-inelastic scattering constrain $Q_{s0}^2 = 0.168 \text{ GeV}^2$ and we take this value as representative of min. bias p-p collisions. For convenience, we work with integer multiples of this saturation scale. For example, central p-p ($N_{\text{trk}}^{\text{offline}} \geq 110$) corresponds to 5-6 times this min. bias value.

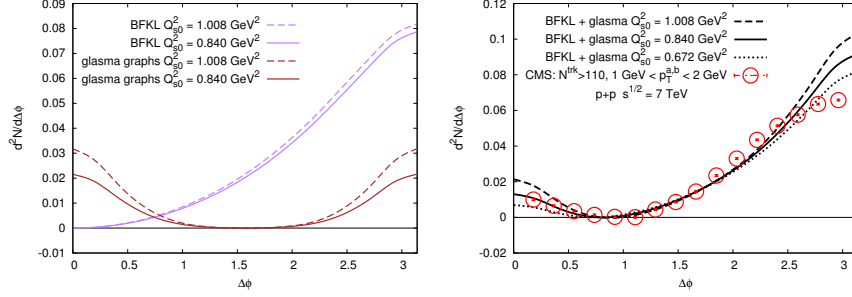


Fig. 33. Long range ($2 \leq \Delta\eta \leq 4$) per-trigger yield of charged hadrons as a function of $\Delta\phi$ for p-p collisions at $\sqrt{s} = 7$ TeV. Data points are from the CMS collaboration. The curves show the results for $Q_0^2(x = 10^{-2}) = 0.840$ GeV² and $Q_0^2(x = 10^{-2}) = 1.008$ GeV².

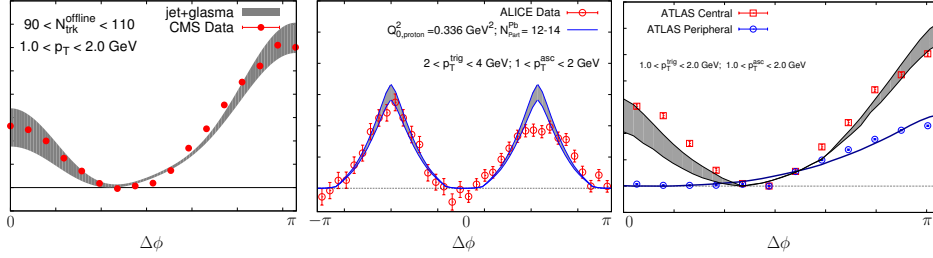


Fig. 34. Representative sample of p-Pb data from the CMS, ALICE and ATLAS collaborations of the per-trigger yield along with calculations within the *glasma graph* framework.

The overall strength of the glasma graph contribution is controlled by α_s which is evaluated at one-loop running at the relevant momentum scale of the process. In addition, a correction from non-perturbative dynamics (for example multiple scattering) is taken into account through the multiplicative pre-factor $1/\zeta$ that enhances the glasma graph contribution relative to the jet contribution.

The parameter ζ is particularly sensitive to the multiplicity distribution (see figure 35) and independent fits corroborate the value of $\zeta = 1/6$ used in the glasma graph ridge analysis. Lattice calculations^{116,227} find that this constant can be small, $\zeta \sim 0.2 - 1$, lending support that non-perturbative corrections due to multiple-scattering enhance the signal.

A comprehensive comparison of the glasma graph framework with all the available p-p, p-A and d-A data was presented in²²² and will not be reproduced here. Instead in figure 34 we show a representative set of p-Pb data from the CMS, ALICE and ATLAS collaborations along with the corresponding glasma graph calculations.

In summary, the glasma graph framework is able to account for many features of the data on a qualitative and quantitative level. These include 1) the long range

nature of the correlations, 2) the nearly symmetric near- and away-side ridge (the double ridge), 3) the strength of the correlation as a function of transverse momentum, in particular the maximum correlation for $p_\perp \sim q_\perp \sim Q_s$, 4) the non-trivial centrality dependence of both p-p and p-Pb collisions.

Since the time of the above analysis more precise data on the experimental side have uncovered two shortcomings in the glasma graph description. The first is the presence of a large and positive v_3 in central p-Pb collisions. The glasma graphs only contribute to the even harmonics and the peripheral jet diagram gives a negative v_3 . Whether modifications to the jet can accommodate a positive v_3 has yet to be fully explored. Further, the interference diagram between the jet and glasma graph also appears to vanish.²²⁸ Recent calculations within classical Yang-Mills provide one source of positive v_3 (see section 4.4) but this has yet to confront the data.

A final shortcoming of the glasma graph description (at least within the framework used here) is the negative $c_2\{4\}$ measured by CMS. The glasma graph and jet graph both give a positive contribution to $c_2\{4\}$. The empirical observation that $\sqrt[4]{-c_2\{4\}} \sim \sqrt[6]{c_2\{6\}} \sim \sqrt[8]{-c_2\{8\}}$ suggests that the correlation is driven by correlations among the disconnected diagrams at the single-inclusive level. We should stress that the multiple particle correlations are dominated by soft momentum $\mathbf{p}_\perp \lesssim Q_s$ where the glasma graph framework no longer applies. It would be very interesting to see if and where $c_2\{4\}$ changes sign as the minimum p_T used in the analysis is increased and when a rapidity gap between the particles is introduced in order to suppress jet-like correlations.

Multi-gluon production in the CGC The framework laid out for two-gluon production in the previous section has been extended to three gluons²²⁹ and generalized to n -gluons.²³⁰

The results can be represented diagrammatically as *glasma graphs* in a similar fashion as above and the subset of these diagrams that contribute for $\mathbf{p}_\perp \gg Q_s$ has been identified and the n -gluon distribution is

$$\left\langle \frac{d^n N}{dy_1 d^2 \mathbf{k}_{1\perp} \cdots dy_n d^2 \mathbf{k}_{n\perp}} \right\rangle = (n-1)! \frac{\zeta(N_c^2 - 1)}{2\pi} \frac{Q_s^2 S_\perp}{\mathbf{k}_{1\perp}^4 \cdots \mathbf{k}_{n\perp}^4} \left(\frac{N_c (g^2 \mu)^4}{2\pi^3 g^2 \zeta Q_s^2} \right)^n, \quad (39)$$

where the sensitivity to the infrared dynamics is encoded in the constant ζ introduced earlier. The factorial cumulants $\langle d^n N \rangle$ are those of a negative binomial

$$P_n^{\text{NB}}(\bar{n}, k) = \frac{\Gamma(k+n)}{\Gamma(k)\Gamma(n+1)} \frac{\bar{n}^n k^k}{(\bar{n}+k)^{n+k}} \quad (40)$$

where \bar{n} is the average multiplicity and $k = \zeta(N_c^2 - 1)Q_s^2 S_\perp / (2\pi)$ is proportional to the number of flux tubes. For $k = 1$ the negative binomial is a Bose-Einstein distribution and for $k \rightarrow \infty$ the distribution is Poissonian. The left plot in figure 35 shows the resulting multiplicity distribution in p-p collisions in the IP-Sat model¹²⁰ with the one free parameter $\zeta = 0.155$ fit to data at 0.9 TeV and then exhibited for other energies.

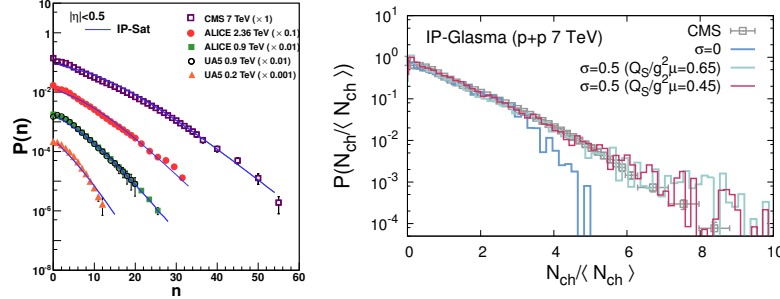


Fig. 35. Multiplicity distribution within k_{\perp} -factorization in the IP-Sat model²¹² (left) and from classical Yang-Mills with intrinsic fluctuations of the proton saturation scale²³¹ (right).

The right plot in figure 35 shows the recent results of²³¹ for the multiplicity distribution in p-p from classical Yang-Mills simulations. In this case there is no free parameter ζ and the infrared behavior is instead determined by the resulting non-linear dynamics of the gluon fields. In this framework there are multiple sources of fluctuation. First there is a geometric dependence from the saturation scale in the IP-Sat model which sets the initial field configurations. Second, sub-nucleonic fluctuations from the sampling of different configurations of color charges according to the MV model give rise to the negative binomial distribution of gluon number fluctuations for fixed geometry.

However, convolution of these two sources alone are not sufficient to account for the broad width of the multiplicity distribution. In addition there must be intrinsic fluctuations of Q_S in the proton. Modeling the distribution of saturation scales of the proton as a Gaussian distribution provides a good description of the data. The key point for this discussion is that high multiplicity events easily accommodate saturation scales 5–6 times the min. bias values as used to explain the ridge data.

4.3.2. Classical Yang-Mills dynamics

The calculations within the *glasma graph* framework presented in the previous section are strictly valid for $p_T \gtrsim Q_S$ and are infrared divergent if extended to lower transverse momentum. The divergences are regulated by the non-perturbative dynamics of the gluon fields at scales of order Q_S . These dynamics can be captured by solving the classical Yang-Mills equations numerically in the forward light-cone and are valid at any transverse momentum – only limited in the ultraviolet by the inverse lattice spacing and in the infrared by the inverse nuclear size. The perturbative, high p_T , limit of the classical Yang-Mills simulations can be expressed in terms of similar *glasma graphs* if a Gaussian distribution in the sources is used. Corrections due to small- x evolution in numerical simulations of quasi-classical gluon production have been done²³² but in the following section on classical Yang-Mills dynamics a local Gaussian distribution of sources is used (which does not accom-

moderate small- x evolution).

Empirically, the near-side ridge persists to momenta well below the saturation scale and it is therefore imperative to investigate whether the Glasma flux-tube picture holds in this kinematic region. It is also useful to establish the size of the corrections due to multiple scattering at larger transverse momentum. In the remainder of this section we will review the numerical results²³³ of the classical Yang-Mills simulations. We will discuss how the classical Yang-Mills results complement the *glasma graph* description and also provide possible resolutions to some of the discrepancies with data alluded to in the previous section on glasma graph phenomenology.

In the CGC picture, the dynamics of a high energy collision is described by the solution of the classical Yang-Mills equations

$$[D_\mu, F^{\mu\nu}] = J^\nu, \quad (41)$$

in the forward light-cone of the collision. In the above expression J^ν is an eikonal color current generated by a color neutral distribution of classical charges moving along the light-cone,

$$J^\nu = \delta^{\nu+} \rho_p(x^-, \mathbf{x}_\perp) + \delta^{\nu-} \rho_T(x^+, \mathbf{x}_\perp). \quad (42)$$

The sources are distributed according to a Gaussian distribution having variance

$$g^2 \langle \rho^a(\mathbf{x}_\perp) \rho^b(\mathbf{y}_\perp) \rangle = S_{p/Pb}(\mathbf{b}_\perp) \delta^{ab} \delta^{(2)}(\mathbf{x}_\perp - \mathbf{y}_\perp). \quad (43)$$

The function $S_{p/Pb}(\mathbf{b}_\perp)$ encodes information on the spatial structure of color charge distributions of the projectile and target. The results shown here use a *constituent quark proton model* whereby the color charge density is concentrated around the transverse positions of three constituent quarks whose positions fluctuate event to event. The use of a *spherical proton* has a negligible effect on the results.²³³ The result is even less sensitive to the impact parameter dependence of the color charge in the nucleus which is sampled from a Wood-Saxon distribution.

Starting from field configurations derived from the color charges in a given event the classical equations of motion are solved and the gluon distribution extracted at a given proper-time by measuring equal-time correlation functions of the gauge fields. Using either two-particle correlations or the event plane method $v_2(p_T)$ and $v_3(p_T)$ can be extracted from the gluon spectrum as show in the left and right plot of figure 36. We now discuss the implications of these results.

It is striking that a sizable $v_2(p_T)$ is present at the initial time $\tau = 0^+$ as it therefore cannot be attributed to a collective expansion of the system. This is in contrast to a hydrodynamic interpretation where the elliptic flow is initially zero and gradually develops over the lifetime of the collision. Further evolution of the Yang-Mills simulation finds only a modest decrease in the v_2 at later times indicating that the glasma flux-tube picture is robust against gluon re-scattering (a similar conclusion was reached by earlier lattice simulations²²⁷ as well).

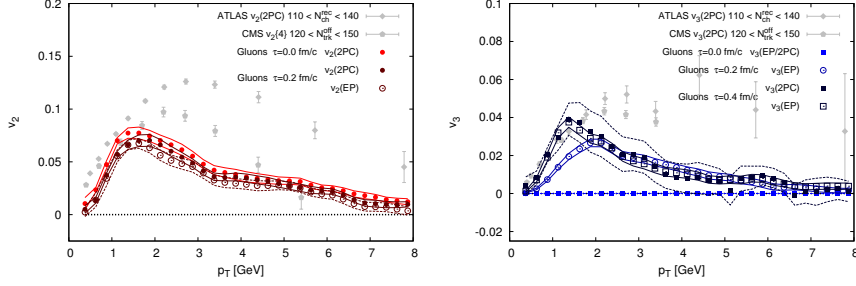


Fig. 36. (Color online) Gluon $v_2(p_T)$ (left) and $v_3(p_T)$ (right) at times $\tau = 0, 0.2, 0.4$ fm/c in p-Pb collisions at impact parameter $\mathbf{b}_\perp = 0$ in the constituent quark proton model. Open and closed symbols correspond to results obtained using the event plane method and two particle correlations, respectively. Error bands include statistical errors only. Experimental results by the ATLAS³⁷ and CMS collaboration³⁵ for inclusive hadrons are also shown as a guideline for comparison.

The observation that v_2 as extracted from the event-plane method and two particle correlations are similar within errors suggests that the dominant origin of the v_2 is the breaking of rotational symmetry of the single particle spectrum on a per-event basis. To elaborate on this point, the initial-state (*i.e.* $\tau = 0^+$) classical Yang-Mills results can be divided into two contributions. One consisting of glasma graphs corresponding to the connected diagrams shown in the previous section. The second contribution stems from seemingly disconnected graphs (disconnected on a perturbative level) but connected when the two gluons scatter on a common color field domain. This is similar in spirit to the effect seen in²³⁴ (where the proton was treated as a dilute object) and will be discussed in further detail in the upcoming section.

The classical simulations fail to reproduce the magnitude of the $v_2(p_T)$ at larger values of transverse momentum. The situation should worsen when hadronization is taken into account. Hadrons at a given p_T fragment from gluons of higher p_T and therefore the v_2 shown in figure 36 will be rescaled to lower p_T when hadronization is accounted for. This demonstrates the importance of including small- x evolution in the nuclear wavefunction absent in the classical Yang-Mills simulations. The classical Yang-Mills and glasma graph picture complement each-other quite nicely; the latter responsible for the large $p_T \gtrsim Q_S$ ridge due to intrinsic (*i.e.* non-factorizable) two-parton correlations including small- x evolution and the prior responsible for the softer ridge, $p_T \lesssim Q_S$ generated from the event-by-event breaking of rotational invariance.

We now turn to a discussion of the gluon $v_3(p_T)$ as shown in the right plot of figure 36. The first observation is that the initial v_3 at $\tau = 0^+$ is zero. This is a consequence of the initial gluon spectra being symmetric under $\mathbf{k}_\perp \rightarrow -\mathbf{k}_\perp$ resulting in the odd Fourier harmonics being identically zero at the initial time. This is consistent with the vanishing of odd harmonics in the glasma graph calculation.

At a proper-time of $\tau = 0.2$ fm/c a sizable v_3 has built up. Further evolution to $\tau = 0.4$ fm/c, where the system is practically free-streaming, results in a modest increase in the signal. The agreement between the event plane method and two particle correlations suggests that the event-by-event breaking of translational invariance combined with coherent final state effects is ultimately responsible for the v_3 . The most surprising finding is the lack of correlation between the global initial state eccentricity, ϵ_3 , and the p_T integrated v_3 on a per-event basis; refuting the notion that the source of v_3 is from the build up of a global energy-momentum flow via classical Yang-Mills dynamics.

Finally, we stress that the Yang Mills calculation²³³ is not able to reproduce the azimuthal anisotropy coefficients in A-A collisions, because of the large amount of uncorrelated color field domains present in a single collision and the lack of hydrodynamic evolution. This further confirms the standard interpretation of the v_n in heavy ion collisions as strong final state effects.

To summarize, the azimuthal correlations generated via the classical Yang-Mills simulations can be separated into three sources: 1) A genuine non-factorizable two-particle correlation – the glasma graph contribution 2) perturbatively disconnected graphs connected by the event-by-event breaking of rotational symmetry and 3) A contribution from final state interactions generated by the Yang-Mills dynamics. In the following section we review work that has focused on the second contribution; the event-by-event breaking of rotational symmetry.

4.4. Scattering from color-field domains

The basic idea can be traced back to Kovner and Lublinsky^{235,236} who argued that domains of color-electric fields of size $1/Q_S$ will produce non-trivial angular correlations in the single-particle distribution. Following their arguments, this can be easily seen by considering the scattering of two projectiles from a stationary (in the lab frame) hadronic target. The two projectiles may have different rapidities but at high enough energies their wave functions are boost invariant. Therefore the long-range nature of the correlations are a general consequence of the high-energy limit. If the two projectiles strike the target at the same impact parameter both will see the same color configuration in the target and be scattered in similar directions. This provides the source of near-side correlations. If the projectiles under consideration are gluons, it is just as likely that they can have *opposite charge* (as gluons transform in the adjoint representation of SU(3)) and therefore scatter in opposite directions. For quarks in the fundamental representation this would not be the case and the near-/away-side symmetry would be broken. As the size of correlated domains in the target are of order $1/Q_S^2(\text{target})$ we parametrically expect the strength of the two particle correlation to go as $(Q_S^2 S_\perp)^{-1}$ where S_\perp is the overlap area.

So far this is conceptually identical to what has been done in the previous section on glasma graphs except considered in a different Lorentz frame. Indeed the work

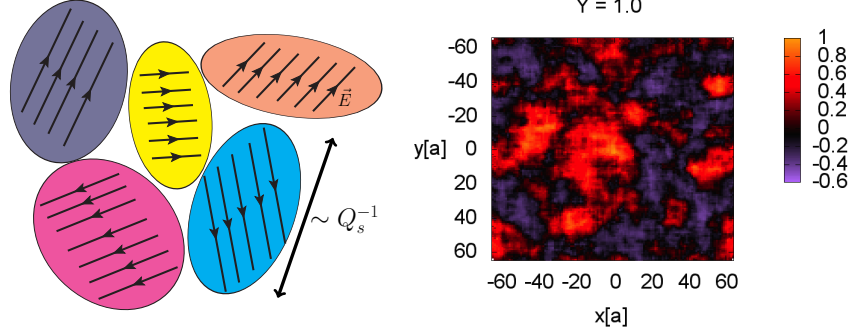


Fig. 37. Left: Schematic illustration of localized domains of chromo-electric fields in the target. Right: The dipole operator $1/N_c \text{Tr} V(\mathbf{x}_\perp) V^\dagger(\mathbf{y}_\perp)$ after evolution by the JIMWLK equation demonstrating the persistence of local fluctuations of the Wilson line.¹⁷⁸

of²³⁵ obtains the same glasma graphs when using a Gaussian weight functional for the color charge densities.

It was argued however that the Gaussian averaging procedure may underestimate the strength of the correlation. In the Gaussian approximation the two-gluon production is written as a term that factorizes into a product of single inclusive distributions and eight remaining connected diagrams (the glasma graphs considered earlier), the latter of which are N_c^2 suppressed,

$$\left\langle \frac{d^2 N}{dy_p d^2 \mathbf{p}_\perp dy_q d^2 \mathbf{q}_\perp} \right\rangle_{\text{Gaussian}} \sim \left\langle \frac{dN}{dy_p d^2 \mathbf{p}_\perp} \right\rangle \left\langle \frac{dN}{dy_q d^2 \mathbf{q}_\perp} \right\rangle + \frac{1}{N_c^2} (8 \text{ glasma graphs}) . \quad (44)$$

However, in the Gaussian approximation this first term has no azimuthal correlations – it corresponds to the independent emission of two gluons. An analysis going beyond leading order in N_c has found that the four-point function does not necessarily factorize into a product of two-point functions²³⁷ and these factorization breaking terms contribute at leading order in N_c to correlated two-gluon production.

A model for the generation of initial state azimuthal asymmetry from scattering from color domains was introduced in.²³⁴ It was shown that scattering of a dipole of size $\sim 1/p_T$ from a target with fixed configuration of color electric field reproduces the p_T dependence of v_2 and v_4 for a sufficiently polarized target.

Conventionally in the MV model the averaging over the field configurations of the target using a Gaussian correlator,

$$\frac{g^2}{N_c} \langle E_i^a(\mathbf{b}_1) E_j^b(\mathbf{b}_2) \rangle = \frac{1}{(N_c^2 - 1)} \delta^{ab} \delta_{ij} Q_S^2 \Delta(\mathbf{b}_1 - \mathbf{b}_2) \quad (45)$$

will result in isotropic particle production. In order to take into account observables that are sensitive to the breaking of translation invariance on a per-event level a model is introduced such that the target configurations are constrained such that

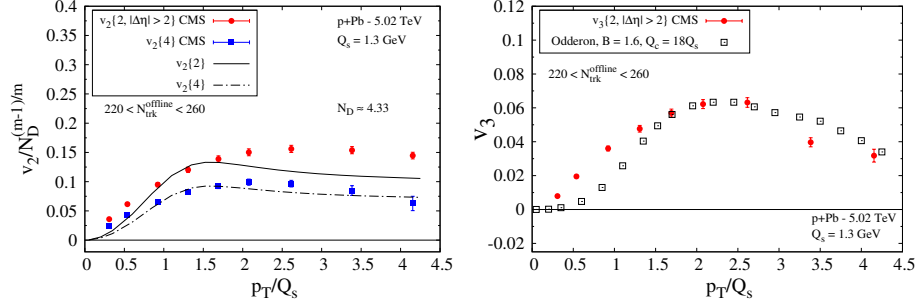


Fig. 38. Comparison of the color domain model of²³⁴ with $v_2(\mathbf{p}_\perp)$ (left) and $v_3(\mathbf{p}_\perp)$ (right) with high multiplicity p+Pb collisions.

the electric fields point in a specific direction \hat{a} ,

$$\frac{g^2}{N_c} \langle E_i^a(\mathbf{b}_1) E_j^b(\mathbf{b}_2) \rangle = \frac{1}{(N_c^2 - 1)} \delta^{ab} Q_S^2 \Delta(\mathbf{b}_1 - \mathbf{b}_2) \left(\delta_{ij} + 2\mathcal{A} \left[\hat{a}_i \hat{a}_j - \frac{1}{2} \delta_{ij} \right] \right) \quad (46)$$

The above expression takes into account that in the vicinity of $\mathbf{b}_1 \sim \mathbf{b}_2$ there is a subclass of events that have a predefined orientation and the average over these subclasses are done *after* the observable has been computed.

In this framework there exists a correlation even at the single particle level,

$$\langle \cos n(\phi_p - \phi_{\hat{a}}) \rangle(\mathbf{p}_\perp) = \int d\phi_p \langle \cos n(\phi_p - \phi_{\hat{a}}) \left\langle \frac{dN}{dy_p d^2\mathbf{p}_\perp} \right\rangle_{\hat{a}} \rangle. \quad (47)$$

and will correspondingly produce azimuthal correction in the disconnected terms in higher order cumulants.

One of the strengths of the above model is that it is able to accommodate a negative $c_2\{4\}$ ²³⁸

$$c_2\{4\} = -\frac{1}{N_D^3} \left(\mathcal{A}^4 - \frac{1}{4(N_c^2 - 1)^3} \right) \quad (48)$$

Furthermore, the consideration of C-odd fluctuations in the target, related to the odderon, are able to generate a v_3 .

While the above color domain model appears to use only Gaussian fluctuations, (*i.e.* the only correlator used equation (46) is a two-point function) the separation of averages is outside of the assumptions of the CGC framework. Implicit in this separation of averages is that the angular fluctuations of the large- x color sources, ρ , evolve on a slower times scale. First the fast modes are averaged over with the modified two point function equation (46), second the observable is computed, and only then is the averaging over all possible electric field directions, \hat{a} performed as required by Gauge invariance.

A recent work²³⁹ has made the connection between the color domain model and non-gaussianities in the color glass condensate. We direct the reader there for further discussion of the interpretation of the polarization factor \mathcal{A} in the color

domain model and its relation to the possible sources of non-Gaussianity in the CGC effective theory.

4.5. Conclusions on initial state interactions in small systems

In conclusion, the previous sections have demonstrated how glasma graphs and classical Yang-Mills complement each other as two different approximations of the same effective theory of high energy nuclear collisions able to address different features of the data. The connection to the scattering from localized domains of color electric fields with finite polarization can be made by considering non-Gaussianities of the color charge correlators.

We conclude this section by briefly discussing two other initial state proposals. While these have yet to address the data at the same quantitative level as the hydrodynamic and CGC models discussed thus far, these proposals contain interesting ideas which should be explored further.

The work of^{240,241} demonstrates that angular correlations can be generated by the exchange of two BFKL Pomeron ladders. The transverse momentum exchanged by the Pomeron is conjugate to the impact parameter of the collision and as events with a fixed multiplicity correspond to a finite impact parameter, an asymmetry is generated. Motivated by Gribov Reggeon and Pomeron calculus it was shown that the correlation is long-range in rapidity and that a double-ridge signal is generated.

A more recent work²⁴² argued that non-abelian beam jet bremsstrahlung generates long range rapidity correlations having a hierarchy of non-trivial azimuthal harmonics. The anisotropies are generated from radiating clusters that have accumulated a net transverse momentum kick on an event-by-event basis. In addition to explaining the ridge in small colliding systems, it was argued that this mechanism may be able to explain the approximate energy independence of azimuthal asymmetries observed in the RHIC beam energy scan.

5. Future Directions

While a lot of progress has been made towards understanding novel long-range correlation phenomena in small colliding systems, many questions remain open, requiring future efforts by both experimental and theoretical communities. We consider the following two big questions we feel should be addressed in order for progress to be made in the coming years: 1) Have we reached a consensus on the nature of long-range correlation phenomena in small (and/or large) systems? 2) If a strongly-coupled QGP is indeed formed, what fundamentally new knowledge do we gain from small systems?

To answer these questions, we discuss a few possible future directions in this section:

- Further scrutiny of hydrodynamic paradigm
- Nature of the ridge in p-p collisions

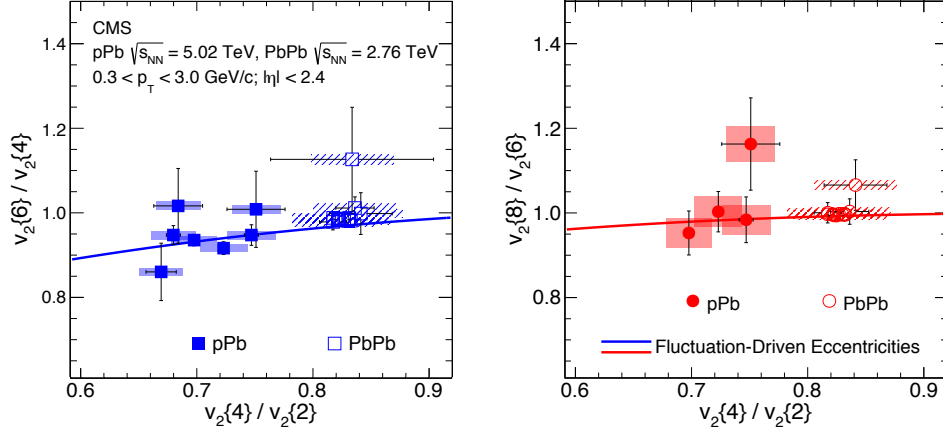


Fig. 39. Cumulant v_2 ratios, $v_2\{6\}/v_2\{4\}$ (left) and $v_2\{8\}/v_2\{6\}$ (right), as a function of $v_2\{4\}/v_2\{2\}$ ratios for high-multiplicity events in p-Pb collisions at $\sqrt{s_{NN}} = 5.02$ TeV and Pb-Pb collisions at $\sqrt{s_{NN}} = 2.76$ TeV.⁵⁴ The solid curves are predictions from a proposed universal behavior of fluctuation-driven eccentricities.⁴⁰

- Jet-medium interactions in p-p and p-Pb collisions
- Pre-equilibrium dynamics

5.1. Further scrutiny of hydrodynamic paradigm

The scrutiny of standard paradigms by identifying inconsistencies with experimental observations has been the recipe for many major scientific discoveries. In this light, precision studies of the hydrodynamic framework in small systems should be steadily pursued. The main theoretical challenge for p-p and p-A systems lies in the large uncertainties in determining the initial-state geometry, due to the lack of knowledge of the proton structure as well as its fluctuations, as discussed in Sec. 4.1. To make progress, identifying observables that are primarily sensitive to either the initial-state geometry or final-state dynamics is the most promising approach.

It was argued in Ref.⁴⁰ that for purely fluctuation driven initial-state anisotropies, such as in p-p and p-A collisions, the initial-state eccentricity distribution is universal. With the assumption of $v_2 \sim \epsilon_2$ motivated by hydrodynamics, the v_2 cumulants measured from 2-, 4-, 6-, and 8-particle correlations are predicted to follow a specific relation, as shown by the solid lines in Fig. 39 for ratios of $v_2\{6\}/v_2\{4\}$ and $v_2\{8\}/v_2\{6\}$ as a function of $v_2\{4\}/v_2\{2\}$. The recent experimental results in p-Pb collisions⁵⁴ (also shown in Fig. 39), seem to favor the theoretical predictions but clearly improvement in the experimental precision is needed before firm conclusions can be drawn. Additional information on the initial state fluctuations can also be extracted by measuring event-by-event v_2 distribution in p-Pb collisions, as was done in Pb-Pb collisions.¹⁰⁷

Correlations among flow harmonics v_n and the event planes (Ψ_n) are another

class of observable that may provide a valuable way of disentangling the effects of initial-state geometry from final-state evolution within hydrodynamical models. Such correlations were studied in great detail by the ATLAS collaboration in Pb-Pb collisions.^{243,244}

Similar measurements should be pursued in p-Pb collisions and compared to hydrodynamic calculations. For example, the correlation between v_2 and v_4 , or Ψ_2 and Ψ_4 , is generated by the non-linear response of hydrodynamic evolution, and one expects such a correlation to persist in small systems as well. The interpretation is different for Ψ_2 and Ψ_3 . Final-state hydrodynamic evolution does not induce a strong correlation between Ψ_2 and Ψ_3 and indeed this correlation was observed to be small in Pb-Pb collisions.²⁴³ However, it has been argued that a sizable correlation between Ψ_2 and Ψ_3 may be induced by large initial-state fluctuations in small colliding systems such as p-Pb.²⁴⁵ Similar event plane correlations measurements in p-Pb could therefore provide valuable information on the initial-state geometry.

Another observable that is mainly sensitive to the details of initial-state fluctuations is the transverse momentum dependent event plane fluctuations (of the same order). The measurement was carried out by the CMS collaboration in p-Pb and Pb-Pb collisions.⁸² Hydrodynamic calculations have indicated that this observable is sensitive to the granularity of the initial energy density fluctuations, instead of the η/s of the medium.⁸⁴ Evidence of significant rapidity-dependent event plane fluctuations in p-Pb and Pb-Pb collisions is also observed,⁸⁴ although it may be sensitive to both initial- and final-state effects in the longitudinal direction.²⁴⁶ Detailed studies of anisotropic flow observables and their correlations among each other in small systems, could provide crucial information on the initial-state in small systems if hydrodynamics is the correct framework to model these systems.

5.2. *Collectivity in p-p collisions*

While there has been a flood of new results on the long-range correlations in p-Pb collisions as summarized in Sec. 3, little progress has been made in addressing the nature of the ridge in p-p collisions since its first observation in 2010. Only recently have new measurements of the ridge in p-p become available²⁴⁷ with theoretical analysis closely following.²²⁴ A more recent work has attempted to extract the v_2 harmonics of long-range correlations by a careful fitting procedure between peripheral and central event classes in 13 TeV and 2.76 TeV.³⁸

As discussed in Sec. 4.1, hydrodynamic descriptions of small colliding systems are highly limited by the lack of knowledge of the initial conditions. Especially for p-A collisions, the initial-state eccentricity is highly sensitive to the shape of the proton and its fluctuations on very short timescales. Precision measurements of v_n harmonics from long-range correlations in p-p collisions should provide new constraints on the proton shape, and thus have the promise of improving the hydrodynamic modeling of p-p and p-A systems. Even more precise and independent measurements of the proton shape and its fluctuations would be possible with an

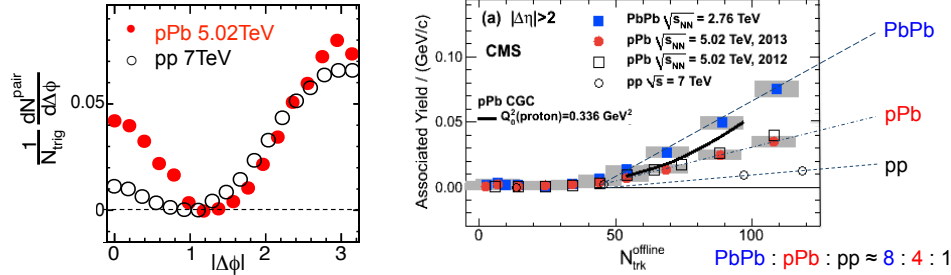


Fig. 40. Left: The 1-D long-range azimuthal ($\Delta\phi$) correlation functions in high-multiplicity p-p collisions at $\sqrt{s} = 7$ TeV and p-Pb collisions at $\sqrt{s_{NN}} = 5.02$ TeV.¹⁰ Right: long-range near-side associated yields for $1 \text{ GeV}/c < p_T < 2 \text{ GeV}/c$ as a function of multiplicity in p-p, p-Pb and Pb-Pb collisions.³⁵

electron ion Collider.²⁴⁸

The $\Delta\phi$ correlation for hadron pairs with $1 \text{ GeV}/c < p_T < 3 \text{ GeV}/c$ in p-p and p-Pb collisions are directly compared in Fig. 40 (left) at a comparable multiplicity. While the magnitudes of the away sides are similar, the near-side ridge yield in p-p is about four times smaller than in p-Pb. Extracting v_2 from p-p is difficult because of the larger relative contribution from the away-side jet yield. The near-side ridge yield as a function of multiplicity in p-p, p-Pb and Pb-Pb collisions is shown in Fig. 40 (right). Above around $N_{\text{trk}} \sim 40$, the ridge yield increases roughly linearly with multiplicity for all systems. At a given track multiplicity, the ridge yield in p-p collisions is roughly 25% and 10% of those observed in Pb-Pb and p-Pb collisions, respectively.

Associated yields that are collective are expected to grow linearly with event multiplicity, while short-range few-body correlations would be more or less independent of multiplicity (except for the bias towards enhanced jet correlations imposed by the selection of high multiplicity. However, this bias grows much more slowly than linearly with multiplicity). Therefore, pushing to sufficiently high multiplicities (e.g., $N_{\text{trk}} > 150$ –170), the collective component of correlations would eventually dominate. The application of the jet-yield subtraction procedure will be more reliable in that regime.

To shed further light on the situation in p-p collisions, one should aim to measure v_2 with multi-particle correlations. v_2 from multi-particle cumulants is less susceptible to jet correlations and could provide further insights. It is possible that a non-negligible amount of jet correlations may still be present in four-particle correlations for very-high-multiplicity p-p events. In that case, new methods of implementing an η gap among four particles is worth pursuing to suppress short-range jet correlations.

At the top LHC energy of $\sqrt{s} = 13$ –14 TeV for p-p collisions, a data sample with an integrated luminosity of 50 pb^{-1} should be large enough to achieve the goals

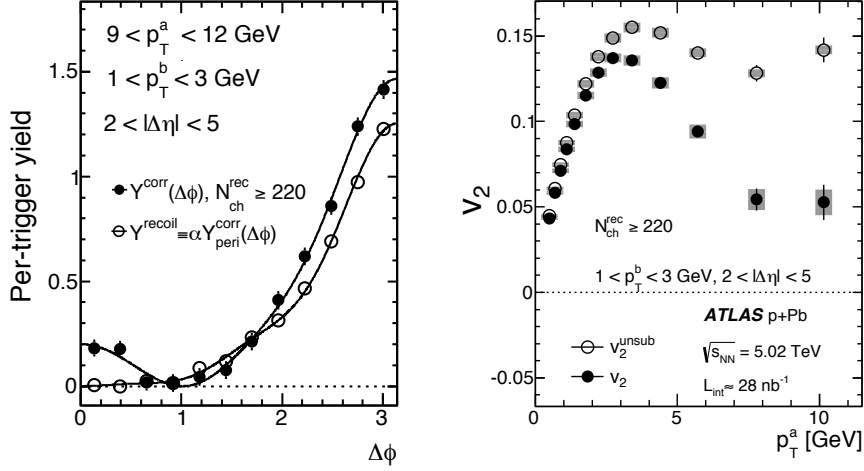


Fig. 41. Left: The 1-D long-range azimuthal ($\Delta\phi$) correlation functions for high- p_T (9–12 GeV/ c) trigger particles in pPb collisions at $\sqrt{s_{NN}} = 5.02$ TeV. Right: The v_2 values from long-range correlations as a function of p_T in high-multiplicity pPb collisions, up to very-high- p_T region, with (closed) and without (open) correcting for back-to-back jet correlations.³⁷

outlined above. Cross sections of high-multiplicity p-p events increase by more than a factor of 10 from $\sqrt{s} = 7$ TeV to $\sqrt{s} = 13$ TeV. However, it is necessary for these data to be delivered under a low pile-up condition (e.g., an average pile-up of 1–2 at CMS and ATLAS) so that the experiments are able to trigger on high-multiplicity events from single p-p interactions. A special run like this lasting for a few days at the LHC in the future would yield very exciting physics. Novel ideas of triggering on high-multiplicity events under high pile-up conditions is another opportunity where progress can be made.

5.3. Jet quenching in small systems

If the observed ridge-like correlations are related to strong final-state rescatterings inside the medium, interactions between high- p_T partons and the medium should also be present, leading to the “jet-quenching” phenomenon first observed in heavy-ion collisions at RHIC.

Due to a much smaller system size, the average path length of a parton traversing through a p-p or p-A system is much shorter. For this reason one might argue that little jet quenching should be expected. However, at similar multiplicities, a smaller system represents a higher energy density or temperature state. The parton energy loss depends on both the path length, L , and the transport coefficient \hat{q} , the mean transverse momentum squared accumulated by a hard parton per unit length. While the average L is reduced in small systems, \hat{q} increases with T^3 . A jet might lose just as much energy in a smaller but denser p-Pb system as in a larger

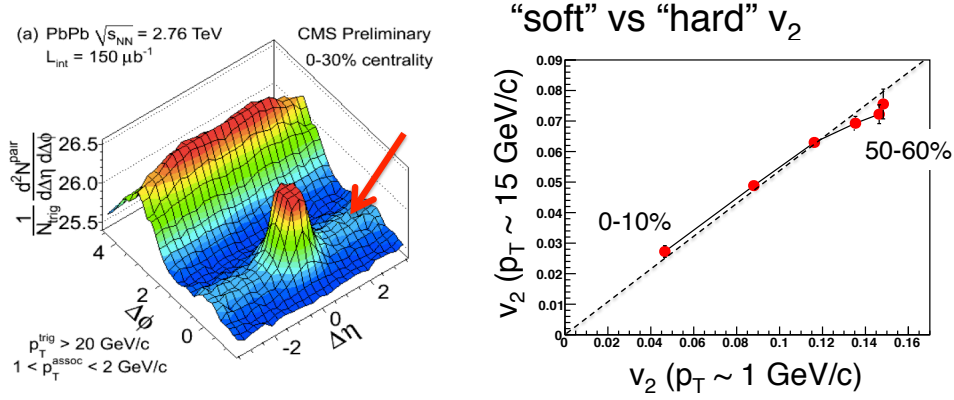


Fig. 42. Left: The 2-D $\Delta\eta$ - $\Delta\phi$ correlation function for high- p_T (> 20 GeV/c) trigger particles in Pb-Pb collisions at $\sqrt{s_{NN}} = 2.76$ TeV. Right: The v_2 values at high p_T (~ 15 GeV/c) versus low p_T (~ 1 GeV/c) for different centralities in Pb-Pb collisions.²⁵⁰

but more dilute Pb-Pb system. While early model calculations predicted a large jet quenching²⁴⁹ one would like to see modeling with the more realistic space-time evolution predicted by hydrodynamic calculations.

Initial results of high- p_T jets or hadrons in p-Pb collisions at the LHC indeed suggest no significant modification of high- p_T parton production.^{251, 252} However, what has been explored so far mainly concerns well-reconstructed jets at very high- p_T (e.g., > 120 GeV/c),²⁵¹ or lower- p_T hadrons but only in minimum bias pPb events.²⁵² Studies of the nuclear modification factor as a function of centrality in p-Pb collisions is highly challenging due to multiplicity selection biases, which remain inconclusive.²⁵³ Many studies have also indicated non-trivial correlations between the production of hard processes and underlying event activity, which is used for centrality determination in p-Pb collisions.²⁵³⁻²⁵⁵ So far, no clear path forward is laid out for the study of jet quenching in p-p and p-A collisions.

Looking for azimuthal anisotropies (v_2) of high- p_T particles can avoid the multiplicity biases and provide us a hint of the (non-)existence of jet quenching. The fact that the near-side ridge yield persists to the high- p_T region suggests finite v_2 values of high- p_T particles, as shown in Fig. 41 by the ATLAS collaboration.³⁷ Assuming back-to-back jet correlations are not significantly modified, the ATLAS collaboration extracted v_2 up to high p_T in high-multiplicity p-Pb collisions, where a sizable v_2 of about 5% is observed at $p_T \sim 10$ GeV/c, shown in Fig. 41.

In Pb-Pb collisions, a long-range near-side correlation structure for a trigger particle with $p_T > 20$ GeV/c is clearly visible (Fig. 42, left).²⁵⁰ Furthermore, the v_2 values obtained at high p_T and low p_T from different centrality ranges of Pb-Pb collisions are found to be strongly correlated (Fig. 42, right), indicating a common origin, i.e., that both are related to the initial-state geometry. It will be very

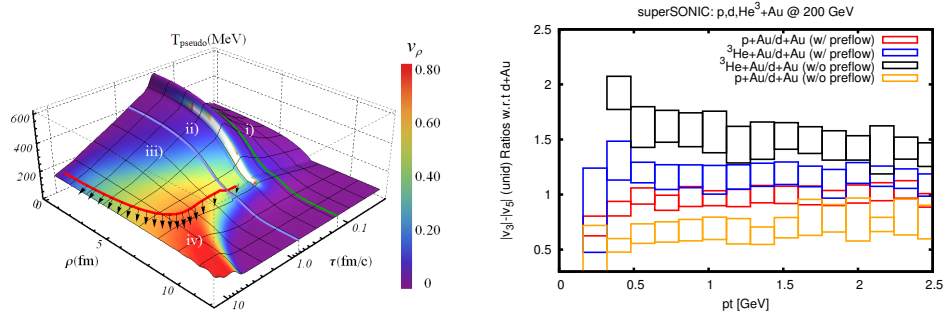


Fig. 43. Left: The radial velocity v_ρ extracted as a function of τ (time) and ρ (radius) for a representative simulation from Ref.²⁵⁸ with pre-equilibrium dynamics. Right: Ratios of v_3 between ^3He -Au, p-Au and d-Au as a function of p_T at $\sqrt{s_{NN}} = 200$ GeV from the superSONIC model with and without pre-equilibrium flow.¹⁵⁷

interesting to perform the same study in p-p and p-Pb collisions to gain some insight into the nature of long-range correlations at high p_T . Moreover, performing multi-particle v_2 measurements in the high- p_T region in p-p and p-Pb would help minimize the influence of short-range jet correlations and help clarify the picture of high- p_T azimuthal anisotropy.

5.4. Pre-equilibrium dynamics

The strong anisotropic flow of final-state particles in heavy-ion collisions has been regarded as evidence for thermalization realized during the very early stages of the collision. However, understanding the detailed mechanism of the fast thermalization process has been a big challenge in the field.²⁵⁶ In most hydrodynamic models, a QGP thermalization or formation time, τ_0 , is usually assumed, after which the hydrodynamic evolution is switched on. This additional freedom allows for the tuning of models to match experimental data. Often, physics in the pre-equilibrium stage as well as its transition to a strongly-coupled QGP state is ignored, even though it is likely to have relevant effects on final-state observables (for example, its influence on HBT radii has been argued to be important²⁵⁷).

The IP-Glasma model^{34,116} includes some pre-equilibrium dynamics via the Yang Mills equations from time zero. However, a switch to hydrodynamics at a time τ_0 is still necessary, because the 2+1 dimensional Yang Mills simulation does not contain the necessary dynamics, which possibly includes the development of Weibel instabilities, to isotropize the system to the point where a matching with hydrodynamics can be completed. However, the build up of flow within the first ~ 0.4 fm/c is comparable in the Yang Mills and hydrodynamic picture, making the final state observables independent of the switching time τ_0 .³³

Progress has also been made in the superSONIC model, where pre-equilibrium dynamics and its transition to the hydrodynamic regime is treated in a coherent

way without any explicit switching time.^{157,258} Fig. 43 (left) shows the development of the radial flow velocity profile as a function of time and radius going from the pre-equilibrium stage to the viscous hydrodynamic regime.²⁵⁸ Most importantly, simulation results from the superSONIC model indicate that flow developed during the pre-equilibrium stage has a significant contribution for small colliding systems since the total lifetime of a small system is much shorter. This can be clearly seen in Fig. 43 (right) for the ratios of v_3 between $^3\text{He-Au}$, p-Au and d-Au as a function of p_T at $\sqrt{s_{NN}} = 200$ GeV, compared with and without pre-equilibrium flow.¹⁵⁷ A lot of work still lies ahead before any solid conclusion can be drawn but high-multiplicity, small colliding systems promise to open a new window for probing the pre-equilibrium dynamics in heavy-ion collisions.

6. Summary

In summary, the observation of long-range correlations in high-multiplicity p-p and p-Pb collisions has opened up new opportunities for investigating novel high-density QCD phenomena in small colliding systems. Experimental results from RHIC and the LHC over the past several years have provided crucial insights and imposed stringent constraints on possible theoretical interpretations.

We reviewed the theoretical progress in the hydrodynamic modeling of small colliding systems. The current status is that hydrodynamic models are able to describe all the features of the experimental data at a largely quantitative level. However, a large sensitivity to the unknown initial state in small systems remains. Without further constraints on initial state models it will be difficult to distill information on the medium produced in small systems and scrutinize the hydrodynamic paradigm. Clearly hydrodynamics is being pushed to the edge of its validity in these small colliding systems and further theoretical work is needed to assess higher order corrections.

Calculations based on the Color Glass Condensate effective theory can also describe many characteristic features of the experimental data. If one can conclusively show that the correlations are generated by glasma graphs, valuable information about multi-gluon correlations in the nuclear wave-function can be obtained; multi-particle correlations can serve as a sensitive probe of saturation dynamics.

Ideally these frameworks should be merged. We have a wealth of information from deep inelastic scattering that should be incorporated into our modeling of the initial state. How the initial gluon fields decohere, isotropize and possibly thermalize to a system that can be described hydrodynamically is an open question. We have argued above that classical Yang-Mills dynamics contains many of the missing pieces of the glasma graph framework. Furthermore, the recently proposed color domain models can accommodate a negative $c_2\{4\}$, and is highly interesting from a theoretical point of view as it could provide a measure of non-Gaussianities in the hadronic wavefunction.

The strongest conclusion that can be made at this time is that the discovery

potential from small colliding systems is immense. The detailed experimental information that has and will continue to come from these experiments will allow the community to test theoretical proposals at an unprecedented level of accuracy. Studying collectivity in high-energy proton-proton and proton-nucleus collisions provide us with access to a rich variety of emergent (and possibly yet undiscovered) QCD phenomena.

Acknowledgements

We thank Jurgen Schukraft for providing valuable feedback on an early version of this manuscript. BPS is supported under DOE Contract No. DE-SC0012704. BPS acknowledges a DOE Office of Science Early Career Award. WL acknowledges funding from a DOE Office of Science Early Career Award (Contract No. DE-SC0012185), from the Welch Foundation (Grant No. C-1845) and from an Alfred P. Sloan Research Fellowship (No. FR-2015-65911).

References

1. BRAHMS Collaboration (I. Arsene *et al.*), *Nucl. Phys. A* **757** (2005) 1, [arXiv:nucl-ex/0410020](#) [nucl-ex].
2. PHENIX Collaboration (K. Adcox *et al.*), *Nucl. Phys. A* **757** (2005) 184, [arXiv:nucl-ex/0410003](#) [nucl-ex].
3. PHOBOS Collaboration (B. B. Back *et al.*), *Nucl. Phys. A* **757** (2005) 28, [arXiv:nucl-ex/0410022](#) [nucl-ex].
4. STAR Collaboration (J. Adams *et al.*), *Nucl. Phys. A* **757** (2005) 102, [arXiv:nucl-ex/0501009](#) [nucl-ex].
5. CMS Collaboration (V. Khachatryan *et al.*), *JHEP* **09** (2010) 091, [arXiv:1009.4122](#) [hep-ex].
6. CMS Collaboration (S. Chatrchyan *et al.*), *Eur. Phys. J. C* **72** (2012) 2012, [arXiv:1201.3158](#) [nucl-ex].
7. W. Li, *Mod. Phys. Lett. A* **27** (2012) 1230018, [arXiv:1206.0148](#) [nucl-ex].
8. ALICE Collaboration (B. Abelev *et al.*), *Phys. Lett. B* **719** (2013) 29, [arXiv:1212.2001](#) [nucl-ex].
9. ATLAS Collaboration (G. Aad *et al.*), *Phys. Rev. Lett.* **110** (2013) 182302, [arXiv:1212.5198](#) [hep-ex].
10. CMS Collaboration (S. Chatrchyan *et al.*), *Phys. Lett. B* **718** (2013) 795, [arXiv:1210.5482](#) [nucl-ex].
11. PHENIX Collaboration (A. Adare *et al.*), *Phys. Rev. Lett.* **114** (2015) 192301, [arXiv:1404.7461](#) [nucl-ex].
12. PHENIX Collaboration (A. Adare *et al.*), *Phys. Rev. Lett.* **115** (2015) 142301, [arXiv:1507.06273](#) [nucl-ex].
13. J.-Y. Ollitrault, *Phys. Rev. D* **46** (1992) 229.
14. C. Gale, S. Jeon and B. Schenke, *Int. J. Mod. Phys. A* **28** (2013) 1340011, [arXiv:1301.5893](#) [nucl-th].
15. PHOBOS Collaboration (B. Alver *et al.*), *Phys. Rev. C* **81** (2010) 024904, [arXiv:0812.1172](#) [nucl-ex].
16. PHENIX Collaboration (K. Adcox *et al.*), *Nucl. Phys. A* **757** (2005) 184, [arXiv:nucl-ex/0410003](#).

17. STAR Collaboration (J. Adams *et al.*), *Nucl. Phys. A* **757** (2005) 102, [arXiv:nucl-ex/0501009](#).
18. B. B. Back *et al.*, *Nucl. Phys. A* **757** (2005) 28, [arXiv:nucl-ex/0410022](#).
19. PHENIX Collaboration (S. S. Adler *et al.*), *Phys. Rev. Lett.* **94** (2005) 232302.
20. STAR Collaboration (G. Agakishiev *et al.*), *Phys. Rev. C* **85** (2012) 014901.
21. PHOBOS Collaboration (B. Alver *et al.*), *Phys. Rev. Lett.* **98** (2007) 242302.
22. CMS Collaboration (S. Chatrchyan *et al.*), *Phys. Rev. C* **87** (2013) 014902, [arXiv:1204.1409 \[nucl-ex\]](#).
23. ALICE Collaboration (K. Aamodt *et al.*), *Phys. Rev. Lett.* **105** (2010) 252302, [arXiv:1011.3914 \[nucl-ex\]](#).
24. ATLAS Collaboration (G. Aad *et al.*), *Phys. Lett. B* **707** (2012) 330, [arXiv:1108.6018 \[hep-ex\]](#).
25. CMS Collaboration (S. Chatrchyan *et al.*), *JHEP* **02** (2014) 088, [arXiv:1312.1845 \[nucl-ex\]](#).
26. B. Alver and G. Roland, *Phys. Rev. C* **81** (2010) 054905, [arXiv:1003.0194 \[nucl-th\]](#), [Erratum: *Phys. Rev. C* **82**, 039903(2010)].
27. B. H. Alver, C. Gombeaud, M. Luzum and J.-Y. Ollitrault, *Phys. Rev. C* **82** (2010) 034913, [arXiv:1007.5469 \[nucl-th\]](#).
28. B. Schenke, S. Jeon and C. Gale, *Phys. Rev. Lett.* **106** (2011) 042301, [arXiv:1009.3244 \[hep-ph\]](#).
29. H. Petersen *et al.*, *Phys. Rev. C* **82** (2010) 041901, [arXiv:1008.0625 \[nucl-th\]](#).
30. J. Xu and C. M. Ko, *Phys. Rev. C* **83** (2011) 021903, [arXiv:1011.3750 \[nucl-th\]](#).
31. D. Teaney and L. Yan, *Phys. Rev. C* **83** (2011) 064904, [arXiv:1010.1876 \[nucl-th\]](#).
32. S. Voloshin and Y. Zhang, *Z. Phys. C* **70** (1996) 665, [arXiv:hep-ph/9407282 \[hep-ph\]](#).
33. C. Gale, S. Jeon, B. Schenke, P. Tribedy and R. Venugopalan, *Phys. Rev. Lett.* **110** (2013) 012302, [arXiv:1209.6330 \[nucl-th\]](#).
34. B. Schenke, P. Tribedy and R. Venugopalan, *Phys. Rev. Lett.* **108** (2012) 252301, [arXiv:1202.6646 \[nucl-th\]](#).
35. CMS Collaboration (S. Chatrchyan *et al.*), *Phys. Lett. B* **724** (2013) 213, [arXiv:1305.0609 \[nucl-ex\]](#).
36. N. Armesto, N. Borghini, S. Jeon, U. A. Wiedemann, S. Abreu, V. Akkelin, J. Alam, J. L. Albacete, A. Andronic, D. Antonov *et al.*, *J. Phys. G* **35** (2008) 054001, [arXiv:0711.0974 \[hep-ph\]](#).
37. ATLAS Collaboration (G. Aad *et al.*), *Phys. Rev. C* **90** (2014) 044906, [arXiv:1409.1792 \[hep-ex\]](#).
38. ATLAS Collaboration (G. Aad *et al.*) (2015) [arXiv:1509.04776 \[hep-ex\]](#).
39. ATLAS Collaboration (G. Aad *et al.*), *Phys. Rev. C* **86** (2012) 014907, [arXiv:1203.3087 \[hep-ex\]](#).
40. L. Yan and J.-Y. Ollitrault, *Phys. Rev. Lett.* **112** (2014) 082301, [arXiv:1312.6555 \[nucl-th\]](#).
41. G. Baar and D. Teaney, *Phys. Rev. C* **90** (2014) 054903, [arXiv:1312.6770 \[nucl-th\]](#).
42. A. Bzdak, P. Bozek and L. McLerran, *Nucl. Phys. A* **927** (2014) 15, [arXiv:1311.7325 \[hep-ph\]](#).
43. A. Bzdak and V. Skokov, *Nucl. Phys. A* **943** (2015) 1, [arXiv:1312.7349 \[hep-ph\]](#).
44. N. Borghini, P. M. Dinh and J.-Y. Ollitrault, *Phys. Rev. C* **64** (2001) 054901, [arXiv:nucl-th/0105040 \[nucl-th\]](#).
45. R. Bhalerao, N. Borghini and J. Ollitrault, *Phys. Lett. B* **580** (2004) 157, [arXiv:nucl-th/0307018 \[nucl-th\]](#).

46. A. Bilandzic, R. Snellings and S. Voloshin, *Phys. Rev. C* **83** (2011) 044913, [arXiv:1010.0233 \[nucl-ex\]](#).
47. NA49 Collaboration (C. Alt *et al.*), *Phys. Rev. C* **68** (2003) 034903, [arXiv:nucl-ex/0303001 \[nucl-ex\]](#).
48. STAR Collaboration (C. Adler *et al.*), *Phys. Rev. C* **66** (2002) 034904, [arXiv:nucl-ex/0206001 \[nucl-ex\]](#).
49. ALICE Collaboration (B. Abelev *et al.*), *Phys. Lett. B* **719** (2013) 18, [arXiv:1205.5761 \[nucl-ex\]](#).
50. CMS Collaboration (S. Chatrchyan *et al.*), *Phys. Rev. C* **89** (2014) 044906, [arXiv:1310.8651 \[nucl-ex\]](#).
51. ATLAS Collaboration (G. Aad *et al.*), *Eur. Phys. J. C* **74** (2014) 3157, [arXiv:1408.4342 \[hep-ex\]](#).
52. ATLAS Collaboration (G. Aad *et al.*), *Phys. Lett. B* **725** (2013) 60, [arXiv:1303.2084 \[hep-ex\]](#).
53. ALICE Collaboration (B. B. Abelev *et al.*), *Phys. Rev. C* **90** (2014) 054901, [arXiv:1406.2474 \[nucl-ex\]](#).
54. CMS Collaboration (V. Khachatryan *et al.*), *Phys. Rev. Lett.* **115** (2015) 012301, [arXiv:1502.05382 \[nucl-ex\]](#).
55. ALICE Collaboration (B. B. Abelev *et al.*), *Phys. Lett. B* **728** (2014) 25, [arXiv:1307.6796 \[nucl-ex\]](#).
56. CMS Collaboration (S. Chatrchyan *et al.*), *Eur. Phys. J. C* **72** (2012) 2164, [arXiv:1207.4724 \[hep-ex\]](#).
57. CMS Collaboration (S. Chatrchyan *et al.*), *Eur. Phys. J. C* **74** (2014) 2847, [arXiv:1307.3442 \[hep-ex\]](#).
58. ALICE Collaboration (B. Abelev *et al.*), *Phys. Rev. C* **88** (2013) 044910, [arXiv:1303.0737 \[hep-ex\]](#).
59. ALICE Collaboration (B. B. Abelev *et al.*), *Phys. Lett. B* **726** (2013) 164, [arXiv:1307.3237 \[nucl-ex\]](#).
60. CMS Collaboration (V. Khachatryan *et al.*), *Phys. Lett. B* **742** (2015) 200, [arXiv:1409.3392 \[nucl-ex\]](#).
61. E. Schnedermann, J. Sollfrank and U. Heinz, *Phys. Rev. C* **48** (1993) 2462.
62. E. Shuryak and I. Zahed, *Phys. Rev. C* **88** (2013) 044915, [arXiv:1301.4470 \[hep-ph\]](#).
63. T. Kalaydzhyan and E. Shuryak, *Phys. Rev. C* **90** (2014) 014901, [arXiv:1404.1888 \[hep-ph\]](#).
64. T. Kalaydzhyan and E. Shuryak, *Phys. Rev.* **C91** (2015) 054913, [arXiv:1503.05213 \[hep-ph\]](#).
65. P. Z. Skands and D. Wicke, *Eur. Phys. J. C* **52** (2007) 133, [arXiv:hep-ph/0703081 \[HEP-PH\]](#).
66. H. Schulz and P. Skands, *Eur. Phys. J. C* **71** (2011) 1644, [arXiv:1103.3649 \[hep-ph\]](#).
67. L. McLerran, M. Praszalowicz and B. Schenke, *Nucl. Phys. A* **916** (2013) 210, [arXiv:1306.2350 \[hep-ph\]](#).
68. PHENIX Collaboration (S. S. Adler *et al.*), *Phys. Rev. Lett.* **91** (2003) 182301, [arXiv:nucl-ex/0305013 \[nucl-ex\]](#).
69. STAR Collaboration (C. Adler *et al.*), *Phys. Rev. Lett.* **87** (2001) 182301, [arXiv:nucl-ex/0107003 \[nucl-ex\]](#).
70. ALICE Collaboration (B. B. Abelev *et al.*), *JHEP* **06** (2015) 190, [arXiv:1405.4632 \[nucl-ex\]](#).
71. P. Huovinen, P. F. Kolb, U. W. Heinz, P. V. Ruuskanen and S. A. Voloshin, *Phys.*

- Lett. B* **503** (2001) 58, [arXiv:hep-ph/0101136](#) [hep-ph].
72. P. F. Kolb and U. W. Heinz, Hydrodynamic description of ultrarelativistic heavy-ion collisions, in *Quark gluon plasma 3*, eds. R. C. Hwa and X. N. Wang (World Scientific, Singapore, 2003), p. 634. [arXiv:nucl-th/0305084](#).
 73. C. Shen, U. Heinz, P. Huovinen and H. Song, *Phys. Rev. C* **84** (2011) 044903, [arXiv:1105.3226](#) [nucl-th].
 74. K. Werner, M. Bleicher, B. Guiot, I. Karpenko and T. Pierog, *Phys. Rev. Lett.* **112** (2014) 232301, [arXiv:1307.4379](#) [nucl-th].
 75. P. Bożek, W. Broniowski and G. Torrieri, *Phys. Rev. Lett.* **111** (2013) 172303, [arXiv:1307.5060](#) [nucl-th].
 76. STAR Collaboration (J. Adams *et al.*), *Phys. Rev. Lett.* **92** (2004) 052302, [arXiv:nucl-ex/0306007](#) [nucl-ex].
 77. STAR Collaboration (B. I. Abelev *et al.*), *Phys. Rev. C* **75** (2007) 054906, [arXiv:nucl-ex/0701010](#) [nucl-ex].
 78. PHENIX Collaboration (A. Adare *et al.*), *Phys. Rev. Lett.* **98** (2007) 162301, [arXiv:nucl-ex/0608033](#) [nucl-ex].
 79. D. Molnar and S. A. Voloshin, *Phys. Rev. Lett.* **91** (2003) 092301, [arXiv:nucl-th/0302014](#) [nucl-th].
 80. V. Greco, C. M. Ko and P. Levai, *Phys. Rev. Lett.* **90** (2003) 202302, [arXiv:nucl-th/0301093](#) [nucl-th].
 81. R. J. Fries, B. Muller, C. Nonaka and S. A. Bass, *Phys. Rev. Lett.* **90** (2003) 202303, [arXiv:nucl-th/0301087](#) [nucl-th].
 82. CMS Collaboration (V. Khachatryan *et al.*) (2015) [arXiv:1503.01692](#) [nucl-ex].
 83. U. Heinz, Z. Qiu and C. Shen, *Phys. Rev. C* **87** (2013) 034913, [arXiv:1302.3535](#) [nucl-th].
 84. I. Kozlov, M. Luzum, G. Denicol, S. Jeon and C. Gale (2014) [arXiv:1405.3976](#) [nucl-th].
 85. F. G. Gardim, F. Grassi, M. Luzum and J.-Y. Ollitrault, *Phys. Rev. C* **87** (2013) 031901, [arXiv:1211.0989](#) [nucl-th].
 86. S. Floerchinger and U. A. Wiedemann, *Phys. Lett. B* **728** (2014) 407, [arXiv:1307.3453](#) [hep-ph].
 87. C. E. Coleman-Smith, H. Petersen and R. L. Wolpert, *J. Phys. G* **40** (2013) 095103, [arXiv:1204.5774](#) [hep-ph].
 88. A. Mazeliauskas and D. Teaney, *Phys. Rev. C* **91** (2015) 044902, [arXiv:1501.03138](#) [nucl-th].
 89. ALICE Collaboration (J. Adam *et al.*), *Phys. Rev. C* **91** (2015) 034906, [arXiv:1502.00559](#) [nucl-ex].
 90. T. Matsui and H. Satz, *Phys. Lett. B* **178** (1986) 416.
 91. CMS Collaboration (S. Chatrchyan *et al.*), *JHEP* **04** (2014) 103, [arXiv:1312.6300](#) [nucl-ex].
 92. ALICE Collaboration (J. Adam *et al.*) (2015) [arXiv:1505.00664](#) [nucl-ex].
 93. A. Dumitru, F. Gelis, L. McLerran and R. Venugopalan, *Nucl. Phys. A* **810** (2008) 91, [arXiv:0804.3858](#) [hep-ph].
 94. F. B. Yano and S. E. Koonin, *Phys. Lett. B* **78** (1978) 556.
 95. M. I. Podgoretsky, *Sov. J. Nucl. Phys.* **37** (1983) 272, [Yad. Fiz.37,455(1983)].
 96. Y. F. Wu, U. W. Heinz, B. Tomasik and U. A. Wiedemann, *Eur. Phys. J. C* **1** (1998) 599, [arXiv:nucl-th/9607044](#) [nucl-th].
 97. M. A. Lisa, S. Pratt, R. Soltz and U. Wiedemann, *Ann. Rev. Nucl. Part. Sci.* **55** (2005) 357, [arXiv:nucl-ex/0505014](#) [nucl-ex].
 98. PHOBOS Collaboration (B. Alver *et al.*), *Phys. Rev. C* **81** (2010) 024904,

- arXiv:0812.1172 [nucl-ex].
99. PHOBOS Collaboration (B. Alver *et al.*), *Phys. Rev. Lett.* **104** (2010) 062301, arXiv:0903.2811 [nucl-ex].
 100. K. Dusling, F. Gelis, T. Lappi and R. Venugopalan, *Nucl. Phys. A* **836** (2010) 159, arXiv:0911.2720 [hep-ph].
 101. D. Teaney, J. Lauret and E. V. Shuryak, *Phys. Rev. Lett.* **86** (2001) 4783, arXiv:nucl-th/0011058 [nucl-th].
 102. T. Hirano and K. Tsuda, *Phys. Rev. C* **66** (2002) 054905.
 103. P. Huovinen, *Quark Gluon Plasma 3 ed R C Hwa and X N Wang (Singapore: World Scientific)* (2003) 600, arXiv:nucl-th/0305064.
 104. R. Derradi de Souza, T. Koide and T. Kodama, *Prog. Part. Nucl. Phys.* **86** (2016) 35, arXiv:1506.03863 [nucl-th].
 105. S. Ryu, J. F. Paquet, C. Shen, G. S. Denicol, B. Schenke, S. Jeon and C. Gale, *Phys. Rev. Lett.* **115** (2015) 132301, arXiv:1502.01675 [nucl-th].
 106. B. Schenke and R. Venugopalan, *Phys. Rev. Lett.* **113** (2014) 102301, arXiv:1405.3605 [nucl-th].
 107. ATLAS Collaboration (G. Aad *et al.*), *JHEP* **11** (2013) 183, arXiv:1305.2942 [hep-ex].
 108. L. Landau, *Ser. Fiz.* **17** (1953) 51.
 109. S. Belenkji and L. Landau, *Il Nuovo Cimento* **3** (1956) 15.
 110. K. Werner, I. Karpenko, T. Pierog, M. Bleicher and K. Mikhailov, *Phys. Rev. C* **83** (2011) 044915, arXiv:1010.0400 [nucl-th].
 111. K. Werner, I. Karpenko and T. Pierog, *Phys. Rev. Lett.* **106** (2011) 122004, arXiv:1011.0375 [hep-ph].
 112. P. Bozek, *Phys. Rev. C* **85** (2012) 014911, arXiv:1112.0915 [hep-ph].
 113. P. Bozek and W. Broniowski, *Phys. Lett. B* **718** (2013) 1557, arXiv:1211.0845 [nucl-th].
 114. K. Werner, B. Guiot, I. Karpenko and T. Pierog, *Phys. Rev. C* **89** (2014) 064903, arXiv:1312.1233 [nucl-th].
 115. M. L. Miller, K. Reygers, S. J. Sanders and P. Steinberg, *Ann. Rev. Nucl. Part. Sci.* **57** (2007) 205, arXiv:nucl-ex/0701025 [nucl-ex].
 116. B. Schenke, P. Tribedy and R. Venugopalan, *Phys. Rev. C* **86** (2012) 034908, arXiv:1206.6805 [hep-ph].
 117. P. Bozek and W. Broniowski, *Phys. Rev. C* **88** (2013) 014903, arXiv:1304.3044 [nucl-th].
 118. W. Broniowski, M. Rybczycki and P. Boek, *Computer Physics Communications* **180** (2009) 69.
 119. E. Iancu and R. Venugopalan (2003) arXiv:hep-ph/0303204 [hep-ph].
 120. H. Kowalski and D. Teaney, *Phys. Rev. D* **68** (2003) 114005, arXiv:hep-ph/0304189 [hep-ph].
 121. A. Kovner, L. D. McLerran and H. Weigert, *Phys. Rev. D* **52** (1995) 6231.
 122. Y. V. Kovchegov and D. H. Rischke, *Phys. Rev. C* **56** (1997) 1084.
 123. A. Krasnitz and R. Venugopalan, *Nucl. Phys. B* **557** (1999) 237.
 124. A. Krasnitz and R. Venugopalan, *Phys. Rev. Lett.* **84** (2000) 4309.
 125. A. Krasnitz and R. Venugopalan, *Phys. Rev. Lett.* **86** (2001) 1717.
 126. T. Lappi, *Phys. Rev. C* **67** (2003) 054903.
 127. B. Schenke, P. Tribedy and R. Venugopalan, *Phys. Rev. C* **89** (2014) 024901, arXiv:1311.3636 [hep-ph].
 128. J. Bartels, K. J. Golec-Biernat and H. Kowalski, *Phys. Rev. D* **66** (2002) 014001.
 129. A. H. Rezaeian, M. Siddikov, M. Van de Klundert and R. Venugopalan, *Phys. Rev.*

- D* **87** (2013) 034002, [arXiv:1212.2974 \[hep-ph\]](#).
130. A. Kovner, L. D. McLerran and H. Weigert, *Phys. Rev. D* **52** (1995) 3809.
131. H. Drescher, M. Hladik, S. Ostapchenko, T. Pierog and K. Werner, *Phys. Rept.* **350** (2001) 93, [arXiv:hep-ph/0007198 \[hep-ph\]](#).
132. K. Werner, I. Karpenko, M. Bleicher, T. Pierog and S. Porteboeuf-Houssais, *Phys. Rev. C* **85** (2012) 064907, [arXiv:1203.5704 \[nucl-th\]](#).
133. J. M. Maldacena, *Int. J. Theor. Phys.* **38** (1999) 1113, [arXiv:hep-th/9711200 \[hep-th\]](#), [Adv. Theor. Math. Phys.2,231(1998)].
134. M. Rho, S.-J. Sin and I. Zahed, *Phys. Lett. B* **466** (1999) 199, [arXiv:hep-th/9907126 \[hep-th\]](#).
135. G. Basar, D. E. Kharzeev, H.-U. Yee and I. Zahed, *Phys. Rev. D* **85** (2012) 105005, [arXiv:1202.0831 \[hep-th\]](#).
136. E. Shuryak and I. Zahed, *Phys. Rev. D* **89** (2014) 094001, [arXiv:1311.0836 \[hep-ph\]](#).
137. T. Kalaydzhyan and E. Shuryak, *Phys. Rev. D* **90** (2014) 025031, [arXiv:1402.7363 \[hep-ph\]](#).
138. U. Heinz and R. Snellings, *Ann. Rev. Nucl. Part. Sci.* **63** (2013) 123, [arXiv:1301.2826 \[nucl-th\]](#).
139. W. Israel, *Annals Phys.* **100** (1976) 310.
140. W. Israel and J. Stewart, *Annals Phys.* **118** (1979) 341.
141. G. Denicol, H. Niemi, E. Molnar and D. Rischke, *Phys. Rev. D* **85** (2012) 114047, [arXiv:1202.4551 \[nucl-th\]](#).
142. H. Niemi and G. Denicol (2014) [arXiv:1404.7327 \[nucl-th\]](#).
143. M. Luzum and P. Romatschke, *Phys. Rev. Lett.* **103** (2009) 262302, [arXiv:0901.4588 \[nucl-th\]](#).
144. I. Bautista, L. Cunqueiro, J. D. de Deus and C. Pajares, *J. Phys. G* **37** (2010) 015103, [arXiv:0905.3058 \[hep-ph\]](#).
145. D. d'Enterria, G. K. Eyyubova, V. L. Korotkikh, I. P. Lokhtin, S. V. Petrushanko, L. I. Sarycheva and A. M. Snigirev, *Eur. Phys. J. C* **66** (2010) 173, [arXiv:0910.3029 \[hep-ph\]](#).
146. S. K. Prasad, V. Roy, S. Chattopadhyay and A. K. Chaudhuri, *Phys. Rev. C* **82** (2010) 024909, [arXiv:0910.4844 \[nucl-th\]](#).
147. P. Bozek, *Acta Phys. Polon. B* **41** (2010) 837, [arXiv:0911.2392 \[nucl-th\]](#).
148. J. Casalderrey-Solana and U. A. Wiedemann, *Phys. Rev. Lett.* **104** (2010) 102301, [arXiv:0911.4400 \[hep-ph\]](#).
149. G. Ortona, G. S. Denicol, P. Mota and T. Kodama (2009) [arXiv:0911.5158 \[hep-ph\]](#).
150. E. Avsar, C. Flensburg, Y. Hatta, J.-Y. Ollitrault and T. Ueda, *Phys. Lett. B* **702** (2011) 394, [arXiv:1009.5643 \[hep-ph\]](#).
151. ALICE Collaboration (K. Aamodt *et al.*), *Phys. Rev. Lett.* **107** (2011) 032301, [arXiv:1105.3865 \[nucl-ex\]](#).
152. P. Bozek and W. Broniowski, *Phys. Lett. B* **720** (2013) 250, [arXiv:1301.3314 \[nucl-th\]](#).
153. Y. Zhou, X. Zhu, P. Li and H. Song, *Phys. Rev. C* **91** (2015) 064908, [arXiv:1503.06986 \[nucl-th\]](#).
154. P. M. Chesler, *Phys. Rev. Lett.* **115** (2015) 241602, [arXiv:1506.02209 \[hep-th\]](#).
155. ALICE Collaboration (B. B. Abelev *et al.*), *Phys. Lett. B* **739** (2014) 139, [arXiv:1404.1194 \[nucl-ex\]](#).
156. P. Bozek and W. Broniowski, *Phys. Lett. B* **747** (2015) 135, [arXiv:1503.00468 \[nucl-th\]](#).

157. P. Romatschke, *Eur. Phys. J. C* **75** (2015) 305, [arXiv:1502.04745 \[nucl-th\]](#).
158. B. Schenke and R. Venugopalan, *Nucl. Phys. A* **931** (2014) 1039, [arXiv:1407.7557 \[nucl-th\]](#).
159. J. Nagle, A. Adare, S. Beckman, T. Koblesky, J. O. Koop, D. McGlinchey, P. Romatschke, J. Carlson, J. Lynn and M. McCumber, *Phys. Rev. Lett.* **113** (2014) 112301, [arXiv:1312.4565 \[nucl-th\]](#).
160. P. Bozek and W. Broniowski, *Phys. Lett. B* **739** (2014) 308, [arXiv:1409.2160 \[nucl-th\]](#).
161. PHENIX Collaboration (A. Adare *et al.*), *Phys. Rev. Lett.* **111** (2013) 212301, [arXiv:1303.1794 \[nucl-ex\]](#).
162. Z.-W. Lin, C. M. Ko, B.-A. Li, B. Zhang and S. Pal, *Phys. Rev. C* **72** (2005) 064901, [arXiv:nucl-th/0411110 \[nucl-th\]](#).
163. X.-N. Wang and M. Gyulassy, *Phys. Rev. D* **44** (1991) 3501.
164. B. Zhang, *Comput. Phys. Commun.* **109** (1998) 193, [arXiv:nucl-th/9709009 \[nucl-th\]](#).
165. G.-L. Ma and A. Bzdak, *Phys. Lett. B* **739** (2014) 209, [arXiv:1404.4129 \[hep-ph\]](#).
166. A. Bzdak and G.-L. Ma, *Phys. Rev. Lett.* **113** (2014) 252301, [arXiv:1406.2804 \[hep-ph\]](#).
167. L. He, T. Edmonds, Z.-W. Lin, F. Liu, D. Molnar and F. Wang, *Phys. Lett.* **B753** (2016) 506, [arXiv:1502.05572 \[nucl-th\]](#).
168. V. N. Gribov and L. N. Lipatov, *Sov. J. Nucl. Phys.* **15** (1972) 438, [*Yad. Fiz.*15,781(1972)].
169. G. Altarelli and G. Parisi, *Nucl. Phys. B* **126** (1977) 298.
170. Y. L. Dokshitzer, *Sov. Phys. JETP* **46** (1977) 641, [*Zh. Eksp. Teor. Fiz.*73,1216(1977)].
171. E. A. Kuraev, L. N. Lipatov and V. S. Fadin, *Sov. Phys. JETP* **45** (1977) 199, [*Zh. Eksp. Teor. Fiz.*72,377(1977)].
172. I. Balitsky and L. Lipatov, *Sov. J. Nucl. Phys.* **29** (1978) 822.
173. L. V. Gribov, E. M. Levin and M. G. Ryskin, *Phys. Rept.* **100** (1983) 1.
174. R. D. Ball, V. Bertone, S. Carrazza, C. S. Deans, L. Del Debbio *et al.*, *Nucl. Phys. B* **867** (2013) 244, [arXiv:1207.1303 \[hep-ph\]](#).
175. Particle Data Group Collaboration (K. Olive *et al.*), *Chin. Phys. C* **38** (2014) 090001.
176. F. Gelis, E. Iancu, J. Jalilian-Marian and R. Venugopalan, *Ann. Rev. Nucl. Part. Sci.* **60** (2010) 463, [arXiv:1002.0333 \[hep-ph\]](#).
177. K. Rummukainen and H. Weigert, *Nucl. Phys. A* **739** (2004) 183, [arXiv:hep-ph/0309306 \[hep-ph\]](#).
178. A. Dumitru, J. Jalilian-Marian, T. Lappi, B. Schenke and R. Venugopalan, *Phys. Lett. B* **706** (2011) 219, [arXiv:1108.4764 \[hep-ph\]](#).
179. T. Lappi, B. Schenke, S. Schlichting and R. Venugopalan (2015) [arXiv:1509.03499 \[hep-ph\]](#).
180. L. D. McLerran and R. Venugopalan, *Phys. Rev. D* **49** (1994) 2233, [arXiv:hep-ph/9309289 \[hep-ph\]](#).
181. L. D. McLerran and R. Venugopalan, *Phys. Rev. D* **49** (1994) 3352, [arXiv:hep-ph/9311205 \[hep-ph\]](#).
182. L. D. McLerran and R. Venugopalan, *Phys. Rev. D* **50** (1994) 2225, [arXiv:hep-ph/9402335 \[hep-ph\]](#).
183. I. Balitsky, *Nucl. Phys. B* **B463** (1996) 99, [arXiv:hep-ph/9509348 \[hep-ph\]](#).
184. Y. V. Kovchegov, *Phys. Rev. D* **61** (2000) 074018, [arXiv:hep-ph/9905214 \[hep-ph\]](#).
185. I. Balitsky, *Phys. Rev. D* **75** (2007) 014001, [arXiv:hep-ph/0609105 \[hep-ph\]](#).
186. Y. V. Kovchegov and H. Weigert, *Nucl. Phys. A* **784** (2007) 188,

- arXiv:hep-ph/0609090 [hep-ph].
187. L. N. Lipatov, *Phys. Rept.* **286** (1997) 131, arXiv:hep-ph/9610276 [hep-ph].
 188. J. L. Albacete and Y. V. Kovchegov, *Phys. Rev. D* **75** (2007) 125021, arXiv:0704.0612 [hep-ph].
 189. T. Lappi and H. Mäntysaari, *Phys. Rev. D* **91** (2015) 074016, arXiv:1502.02400 [hep-ph].
 190. I. Balitsky and G. A. Chirilli, *Phys. Rev. D* **77** (2008) 014019, arXiv:0710.4330 [hep-ph].
 191. E. Iancu, J. D. Madrigal, A. H. Mueller, G. Soyez and D. N. Triantafyllopoulos, *Phys. Lett. B* **744** (2015) 293, arXiv:1502.05642 [hep-ph].
 192. J. L. Albacete, N. Armesto, J. G. Milhano and C. A. Salgado, *Phys. Rev. D* **80** (2009) 034031, arXiv:0902.1112 [hep-ph].
 193. J. L. Albacete, N. Armesto, J. G. Milhano, P. Quiroga-Arias and C. A. Salgado, *Eur. Phys. J. C* **71** (2011) 1705, arXiv:1012.4408 [hep-ph].
 194. H. Fujii, F. Gelis and R. Venugopalan, *Nucl. Phys.* **A780** (2006) 146, arXiv:hep-ph/0603099 [hep-ph].
 195. A. V. Manohar and W. J. Waalewijn, *Phys. Lett. B* **713** (2012) 196, arXiv:1202.5034 [hep-ph].
 196. M. Diehl and A. Schafer, *Phys. Lett. B* **698** (2011) 389, arXiv:1102.3081 [hep-ph].
 197. S. Gavin, L. McLerran and G. Moschelli, *Phys. Rev. C* **79** (2009) 051902, arXiv:0806.4718 [nucl-th].
 198. A. Dumitru, K. Dusling, F. Gelis, J. Jalilian-Marian, T. Lappi *et al.*, *Phys. Lett. B* **697** (2011) 21, arXiv:1009.5295 [hep-ph].
 199. K. Dusling and R. Venugopalan, *Phys. Rev. Lett.* **108** (2012) 262001, arXiv:1201.2658 [hep-ph].
 200. J. Jalilian-Marian and Y. V. Kovchegov, *Phys. Rev. D* **70** (2004) 114017, arXiv:hep-ph/0405266 [hep-ph].
 201. R. Baier, A. Kovner, M. Nardi and U. A. Wiedemann, *Phys. Rev. D* **72** (2005) 094013, arXiv:hep-ph/0506126 [hep-ph].
 202. K. Fukushima and Y. Hidaka, *Nucl. Phys. A* **813** (2008) 171, arXiv:0806.2143 [hep-ph].
 203. E. Iancu and J. Laidet, *Nucl. Phys. A* **916** (2013) 48, arXiv:1305.5926 [hep-ph].
 204. F. Dominguez, C. Marquet, B.-W. Xiao and F. Yuan, *Phys. Rev. D* **83** (2011) 105005, arXiv:1101.0715 [hep-ph].
 205. V. Del Duca (1995) arXiv:hep-ph/9503226 [hep-ph].
 206. D. Colferai, F. Schwennsen, L. Szymanowski and S. Wallon, *JHEP* **12** (2010) 026, arXiv:1002.1365 [hep-ph].
 207. A. Leonidov and D. Ostrovsky, *Phys. Rev. D* **62** (2000) 094009, arXiv:hep-ph/9905496 [hep-ph].
 208. K. Dusling and R. Venugopalan, *Phys. Rev. D* **87** (2013) 051502, arXiv:1210.3890 [hep-ph].
 209. A. H. Mueller and H. Navelet, *Nucl. Phys. B* **282** (1987) 727.
 210. A. Dumitru, in RIKEN-BNL Center Workshop on “Progress in High pT Physics at RHIC”, March 17 – 19, 2010, RBRC Vol. 95, page 129.
 211. Y. V. Kovchegov and K. Tuchin, *Phys. Rev. D* **65** (2002) 074026, arXiv:hep-ph/0111362 [hep-ph].
 212. P. Tribedy and R. Venugopalan, *Nucl. Phys. A* **850** (2011) 136, arXiv:1011.1895 [hep-ph], [Erratum: *Nucl. Phys.*A859,185(2011)].
 213. J. L. Albacete and A. Dumitru (2010) arXiv:1011.5161 [hep-ph].
 214. P. Tribedy and R. Venugopalan, *Phys. Lett. B* **710** (2012) 125, arXiv:1112.2445

- [hep-ph], [Erratum: Phys. Lett.B718,1154(2013)].
215. J. L. Albacete, A. Dumitru, H. Fujii and Y. Nara, *Nucl. Phys. A* **897** (2013) 1, arXiv:1209.2001 [hep-ph].
216. F. Gelis, T. Lappi and R. Venugopalan, *Phys. Rev. D* **78** (2008) 054019, arXiv:0804.2630 [hep-ph].
217. F. Gelis, T. Lappi and R. Venugopalan, *Phys. Rev. D* **78** (2008) 054020, arXiv:0807.1306 [hep-ph].
218. F. Gelis, T. Lappi and R. Venugopalan, *Phys. Rev. D* **79** (2009) 094017, arXiv:0810.4829 [hep-ph].
219. E. Iancu and D. N. Triantafyllopoulos, *JHEP* **11** (2013) 067, arXiv:1307.1559 [hep-ph].
220. D. Teaney and R. Venugopalan, *Phys. Lett. B* **539** (2002) 53, arXiv:hep-ph/0203208 [hep-ph].
221. K. Dusling and R. Venugopalan, *Phys. Rev. D* **87** (2013) 054014, arXiv:1211.3701 [hep-ph].
222. K. Dusling and R. Venugopalan, *Phys. Rev. D* **87** (2013) 094034, arXiv:1302.7018 [hep-ph].
223. Y. V. Kovchegov and D. E. Wertepny (12 2012) 1212.1195.
224. K. Dusling, P. Tribedy and R. Venugopalan (2015) arXiv:1509.04410 [hep-ph].
225. B. A. Kniehl, G. Kramer and B. Potter, *Nucl. Phys. A* **582** (2000) 514, arXiv:hep-ph/0010289 [hep-ph].
226. D. d’Enterria, K. J. Eskola, I. Helenius and H. Paukkunen (11 2013) 1311.1415.
227. T. Lappi, S. Srednyak and R. Venugopalan, *JHEP* **1001** (2010) 066, arXiv:0911.2068 [hep-ph].
228. K. Dusling and R. Venugopalan, *Nucl. Phys. A* **931** (2014) 283.
229. K. Dusling, D. Fernandez-Fraile and R. Venugopalan, *Nucl. Phys. A* **828** (2009) 161, arXiv:0902.4435 [nucl-th].
230. F. Gelis, T. Lappi and L. McLerran, *Nucl. Phys. A* **828** (2009) 149, arXiv:0905.3234 [hep-ph].
231. L. McLerran and P. Tribedy, *Nucl. Phys. A* **945** (2016) 216, arXiv:1508.03292 [hep-ph].
232. T. Lappi, *Phys. Lett. B* **703** (2011) 325, arXiv:1105.5511 [hep-ph].
233. B. Schenke, S. Schlichting and R. Venugopalan, *Phys. Lett. B* **747** (2015) 76, arXiv:1502.01331 [hep-ph].
234. A. Dumitru and A. V. Giannini, *Nucl. Phys. A* **933** (2014) 212, arXiv:1406.5781 [hep-ph].
235. A. Kovner and M. Lublinsky, *Phys. Rev. D* **83** (2011) 034017, arXiv:1012.3398 [hep-ph].
236. A. Kovner and M. Lublinsky, *Phys. Rev. D* **84** (2011) 094011, arXiv:1109.0347 [hep-ph].
237. A. Dumitru and J. Jalilian-Marian, *Phys. Rev. D* **81** (2010) 094015, arXiv:1001.4820 [hep-ph].
238. A. Dumitru, L. McLerran and V. Skokov, *Phys. Lett. B* **743** (2015) 134, arXiv:1410.4844 [hep-ph].
239. T. Lappi, *Phys. Lett. B* **744** (2015) 315, arXiv:1501.05505 [hep-ph].
240. E. Levin and A. H. Rezaeian, *Phys. Rev. D* **84** (2011) 034031, arXiv:1105.3275 [hep-ph].
241. E. Levin and S. Tapia (2014) arXiv:1406.7358 [hep-ph].
242. M. Gyulassy, P. Levai, I. Vitev and T. S. Biro, *Phys. Rev. D* **90** (2014) 054025, arXiv:1405.7825 [hep-ph].

243. ATLAS Collaboration (G. Aad *et al.*), *Phys. Rev. C* **90** (2014) 024905, [arXiv:1403.0489 \[hep-ex\]](#).
244. ATLAS Collaboration (G. Aad *et al.*) (2015) [arXiv:1504.01289 \[hep-ex\]](#).
245. L. Yan, *Phys. Rev. C* **91** (2015) 064909, [arXiv:1503.00880 \[nucl-th\]](#).
246. P. Bozek and W. Broniowski (2015) [arXiv:1506.02817 \[nucl-th\]](#).
247. The ATLAS collaboration, *ATLAS-CONF-2015-027* (2015).
248. A. Accardi *et al.* (2012) [arXiv:1212.1701 \[nucl-ex\]](#).
249. B. G. Zakharov, *Phys. Rev. Lett.* **112** (2014) 032301, [arXiv:1307.3674 \[hep-ph\]](#).
250. CMS Collaboration (S. Chatrchyan *et al.*), *Phys. Rev. Lett.* **109** (2012) 022301, [arXiv:1204.1850 \[nucl-ex\]](#).
251. CMS Collaboration (S. Chatrchyan *et al.*), *Eur. Phys. J. C* **74** (2014) 2951, [arXiv:1401.4433 \[nucl-ex\]](#).
252. ALICE Collaboration (B. Abelev *et al.*), *Phys. Rev. Lett.* **110** (2013) 082302, [arXiv:1210.4520 \[nucl-ex\]](#).
253. ALICE Collaboration (J. Adam *et al.*), *Phys. Rev. C* **91** (2015) 064905, [arXiv:1412.6828 \[nucl-ex\]](#).
254. M. Alvioli, B. A. Cole, L. Frankfurt, D. V. Perepelitsa and M. Strikman (2014) [arXiv:1409.7381 \[hep-ph\]](#).
255. N. Armesto, D. C. Glhan and J. G. Milhano, *Phys. Lett. B* **747** (2015) 441, [arXiv:1502.02986 \[hep-ph\]](#).
256. M. Strickland, *Pramana* **84** (2015) 671, [arXiv:1312.2285 \[hep-ph\]](#).
257. S. Pratt, *Phys. Rev. Lett.* **102** (2009) 232301, [arXiv:0811.3363 \[nucl-th\]](#).
258. W. van der Schee, P. Romatschke and S. Pratt, *Phys. Rev. Lett.* **111** (2013) 222302, [arXiv:1307.2539](#).